UCLouvain

École polytechnique de Louvain

Implementation of the no-slip boundary condition and of a wall shear stress model in the vorticity-velocity exascale-ready Murphy framework

Author: **Julien KLAUNER**
Supervisors: **Philippe CHATELAIN, Grégoire WINCKELMANS**
Reader: **Laurent BRICTEUX**
Academic year 2022–2023
Master [120] in Electrical Engineering

Contents

Acknowledgements

First of all, I would like to thank my two promoters, Prof. Chatelain and Prof. Winckelmans, for proposing this fascinating and comprehensive subject to me. But also, with the help of Prof. Duponcheel, for having greatly advised me and helped me to develop the implemented models.

I would also like to thank Prof. van Rees for welcoming me into his laboratory during my student research internship at MIT to start my master's thesis. I would also like to thank Thomas Gillis for mentoring me to get started in Murphy.

I would like to thank Pierre Balty and Gilles Poncelet for being available to answer all of my questions and assist me in correcting issues I may have encountered in the code.

All simulations done for this thesis could not have been possible without the computational resources provided by the supercomputing facilities of the Université Catholique de Louvain (UCL) and the Consortium des Equipements de Calcul Intensif en Fédération Wallonie Bruxelles (CECI) funded by the Fond de la Recherche Scientifique de Belgique (F.R.S.-FNRS). The simulations were mainly performed on NIC5 from the Université de Liège (ULg).

I would also like to thank my parents for all their support, as well as my brother Tom, for having accompanied me during these five years of study. I also want to thank Clémence for her careful proofreading, and I hope that it has given her a new interest in fluid mechanics.

Finally, I would like to express my gratitude towards Mrs Manfroid, my high school maths teacher. She gave me the passion for mathematics but also the rigor necessary to complete my engineering degree.

Chapter 1

Introduction

Direct Numerical Simulation (DNS) can simulate a flow with a high accuracy until small scales. However, for turbulent flow, due to the wide range of scales involved in the process, this approach already requires significant computational resources for low Reynolds numbers. For high Reynolds, it becomes not affordable, even on supercomputers. This requirement is also even higher when the flow interacts with a wall. Indeed, this type of turbulent flow in contact with solid boundaries can be seen in real-world examples, such as the wind in the atmospheric boundary layer or the flow around a wing, which are particularly challenging to simulate numerically.

In order to overcome this issue, the idea is to model for both the effect of the small unresolved scales in the bulk flow and the effect of those emerging from the wall. Hence, the objective is to implement a wall-modeled LES, which uses LES for the outer layer and a wall model for the inner layer, in order to relax the constraint on grid size, and reduce the required computational resources. While wall models for codes based on the velocity-pressure formulation of the Navier-Stokes equations have already been studied previously, the present work has the particularity to use the velocity-vorticity formulation for which no model has yet been developed.

Hence, a wall shear stress model is developed and implemented in the TFL-UCL and Van Rees Lab in-house vorticity-velocity code based on the exascale-ready framework Murphy. The present work is structured into seven chapters apart from the conclusion and introduction :

- The second chapter introduces Murphy and develops the vorticty-velocity formulation of Navier-Stokes equations that are used in the code. The Poisson solver is also shortly covered.
- Chapter three proposes a validation of the solver for DNS of turbulent flows through the Taylor-Green vortex test cases. Results of global quantities, energy spectra, and vorticity slices are compared to those obtained from a pseudo-spectral code developed at UCL.
- Equations for two SGS models are set in the fourth chapter, and both models are implemented in Murphy, as required for further chapters. The Taylor-Green

vortex test case is re-used in order to study the influence of these models on isotropic turbulence.

- The fifth chapter sets up the no-through flow boundary condition, which is also used to impose the no-slip condition in the following chapter correctly. Thus, the no-through flow boundary condition acts as a plane of symmetry, and by allowing diffusion through the wall, the reconnection of two vortex rings can be studied as a validation.

- The development to impose a no-slip boundary condition in a velocity-vorticity code is explained in chapter six. A first validation is done with a 1D Poiseuille flow.

- Chapter seven yields further validation of the no-slip boundary condition with a DNS of turbulent channel flow at a low Reynolds number of $Re_\tau = 180$.

- The eighth chapter presents the model that we propose for wall-modeled LES, designed for a velocity-vorticity code. This model is investigated through an under-resolved channel flow at $Re_\tau = 2000$.

Chapter 2

Foreword

2.1 Murphy

MURPHY (MUltiResolution multiPHYsics) in an in-house flow solver developed at UCL-TFL and at Van Rees Lab (MIT). This solver is "a multiresolution adaptive grid framework for numerical simulations on 3D block structured collocated grids with distributed computational architectures" [18]. The code exploits a block-structured grid data structure. Thus, the domain is cut into cubic blocks of equal size and equal number of degree of freedom. Thanks to this structured grid, the code is able to parallelize the computation by means of a one-sided MPI-RMA communication approach with active PSCW synchronization[18].

The code is based on standard finite-difference operators, and in the present work, we will keep to operators of the fourth order. The time discretization is done by means of a total variation diminishing Runge-Kutta of order 3 (RK3). Furthermore, we will only use a uniform grid, without any adaptation. The Navier-Stokes equations are expressed in their Eulerian vorticity-velocity formulations instead of the classic velocity-pressure formulation, and equations used by the solver are described in the following section. The advantage of this formulation is that it could be further developed in order to express the Navier-Stokes equations in their Lagrangian form and to implement the vortex methods. The latter are preferred for external flow with compact vorticity because they benefit from low numerical dissipation, and it could also allow larger time steps during the simulation[40].

2.2 Vorticity-velocity formulation of the Navier-Stokes equations

The classical way to express the Navier-Stokes equations is the velocity-pressure formulation and the corresponding conservation equations are then expressed as,

$$\nabla \cdot \mathbf{u} = 0, \tag{2.1}$$

$$\frac{D\mathbf{u}}{Dt} = \frac{\partial \mathbf{u}}{\partial t} + \mathbf{u} \cdot \nabla \mathbf{u} = -\nabla P + \nu \nabla^2 \mathbf{u}. \tag{2.2}$$

The first equation is the conservation of mass in the case of an incompressible flow and the second one is the conservation of momentum. However, Murphy uses the velocity-vorticity expression of Navier-Stokes equations. The vorticity is defined as the curl of the velocity field,

$$\boldsymbol{\omega} = \nabla \times \mathbf{u}. \tag{2.3}$$

By using this defined quantity, we can rewrite the conservation of momentum as,

$$\frac{D\boldsymbol{\omega}}{Dt} = \frac{\partial \boldsymbol{\omega}}{\partial t} + \mathbf{u} \cdot \nabla \boldsymbol{\omega} = (\boldsymbol{\omega} \cdot \nabla)\mathbf{u} + \nu \nabla^2 \boldsymbol{\omega}. \tag{2.4}$$

This equation is again rewritten by using the relation $(\boldsymbol{\omega} \cdot \nabla)\mathbf{u} - (\mathbf{u} \cdot \nabla)\boldsymbol{\omega} = -\nabla \times (\mathbf{u} \times \boldsymbol{\omega})$, and then $(\mathbf{u} \times \boldsymbol{\omega}) = (\mathbf{u} \times (\nabla \times \mathbf{u}))) = -((\nabla \times \mathbf{u}) \times \mathbf{u})$. Hence, the equation implemented numerically in Murphy is retrieved and reads,

$$\frac{\partial \boldsymbol{\omega}}{\partial t} = \nu \nabla^2 \boldsymbol{\omega} + \nabla \times ((\nabla \times \mathbf{u}) \times \mathbf{u}). \tag{2.5}$$

This formulation is focused on the vorticity field and by knowing this field at a certain time, the field at a next time step can be computed using the RK3 scheme. Thus, initial conditions for the test cases in next chapters are expressed in terms of vorticity. Nevertheless, the velocity field is still required to express the Navier-Stokes equations. Hence, the velocity can directly be computed from vorticity field by means of a Poisson equation. The first approach is by using equations 2.1 and 2.3 to find the following relation,

$$\nabla^2 \mathbf{u} = -\nabla \times \boldsymbol{\omega}. \tag{2.6}$$

However, another approach is used in the code with the stream function $\boldsymbol{\Psi}$. At first, the stream function is computed as,

$$-\nabla^2 \boldsymbol{\Psi} = \boldsymbol{\omega}. \tag{2.7}$$

We can note that the stream function is just a step to compute the velocity field and it is not used in the numerical resolution. However, it is still useful for diagnostic purposes, as computing the global kinetic energy in a certain way. Then, from the stream function, the velocity field is retrieved as,

$$\mathbf{u} = \nabla \times \boldsymbol{\Psi}. \tag{2.8}$$

These formulations of Navier-Stokes equations benefit from preservation properties, such as conserving helicity, energy, and impulse without the generation of spurious divergence, as developed by Gabbard [15].

2.3 Poisson solver

The Poisson equation 2.7 is solved in the spectral domain by means of FLUPS (Fourier-based Library of Unbounded Poisson Solvers). The latter is defined from [5] as: "FLUPS leverages a dedicated implementation of 3D Fourier transforms to solve the Poisson equation using Green's functions, in a fast and memory-efficient way".

Thus, for a given Poisson equation in a 3D computational domain,

$$\nabla^2 \phi = f, \tag{2.9}$$

the solution is given as,

$$\phi = G * f, \tag{2.10}$$

where G is the Green's function. However, the algorithm consists in solving this equation in the spectral domain as,

$$\hat{\phi} = \hat{G}\hat{f}, \tag{2.11}$$

where $\hat{\cdot}$ corresponds to the 3D Fourier transform operation. The transition from one equation to another is made by means of fast Fourier transforms (FFT). From a numerical point of view, 3D FFTs are obtained by successive 1D FFTs in the three directions, wich leads to a complexity of $\mathcal{O}(N \log(N))$. However, the main problem is that discrete Fourier transforms (DFT) enforce periodic boundary conditions. Nevertheless, the different combinations of odd and even symmetries are still achievable by means of cosine and sine transforms (DCT and DST). The case of fully unbounded directions is not as simple and requires to double the domain using zero-padding. Several expressions of Green's kernel are possible, also depending on the combination of periodic, symmetric, semi-unbounded and fully unbounded boundary conditions. Hence, by default, the Singular family of Green's functions are used and their expressions are given in [5].

Chapter 3

Direct Numerical Simulation (DNS)

3.1 Introduction

Direct Numerical Simulation (DNS) aims to capture the entire spectrum of wavenumbers that composes the flow to be then able to simulate all interactions between the different scales.

A fully turbulent regime is constituted by a large range of turbulent scales. Kolmogorov's dimensional analysis of homogeneous isotropic turbulence (HIT) [38], as covered by Carton de Wiart [6], reveals that the energy belonging to larger eddies is gradually cascaded down to more minor scales by means of inertial effects. The inertial subrange corresponds to the range of wavenumbers where this phenomenon occurs without energy loss. However, viscous dissipation progressively becomes more critical when scales decrease until it becomes predominant and the energy is converted into heat from dissipation in the so-called dissipation range. In the inertial range, Kolmogorov states that the associate energy spectrum follows,

$$E(k) = C_K \epsilon^{2/3} k^{-5/3}, \tag{3.1}$$

where k corresponds to the wavenumber, ϵ is the dissipation rate, and C_K is the Kolmogorov constant. Figure 3.1 shows the energy cascade from a typical HIT's energy spectrum and identifies the three ranges.

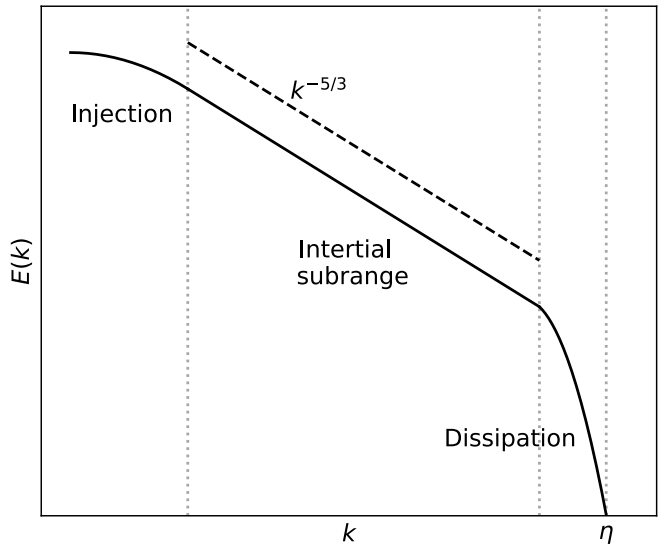

Figure 3.1: Typical energy spectrum of HIT at high Reynolds number.

Thus, we are interested in characterizing the order of magnitude of the smallest turbulent scale, η, called Kolmogorov scale. As developed by Thiry [48], if a vortex, characterized by a vorticity ω_η and a scale η, is at the Kolmogorov scale, viscous and convective terms are at the same magnitude. Thus, the corresponding Reynolds number based on vorticity must be of order 1 at that specific scale.

$$Re_\eta = \frac{\eta^2 \omega_\eta}{\nu} = \frac{\eta u_\eta}{\nu} = 1, \tag{3.2}$$

where the corresponding velocity scale is defined as $u_\eta = \omega_\eta \eta$. As mentioned before, at this scale, the energy is converted into heat from dissipation, and the energy dissipation rate, defined as $\epsilon = 2\nu S_{ij} S_{ij}$, scales as,

$$\epsilon = \nu \frac{u_\eta^2}{\eta^2}. \tag{3.3}$$

Hence, according to the previous relationship, the characteristic velocity and vorticity of these small-scale eddies are given by,

$$u_\eta = (\epsilon \nu)^{1/4}, \tag{3.4}$$

$$\omega_\eta = \left(\frac{\epsilon}{\nu}\right)^{1/2}. \tag{3.5}$$

Based on equation 3.2 and equation 3.4, the Kolmogorov scale can be found as a function of ν and ϵ,

$$\eta = \left(\frac{\nu^3}{\epsilon}\right)^{1/4}. \tag{3.6}$$

In addition, the large scales of the flow can entirely determine the dissipation rate. Indeed, all the energy initially comes from the large scales in the injection ranges, and the link between dissipation rate and structure of large characteristic size L and velocity U can be expressed as,

$$\epsilon \propto \frac{U^3}{L}. \tag{3.7}$$

The Reynolds number is also defined from these quantities as $Re = UL/\nu$. Hence, based on equations 3.6 and 3.7, we find that the ratio of scales is proportional to the Reynolds number to $\eta/L \propto Re^{3/4}$. Based on the latter ratio, the required number of grid's points, N, in each direction is proportional to $N \propto L/\eta \propto Re^{3/4}$. Therefore, the total cost of the simulation, which corresponds to the product between grid size in the three-dimensional space and the number of time steps, is proportional to,

$$N_x N_y N_z N_t \propto \left(\frac{L}{\eta}\right)^4 \propto Re^3. \tag{3.8}$$

Meeting these requirements for direct numerical simulation becomes challenging for high Reynolds number flows.

Therefore, the Kolmogorov scale must be resolved to be qualified of DNS. Thus, a condition on the grid size can be identified such that the simulation is able to capture scales until the Kolmogorov scale, which reads,

$$h \leq 2\eta. \tag{3.9}$$

[51]

3.2 Taylor-Green Vortex test case

The first test case investigated here is the Taylor-Green Vortex. The latter gives the ability to study the dynamics of transition into turbulence, with the formation of small-scale vortical structures and small-scale eddies under the influence of stretching, as stated and studied by Rees et al. [40].

3.2.1 Initial condition and numerical setup

This flow is characterized by triple periodic boundary conditions in a box of equal lengths $L \times L \times L$. The origin of the box is located in one of the corners. The initial

flow condition sets the velocity field $\mathbf{u} = (u, v, w)$ as given below,

$$\begin{aligned} u &= U_0 \sin\left(\frac{x-0.5}{L/2\pi}\right)\cos\left(\frac{y-0.5}{L/2\pi}\right)\cos\left(\frac{z-0.5}{L/2\pi}\right), \\ v &= -U_0 \cos\left(\frac{x-0.5}{L/2\pi}\right)\sin\left(\frac{y-0.5}{L/2\pi}\right)\cos\left(\frac{z-0.5}{L/2\pi}\right), \\ w &= 0. \end{aligned} \tag{3.10}$$

However, because the velocity-vorticity formulation is used, the initial condition is expressed as a vorticity field $\boldsymbol{\omega} = (\omega_x, \omega_y, \omega_z) = \nabla \times \mathbf{u}$ which is given by,

$$\begin{aligned} \omega_x &= -\frac{U_0}{L/2\pi}\cos\left(\frac{x-0.5}{L/2\pi}\right)\sin\left(\frac{y-0.5}{L/2\pi}\right)\sin\left(\frac{z-0.5}{L/2\pi}\right), \\ \omega_y &= -\frac{U_0}{L/2\pi}\sin\left(\frac{x-0.5}{L/2\pi}\right)\cos\left(\frac{y-0.5}{L/2\pi}\right)\sin\left(\frac{z-0.5}{L/2\pi}\right), \\ \omega_z &= \frac{U_0}{L/2\pi}\sin\left(\frac{x-0.5}{L}\right)\sin\left(\frac{y-0.5}{L/2\pi}\right)\cos\left(\frac{z-0.5}{L/2\pi}\right) \\ &\quad + \frac{U_0}{L/2\pi}\sin\left(\frac{x-0.5}{L/2\pi}\right)\sin\left(\frac{y-0.5}{L/2\pi}\right)\cos\left(\frac{z-0.5}{L/2\pi}\right). \end{aligned} \tag{3.11}$$

The flow is characterized by a moderate Reynolds number of $Re = U_0/\nu k_L = 1600$ where the wavenumber is defined as $k_L = 2\pi/\lambda$ and where wavelength λ corresponds to the length L of the cube. This Reynolds number is large enough to achieve a transition to small-scale turbulence in a short time. The metrics of interest are the kinetic energy E^k and the enstrophy $\mathcal{E}$ with respect to the time. The kinetic energy integrated on the domain Ω is given by,

$$E^k = \frac{1}{\rho_0 \Omega}\int_\Omega \rho \frac{\boldsymbol{\omega}\cdot\boldsymbol{\Psi}}{2} d\Omega, \tag{3.12}$$

and the enstrophy integrated on the domain Ω is given by,

$$\mathcal{E} = \frac{1}{\rho_0 \Omega}\int_\Omega \rho \frac{\boldsymbol{\omega}\cdot\boldsymbol{\omega}}{2} d\Omega. \tag{3.13}$$

Dimensionless quantities are considered here, and they are defined as follows. Firstly, the characteristic time is identified as $t_c = 1/k_L U_0$ to obtain $\tau = t/t_c$, $\mathcal{E}^* = \mathcal{E}\cdot t_c^2$ and $E^{k^*} = E^k/U_0^2$. Since the kinetic energy may not be enough discriminant, the last metric used here is the kinetic energy dissipation, defined as $\epsilon = -dE^k/dt$ and in dimensionless quantities as $\epsilon^* = -dE^{k^*}/d\tau$. The latter is computed with a finite difference from the global kinetic energy with respect to time, and for incompressible flow, the equality $\epsilon = 2\nu\mathcal{E}$ must be respected. The simulation duration is $\tau_{final} = 20$. Two other particular times are observed, the first at $\tau \simeq 4$, corresponding to the transition period when the dissipation starts to soar. The second is when the maximum dissipation happens at $\tau \simeq 8$, which is also the

moment when the smallest turbulent structures are formed. These specific times are seen in Figure 3.2, which shows the iso-surfaces of the z-component of vorticity from an under-resolved simulation on a 128^3 grid for illustration purposes. The light grey lines correspond to the delimitation of the sub-blocks of the domain.

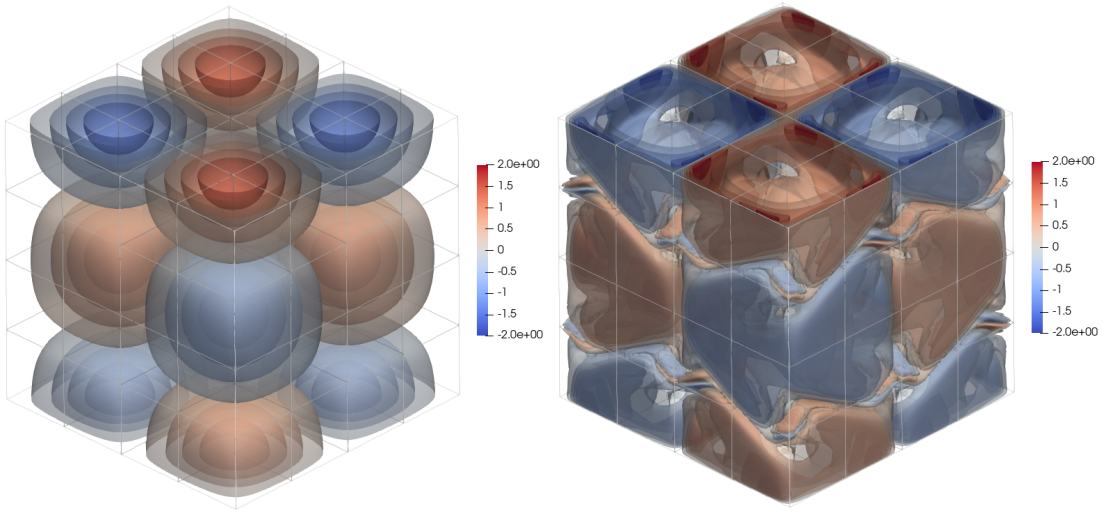

(a) $\tau = 0$ (b) $\tau = 4$

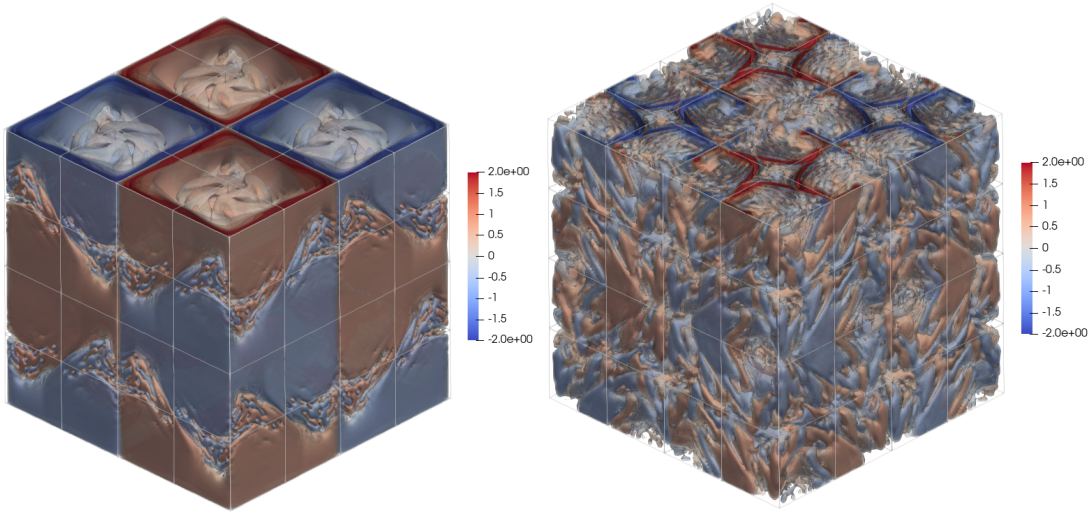

(c) $\tau = 8$ (d) $\tau = 20$

Figure 3.2: Taylor-Green vortex iso-surfaces of the z-component of the dimensionless vorticity with respect to time, with a 128^3 mesh.

Figure 3.3 illustrates, in the same way as DeBonis [11], the evolution of the flow from the inviscid flow into the turbulent decay process. This evolution is outlined by DeBonis [11] from Brachet et al. [4]. In the beginning stages, the flow is described as inviscid, while the vortices gradually develop and roll up. At $\tau = 7$, a change in the smooth structure of vortice appears and keeps evolving until these coherent structures break down at approximately $\tau = 9$. Thus, the flow becomes fully turbulent after

the breakdown and the structures progressively deteriorate until the flow becomes stable.

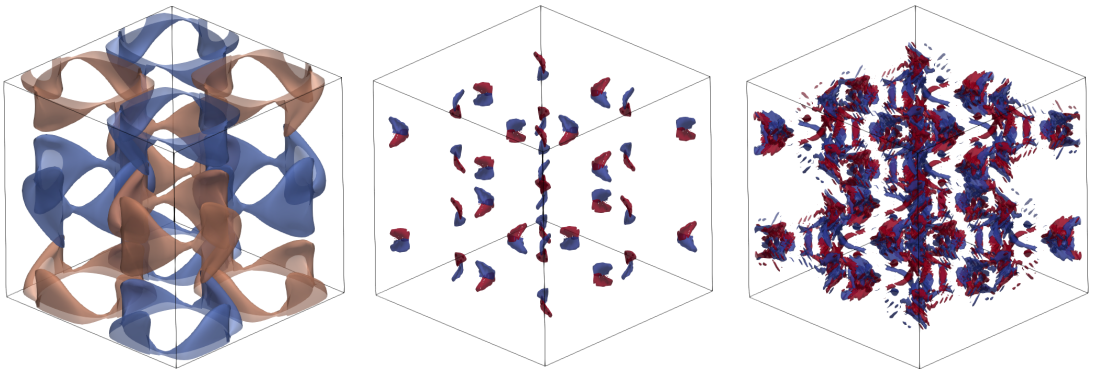

(a) $\tau = 3$, inviscid. (b) $\tau = 5$, vortex roll-up. (c) $\tau = 7$, structure changes.

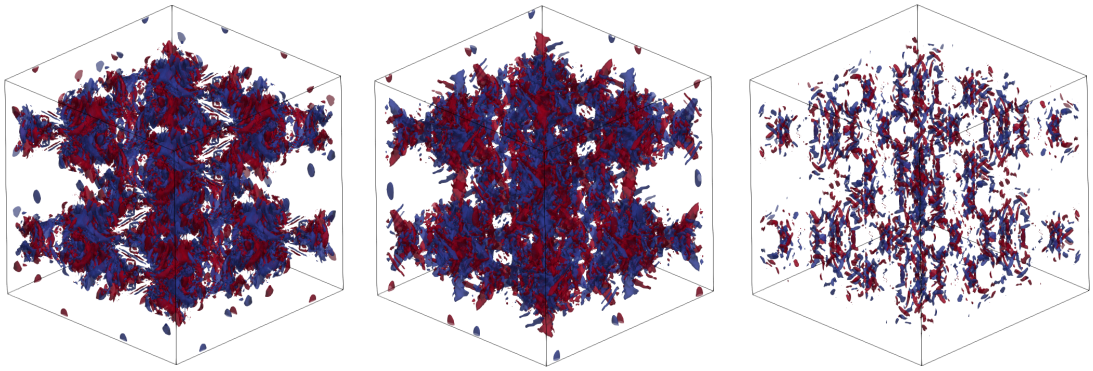

(d) $\tau = 9$, breakdown. (e) $\tau = 11$, fully turbulent. (f) $\tau > 11$, turbulent decay.

Figure 3.3: Evolution of iso-surfaces of the z-component of the dimensionless vorticity, with a 128^3 mesh.

The metrics presented above are compared with a reference solution achieved with a dealiased pseudo-spectral code developed at Université catholique de Louvain (UCL), which has been done with 512^3 degrees of freedom (dof). Thus, several simulations with different grid sizes, 128^3, 256^3, and 512^3 dof are compared with the reference. Lower resolution results, such as 256^3, indicate how the code can still closely approximate the reference with an under-resolved simulation.

For the well-resolved solution of 512^3, the domain is divided into 4096 sub-blocks with each 32^3 dof. This division into several sub-blocks allows parallel computation, and this simulation runs on 256 CPUs during 6.62 hours of physical time to achieve the $\tau_{final} = 20$. The simulation parameters are tabulated in Tab 3.1. Moreover, the Table 3.2 gives the computational resources required depending on the resolution.

$Re = U_0/\nu k_L$	N_x	N_y	N_z	L_x [m]	L_y [m]	L_z [m]	t_c [s]
1600	512	512	512	1.0	1.0	1.0	$1/2\pi$

Table 3.1: Numerical parameters for the simulation of the Taylor-Green vortex test case.

# dof	# Blocks	# CPU	Physical Time [Hour]
128^3	64	64	0.45
256^3	512	256	1.27
512^3	4096	256	6.62

Table 3.2: Physical times comparison with respect to dof.

The mesh Reynolds number based on vorticity is computed as,

$$Re_\omega = \frac{(|\boldsymbol{\omega}|)h^2}{\nu}. \tag{3.14}$$

Hence, based on the maximum vorticity at each time step, the evolution of the Reynolds number with respect to the time for the 512^3 mesh is given at Figure 3.4. This number must not be excessive to guarantee the accuracy of the simulations.

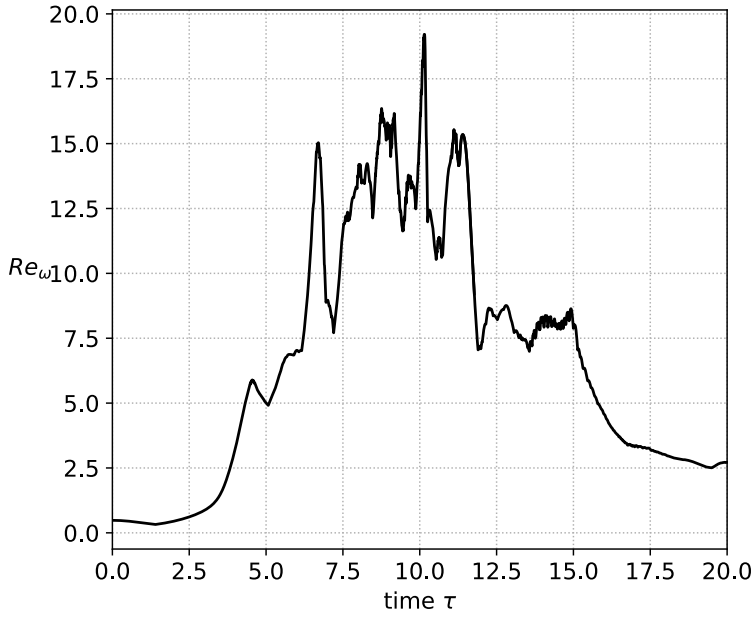

Figure 3.4: Mesh Reynolds number based on vorticity for Taylor-Green test case.

3.2.2 Results and discussion

Global diagnostic

The Figure 3.5 shows the evolution of the global enstrophy for the three resolutions. At first, they all overlap with the reference until achieving the transition time at $\tau \simeq 4$. At this time, the case of 128^3 has an earlier dissipation of kinetic energy, which leads to a shift in the enstrophy peak to the left. For resolutions of 256^3 and 512^3, the peak is reached at the same time as for the reference. The case of 256^3 starts to slightly deviate at $\tau \simeq 7$ and will over-predict the peak of enstrophy. Finally, the resolution of 512^3 overlaps well with the reference, but it very slightly over-predicts the enstrophy peak (as seen in the close-up plot). Therefore, we observe that the simulations performed with Murphy converge towards the reference from above.

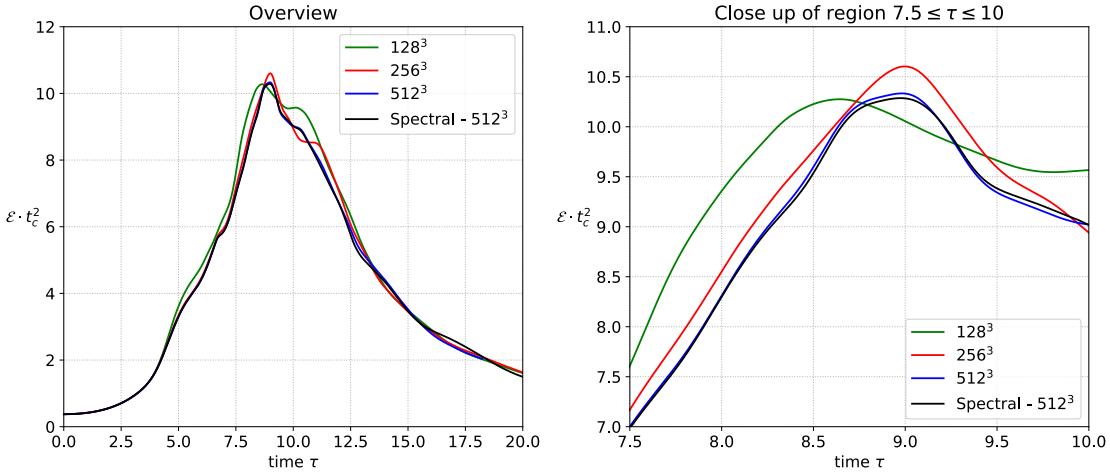

Figure 3.5: Temporal evolution of the global enstrophy for Taylor-Green vortex and for different resolutions.

Figure 3.6 (left) presents the evolution of the global kinetic energy, for different resolutions. As mentioned above, this metric is not well discriminating since the global kinetic energy is well preserved no matter the resolution. Indeed, all the curves overlap with occasional minor deviations from the reference at specific periods. Hence, kinetic energy dissipation will be favored, as shown in Figure 3.6 (right). From this figure, the same behaviors with the enstrophy are observed since a direct relationship exists and links these two metrics as $\epsilon = 2\nu\mathcal{E}$. However, during the peak of kinetic energy dissipation for the resolution of 128^3, a drop with respect to the reference can be noticed, which was not observed with the diagnostic of enstrophy. Indeed, the relationship does not seem to be completely respected here, and it is most noticeable for the lowest resolution, but a difference remains for the finest grids. This observation will be discussed later in this paper.

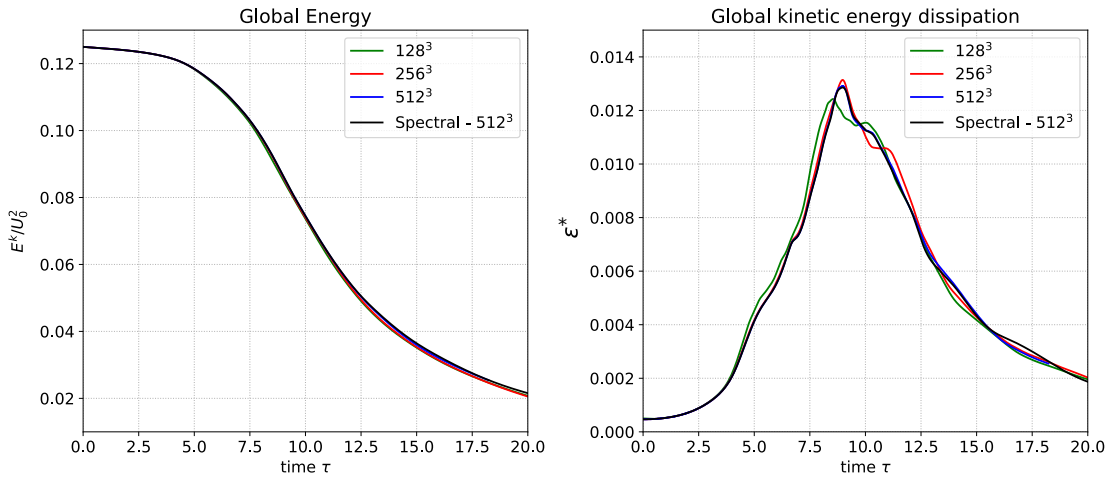

Figure 3.6: Temporal evolution of the kinetic energy (left) and kinetic energy dissipation (right) for Taylor-Green vortex and for different resolutions.

Once the kinetic energy dissipation is computed, its maximum value can be used in order to verify that the simulation captures up to the Kolmogorov scale. From the relationship 3.6, we find that the constraint is respected for the mesh of 512^3 since $h/\eta = 1.05 < 2$. However, this is no longer the case for a grid twice as coarse, such as 256^3.

Spectral analysis

Figure 3.7 shows the energy spectrum for the finest resolution, i.e., 512^3, and this for different times. Note that the energy spectrum is computed from the velocity field at a certain time thanks to a code given by Saad and Sutherland [43]. As mentioned above, the Taylor-Green test case allows for a study of the generation of small-scale eddies. Indeed, as observed in the figure, the energy of high wavenumbers grows with respect to time until it achieves a maximum at $\tau \simeq 8$. This time corresponds to the start of the dissipation peak $\tau = 8 \rightarrow 10$, and when the most complex flow structures appear. After reaching this maximum, the energy spectrum decays for all wave numbers. Note that after $\tau = 4$, the energy decreases monotonically with a slope of $k^{-5/3}$ in the inertial subrange, as described by analysis of Kolmogorov from HIT.

The Figure 3.8 shows the spectra at $\tau = 9$ for the three resolutions. One can observe that the energy is falling below the reference when approaching the end of wavenumbers available associated with the resolution. However, before this phenomenon, the energy spectrum is close to the reference at all resolutions. As expected, the finest resolution of 512^3 is the one that overlaps the most with the reference.

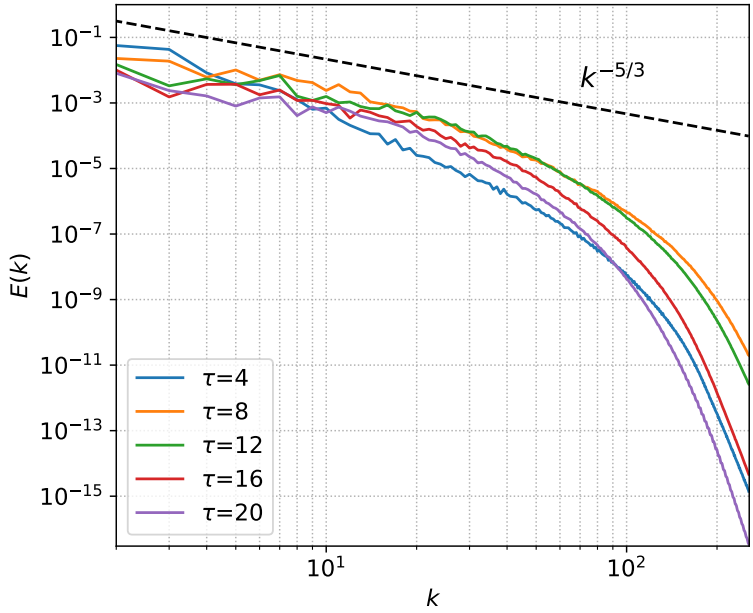

Figure 3.7: Complete energy spectrum of the Taylor–Green vortex for different times at a resolution of 512^3.

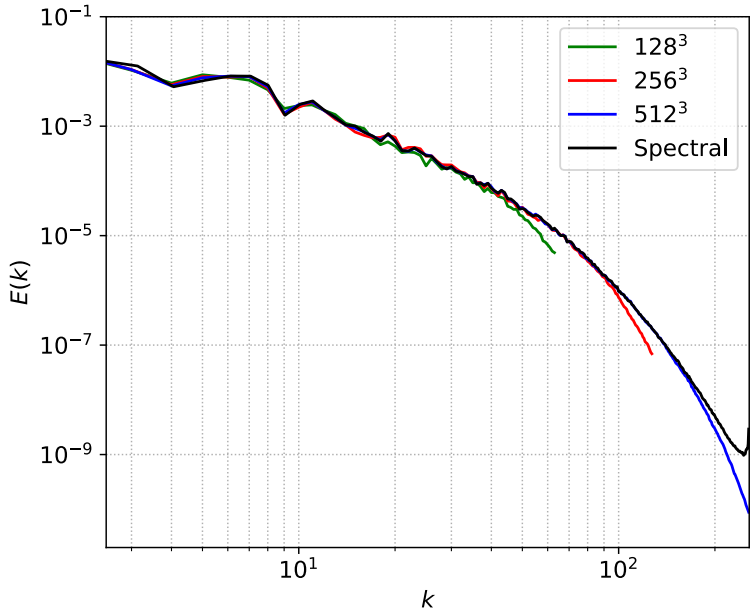

Figure 3.8: Comparison of the complete energy spectrum of the Taylor–Green vortex for different resolutions and for $\tau = 9$.

Vortical structures

As done by Carton de Wiart [6] and Rees et al. [40], slices of the instantaneous vorticity field can be visualized in order to get intuition into the origins of errors. Since the most complex structures happen during the dissipation peak, the most relevant times are between $\tau = 8 \rightarrow 10$. Furthermore, thanks to periodic structures, only one quarter of the slice will be considered for the sake of clarity.

Firstly, a slice for the grid size of 512^3 is plotted in figure 3.9, and it is compared with the pseudo-spectral code. Iso lines are very similar in both cases. Although the fields are remarkably similar, the simulation from Murphy slightly overestimates the vortex structures at very specific locations, in the figure, they are visible as the magenta contours surrounding the two black dots. Rees et al. [40] observe similar behavior with their code, which use the vortex method.

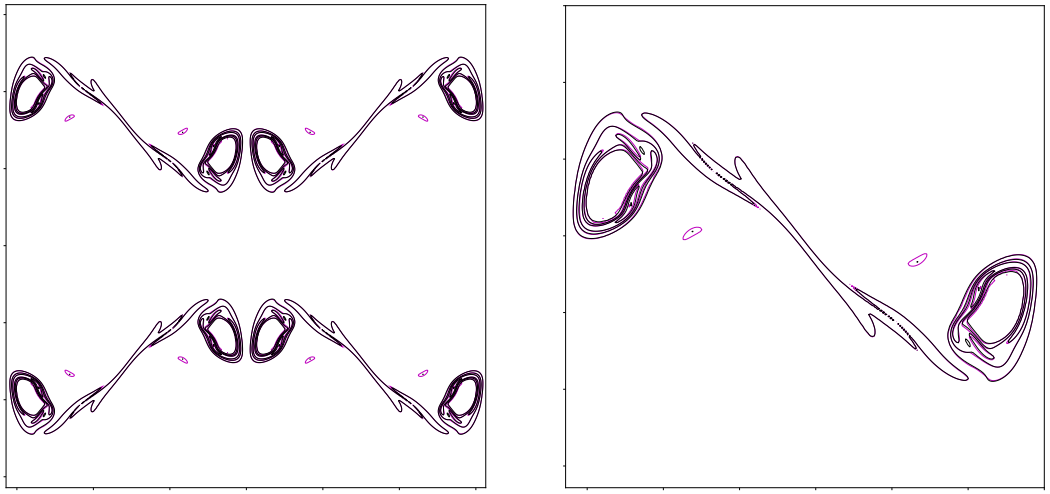

Figure 3.9: Dimensionless vorticity norm at $\tau = 8$, iso-contours of $\omega^* = |\boldsymbol{\omega}|L/U_0 =$ 1,5,10,20,30, the plane is a slice of the domain at $y/L = 0$. Full domain (left) and closed region (right). Murphy (—), spectral solution (—), grid size = 512^3.

Then, Figure 3.10 compares the reference with under-resolved simulations of 128^3 and 256^3 dof. Firstly, the location of the vortex structures is globally captured by the coarse resolutions. For the 256^3 resolution, the structures are close to the reference but contaminated with some non-regularity. Indeed, the highest resolution is smoother. For the lowest resolution of 128^3, it is possible to distinguish global shapes, but the characteristic shape at the edge is no longer perceptible.

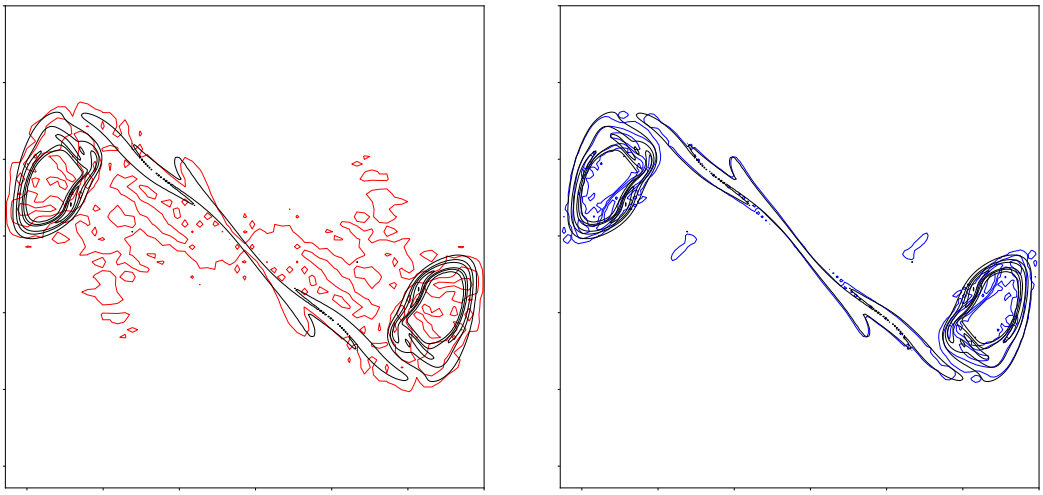

Figure 3.10: Dimensionless vorticity norm at $\tau = 8$, iso-contours of $\omega^* = |\boldsymbol{\omega}|L/U_0 =$ 1,5,10,20,30, the plane is a slice of the domain at $y/L = 0$. Case of under-resolved simulation done in Murphy : 128^3 (left, —), 256^3 (right, —) and spectral solution (—).

Spectral mode analysis

The velocity field is recovered from the vorticity field by solving the Poisson equation with FLUPS. As explained in Section 2.3, the solution of $\nabla^2\phi = f$ is obtained as $\phi = G * f$. However, the expression of Green's function G influences the solution. The Taylor-Green vortex test case has periodic boundaries in the three directions, and therefore, the expressions of Green's function are the ones for three spectral directions, as found in [5]. Two kernels are investigated here, the well-known exact solution, named Singular (SG), reads,

$$\hat{G}(\boldsymbol{k}) = -\frac{1}{k^2} \quad \text{, where} \quad k = \sqrt{k_x^2 + k_y^2 + k_z^2}. \tag{3.15}$$

The second kernel is the Lattice Green's Function of order 4 (LGF4). The latter is computed as the spectral equivalent of the finite difference of Poisson equation, $\nabla_h^2\phi = f$, and reads,

$$\begin{aligned} \hat{G}(\boldsymbol{k}) &= -\frac{h^2}{(f(k_x) + f(k_y) + f(k_z))}, \\ \text{where} \quad f(k_i) &= \frac{1}{3}\left(16\sin^2(k_i h/2) - \sin^2(2k_i h/2)\right). \end{aligned} \tag{3.16}$$

[50]

Unless otherwise stated, the default Green's function is SG, and therefore, it was the one used in the previous simulations.

The comparison of global enstrophy between both Green's functions is presented in figure 3.11. Regardless of resolution, LGF4 induces an underestimation of enstrophy compared to SG. Hence, it increases the discrepancy between the references for 128^3, but for 256^3, this underestimation is beneficial and brings it closer to the reference in the peak.

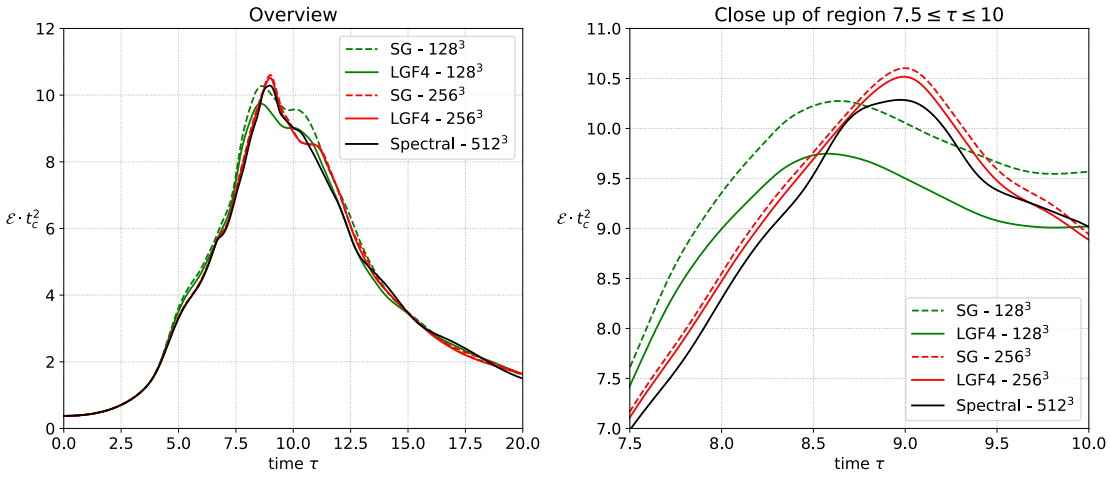

Figure 3.11: Temporal evolution of the global enstrophy for Taylor-Green vortex and for different resolutions. Comparison between Singular Green's function (SG) and Latice Green's Function of order 4 (LGF4).

However, the most significant influence of the choice of the Green's function observed here is on the relationship $\epsilon = 2\nu\mathcal{E}$. Indeed, this equality is not true when SG Green's function is used. Additionally, this analysis is leveraged to consider an alternative form of the energy formula. As seen before, the global kinetic energy is derived with the stream function/vorticity (psi-vel) formulation. However, it could be computed with the classical formulation (vel-vel),

$$E^k = \frac{1}{\rho_0 \Omega} \int_\Omega \rho \frac{\mathbf{u} \cdot \mathbf{u}}{2} d\Omega. \tag{3.17}$$

Figure 3.12 compares the kinetic energy dissipation with their different formulations, and this, for the two Green's functions. The comparison is made on a grid size of 128^3 since the difference is less noticeable for higher resolution, e.g., 256^3 or 512^3. The plot on the right enlarges the most critical part, i.e., corresponding to the peak of enstrophy and, consequently, the dissipation peak. For psi-vel (or similarly for vel-vel) formulation, the curves from SG and LFG4 Green's functions initially overlap. Then, once the peak is reached, they slightly diverge. Hence, the choice of Green's function seems to have a limited impact on kinetic energy. The two formulations of kinetic energy start to diverge sooner, approximately at the time of transition. Indeed, as seen in the zoomed area of the plot on the left, dashed curves deviate earlier from the reference than solid ones. However, both formulations give close results, which is expected since they are theoretically equal. The main difference between Green's functions is the relationship $\epsilon = 2\nu\mathcal{E}$. When the simulation is done

with SG, the kinetic dissipation rate is no longer equal to the enstrophy by one factor. The enstrophy peak reaches a higher value, and this maximum value is closer to the reference values. When using the LGF4 Green's function, it guarantees the equality as we can see in the close-up plot (right) that blue dotted and solid curves overlaps. Note that $2\nu\mathcal{E}$ overlaps the psi-vel formulation and not on the other formulation. However, the enstrophy peak undergoes a non-negligible drop for the lower resolution, e.g., 128^3. This difference is less visible for higher resolution, but it remains present.

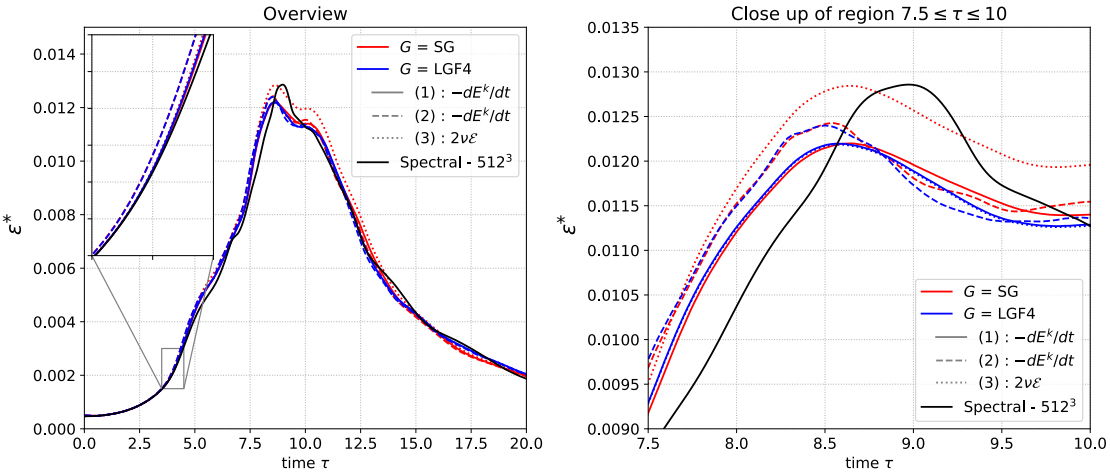

Figure 3.12: Global kinetic energy dissipation for Taylor-Green vortex and with respect to the formulation of kinetic energy: psi-vel formulation (1), vel-vel formulation (2), and $\epsilon = 2\nu\mathcal{E}$ (3), for a grid size of 128^3. The right graph enlarges the dissipation peak.

3.3 Conclusion

In conclusion, the Direct Numerical Simulation of the Taylor-Green vortex test case at a moderate Reynolds number of $Re = 1600$ is done with Murphy, which has the particularity of using the velocity-vorticity formulation of Navier-Stokes equations. The results are compared with the pseudo-spectral method at a resolution of 512^3. Analysis of the time evolution of enstrophy and kinetic energy dissipation, of the energy spectrum and of the vorticity field slices demonstrate strong agreement between Murphy and pseudo-spectral code. Furthermore, an under-resolved simulation with a resolution of 256^3 is performed, leading to reasonable results when compared to the reference. However, when the resolution is further reduced to 128^3, the results are less consistent, although the general trends are preserved. In addition, two Green's functions, singular (SG) and Lattice Green's function of order 4 (LGF4), are investigated to solve the Poisson equation in the spectral domain. While both methods showed similarities in the temporal evolution of kinetic energy dissipation, LGF4 guarantees the relation $\epsilon = 2\nu\mathcal{E}$, which was not observed for the singular Green's function.

Chapter 4

Large Eddy Simulation (LES)

4.1 Introduction

The work presented here aims to investigate Large-Eddies Simulation (LES). Contrary to the DNS, which captures the entire range of scales, LES only resolves large to medium scales. Indeed, the impact of the remaining scales, i.e., small-scales and subgrid scales, on the resolved scales are modeled by means of a subgrid-scale (SGS) model. The grid is deliberately chosen to be too coarse to capture all turbulent structures. The advantage of this kind of model is that it allows a reduction of the grid size and, therefore to decrease the computational resources. Thus, the SGS model is an additional effective dissipation term that aims to reproduce, on largest scales, the effect of the subgrid scales. The smallest resolved scales are smoothly dissipated in the zone of influence of the SGS model, which ranges up to the cut-off wavenumber k_c associated with the mesh, as illustrated in Figure 4.1. This zone of influence is tinted in red in the figure, for the case of an "ideal" SGS model, where only the smallest scales are affected by the SGS dissipation.

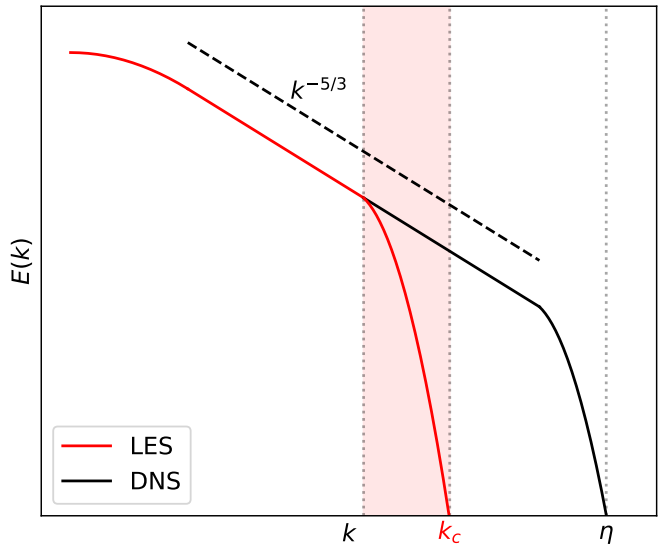

Figure 4.1: Typical energy spectrum of HIT at high Reynolds number, comparison between LES and DNS. The red-tinted area corresponds to the SGS model's "ideal" region of influence.

Before considering any SGS model, we are interested in filtering operators, which are useful for models such as Regularized Variational Multiscale (RVM). The latter differs from the Smagorinsky (SMAG) model in that it uses a filtered version of the vorticity field where only small scales are kept. Once the filtering operation is characterized, the SMAG and RVM models are defined and implemented. Finally, simulations of the Taylor-Green vortex test case are done with SGS models and compared with the previous DNS made with Murphy and the reference, which still is the pseudo-spectral DNS.

4.2 Filtering operators

A field can be described as a sum of several scales. Here, we define the complete scale $u_i = \bar{u}_i + u_i^s$ where $\bar{u}_i$ describes the large scale of the field and where u_i^s corresponds to the small scales. The following development is based on what is done in Jeanmart and Winckelmans [24]. A filtering operator is used to separate the large scale from the field as $\bar{u}_i = \bar{G} * u_i$. Hence, the small scales field is retrieved as $u_i^s = \bar{u}_i - u_i = \bar{G} * u_i - u_i = (\bar{G} - I) * u_i$. The first filter operator investigated is built from compact (stencil 3) discrete filters. Then, the filter is applied on a function $u(x)$ and gives in 1D,

$$\begin{aligned} \bar{u}(x) &= (\bar{G} * u)(x) = (u(x+h) - 2u(x) + u(x-h))/4 \\ &= u(x) + (\delta^2/4)u(x) = (I + \delta^2/4)u(x). \end{aligned} \tag{4.1}$$

Here, we consider a uniform grid with a spacing of h. The notation $\delta^2/4$ is used for the sake of simplicity. The transfer function is given by,

$$\bar{\mathcal{G}}(k) = 1 - (1 - \cos(kh))/2 = 1 - \sin^2(kh/2), \tag{4.2}$$

where k is the wavenumber. The associate filter for the small scales appears by writing $\bar{G}$ as $I - (I - \bar{G})$. Indeed,

$$\bar{u}(x) = u(x) - ((I - \bar{G}) * u)(x) = u(x) - u^s(x). \tag{4.3}$$

Thus, this filter is identified as $(I - \bar{G}) = -\delta^2/4$ and the associated transfer function for small scales filter is $(1 - \bar{\mathcal{G}}(k)) = \sin^2(kh/2)$. The development above corresponds to the 1D case, but the 3D case can be easily derived by operating one direction at a time (tensor-products, $\bar{G} = \bar{G}_x * \bar{G}_y * \bar{G}_z$). Thus, the filtered 3D field is found as,

$$\bar{u}_i(\mathbf{x}) = (I + \delta_x^2/4)(I + \delta_y^2/4)(I + \delta_z^2/4)u_i(\mathbf{x}), \tag{4.4}$$

and the corresponding transfer function reads,

$$\bar{\mathcal{G}}(\mathbf{k}) = (1 - \sin^2(k_x h_x/2))(1 - \sin^2(k_y h_y/2))(1 - \sin^2(k_z h_z/2)). \tag{4.5}$$

This transfer function has the property to be equal to zero on all sides of the cubic wavenumber box ($k_x h_x = \pi$ and $k_y h_y$, $k_z h_z$ arbitrary, etc.). Finally, the field of small scales is obtained as,

$$u_i^s(\mathbf{x}) = (I - (I + \delta_x^2/4)(I + \delta_y^2/4)(I + \delta_z^2/4))u_i(\mathbf{x}). \tag{4.6}$$

However, instead of using the tensor-product filters, we can use "cross based" operations, which provide another expression of the small-scales field in 3D as,

$$u_i^s = -(\delta_x^2/4 + \delta_y^2/4 + \delta_z^2/4)u_i(\mathbf{x}), \tag{4.7}$$

and its associated transfer function reads,

$$1 - \bar{\mathcal{G}}(\mathbf{k}) = \sin^2(k_x h_x/2) + \sin^2(k_y h_y/2) + \sin^2(k_z h_z/2). \tag{4.8}$$

In the case of the "cross-based" filter, the associated transfer function $\bar{\mathcal{G}}(\mathbf{k})$ no longer has the property of being equal to zero on each face of the cubic wavenumber box, but only on each face center ($k_x h_x = \pi$ and $k_y h_y = k_z h_z = 0$, etc.). Thus, as stated by Jeanmart and Winckelmans [24], this filter may not be "as good a high wavenumber smoother" as that of the previous case. However, it has the property to be easy to implement since it corresponds to the application of a crossed Laplacian of second order as $u_i^s = -(h^2/4)\nabla_h^2 u_i$ (which is valid for a uniform grid of same length in all directions). Consequently, filtering operations in the present work are performed using this operator.

For the moment, the filters presented here are of order 2. However, higher order filters can be built by iterating m times the compact stencil-3 operator, producing a $2m$ order filter. Based on previous expressions, these $2m$ order filters are expressed for the "tensor based" operator as,

$$\bar{\mathcal{G}}^m(\mathbf{k}) = (1 - \sin^{2m}(k_x h_x/2))(1 - \sin^{2m}(k_y h_y/2))(1 - \sin^{2m}(k_z h_z/2)). \tag{4.9}$$

And for the "cross-based" operator as,

$$1 - \bar{\mathcal{G}}^m(\mathbf{k}) = (\sin^2(k_x h_x/2) + \sin^2(k_y h_y/2) + \sin^2(k_z h_z/2))^m. \tag{4.10}$$

Hence, as seen in Figure 4.2, the filter is equal to zero for the constant component of the field ($kh = 0$) and one at the LES cutoff wavenumber ($kh = \pi$). The "mid-cutoff" wavenumber is defined as k_{mc} such that $\bar{\mathcal{G}}^{(m)}(k_{mc}h) = 1/2$. This specific wavenumber $k_{mc}h$ can be adjusted by modifying the order of the filter ($k_{mc}h = \pi/2$ for m = 1, $k_{mc}h = 0.636\pi$ for m = 2 or $k_{mc}h = 0.7\pi$ for m = 3). Thus, increasing the order of the filter shifts the "mid-cutoff" wavenumber to the right leading to less consideration of a wider range of large scale.

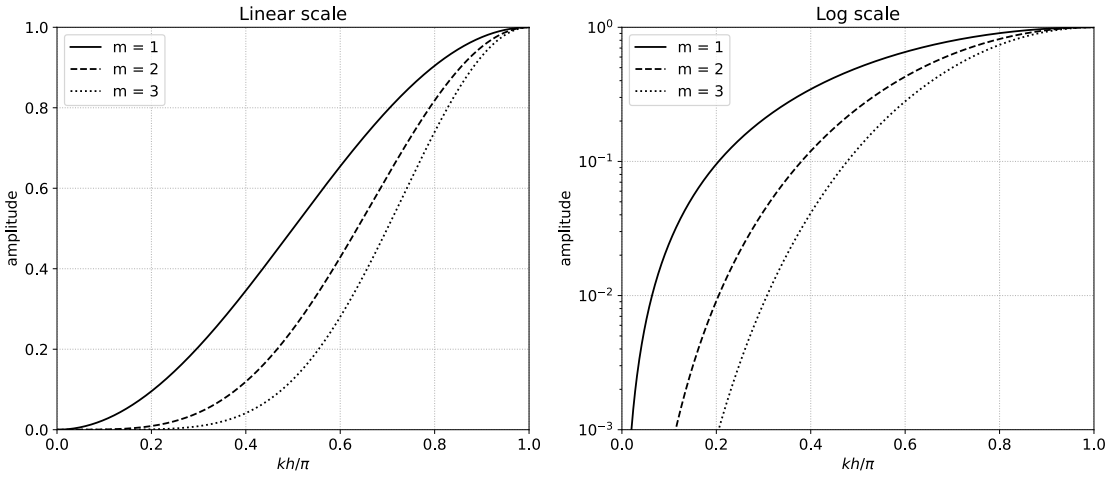

Figure 4.2: Transfer functions (in 1D) for small-scale fields with respect to the order of filter: $m = 1$ (solid), $m = 2$ (dashed), and $m = 3$ (dotted). (Left: linear scale, right: log scale).

Figure 4.3 shows the effect of the filtering operation on a field in a 2D domain, and this, for one and three iterations (the field used here is a slice from the Taylor-Green test case with a 128^3 mesh for illustration purpose). Thus, we can observe that by iterating several times with the same filter, we obtain a field with only the smallest scales of the initial field.

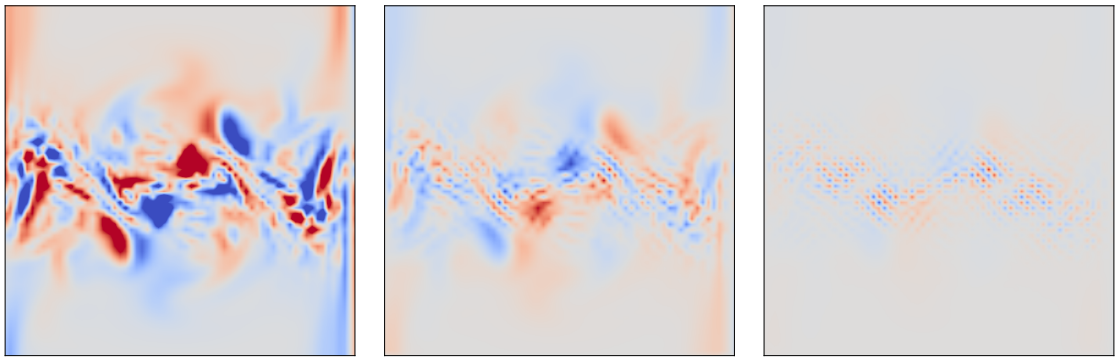

Figure 4.3: Filtering operation over a field. Initial field (left), one iteration of the filter (center), and three iterations of the filter (right).

In the following section, the filter used is the "cross-based" operator since Murphy already uses cross stencil operations to perform finite differences. Note that Murphy also uses wavelet transforms for its multiresolution grid adaptation (not used here), so it might be interesting to use wavelet operators to filter fields since these operators are already available in the code.

4.3 Subgrid-scale (SGS) models

The implementation of LES for an incompressible vortex flow is done with an effective SGS viscosity ν_{sgs}. Based on this effective viscosity, a new term is added to the vorticity/velocity formulation of Navier-Stokes equations. Several models of LES exist and can act either on the complete field or on the small-scale field. Hence, two equations are given by Cocle, Dufresne, and Winckelmans [9],

$$\frac{D\boldsymbol{\omega}}{Dt} = (\boldsymbol{\omega}\cdot\nabla)\mathbf{u} + \nu\nabla^2\boldsymbol{\omega} + \nabla\cdot(\nu_{sgs}(\nabla\boldsymbol{\omega} - (\nabla\boldsymbol{\omega})^T), \tag{4.11}$$

$$\frac{D\boldsymbol{\omega}}{Dt} = (\boldsymbol{\omega}\cdot\nabla)\mathbf{u} + \nu\nabla^2\boldsymbol{\omega} + \nabla\cdot(\nu_{sgs}(\nabla\boldsymbol{\omega}^s - (\nabla\boldsymbol{\omega}^s)^T), \tag{4.12}$$

where $(.)^s$ means that the fields has been filtered to only keep the small scales. In this expression, the LES term has been written as $\nabla\cdot(\nu_{sgs}(\nabla\boldsymbol{\omega} - (\nabla\boldsymbol{\omega})^T)$. However it can be expressed as $-\nabla\times(\nu_{sgs}\nabla\times\boldsymbol{\omega})$. Indeed, one can prove that,

$$\begin{aligned} -\nabla\times(\nu_{sgs}(\nabla\times\boldsymbol{\omega})) &= (\nabla\times\boldsymbol{\omega})\times\nabla\nu_{sgs} + \nu_{sgs}\nabla^2\boldsymbol{\omega} \\ \equiv \nabla\cdot(\nu_{sgs}(\nabla\boldsymbol{\omega} - (\nabla\boldsymbol{\omega})^T) &= (\nabla\boldsymbol{\omega} - (\nabla\boldsymbol{\omega})^T)\cdot\nabla\nu_{sgs} + \nu_{sgs}\nabla^2\boldsymbol{\omega}, \end{aligned} \tag{4.13}$$

by using vector identity,

$$(\nabla\times\boldsymbol{a})\times\boldsymbol{b} = (\nabla\boldsymbol{a} - (\nabla\boldsymbol{a})^T)\cdot\boldsymbol{b}. \tag{4.14}$$

This reformulation has the property not to produce divergence since $\nabla\cdot(\nabla\times a) = 0$, no matter the value of the field a.

Also, equations 4.11 and 4.12 are rewritten in their Eulerian expression to recover the expression implemented in Murphy, with the same development as seen in Chapter 2. Finally, the equations considered here and which are implemented in the code are written as,

$$\frac{\partial \boldsymbol{\omega}}{\partial t} = \nu \nabla^2 \boldsymbol{\omega} + \nabla \times ((\nabla \times \mathbf{u}) \times \mathbf{u}) - \nabla \times (\nu_{sgs}(\nabla \times \boldsymbol{\omega})), \tag{4.15}$$

$$\frac{\partial \boldsymbol{\omega}}{\partial t} = \nu \nabla^2 \boldsymbol{\omega} + \nabla \times ((\nabla \times \mathbf{u}) \times \mathbf{u}) - \nabla \times (\nu_{sgs}(\nabla \times \boldsymbol{\omega}^{\boldsymbol{s}})). \tag{4.16}$$

4.3.1 Smagorinsky model (SMAG)

The first implemented model is the Smagorinsky (SMAG) model, which is the most common "complete-complete" model. Indeed, both effective SGS viscosity and LES term act on the complete field. The SMAG model gives the effective viscosity ν_{sgs} as,

$$\nu_{sgs} = C_s h^2 (2 S_{ij} S_{ij})^{1/2}, \quad \text{where} \quad S_{ij} \triangleq \frac{1}{2}(\frac{\partial u_i}{\partial x_j} + \frac{\partial u_j}{\partial x_i}). \tag{4.17}$$

[9]

The coefficient is set to the theoretical value as $C_s = (0.3)^3 = 0.027$, corresponding to the case of isotropic turbulence at high Reynolds number. The product of strain rate tensor $S_{ij}S_{ij}$ can be developed into a sum of derivatives as,

$$\begin{aligned} S_{ij}S_{ij} = &\left(\frac{\partial u_x}{\partial x}\right)^2 + \left(\frac{\partial u_y}{\partial y}\right)^2 + \left(\frac{\partial u_z}{\partial z}\right)^2 + \\ &\frac{1}{2}\left(\frac{\partial u_x}{\partial y} + \frac{\partial u_y}{\partial x}\right)^2 + \frac{1}{2}\left(\frac{\partial u_y}{\partial z} + \frac{\partial u_z}{\partial y}\right)^2 + \frac{1}{2}\left(\frac{\partial u_z}{\partial x} + \frac{\partial u_x}{\partial z}\right)^2. \end{aligned} \tag{4.18}$$

4.3.2 Regularized Variational Multiscale (RVM) model

Then, a second model is investigated. The regularized variational multiscale model (RVM) is a "complete-small" model, as it acts on the small-scale field, i.e., a filtered version of the vorticity field, while the SGS viscosity still uses the complete field. Thus, the Navier-Stokes equation is equation 4.16. The effective viscosity ν_{sgs} is the same as for the SMAG model except for one constant,

$$\nu_{sgs} = C_R^{(m)} h^2 (2 S_{ij} S_{ij})^{1/2}, \tag{4.19}$$

where the index m corresponds to the number of iterations of the chosen filter. The choice of the constant $C_R^{(m)}$ is motivated by two factors, identified as the ratio of scales and the order of the filter. The development is the one proposed by Cocle, Dufresne, and Winckelmans [9]. At first, a value for $C_R^{(1)}$ can be found based on the approximation of $|S|^2 \simeq |\bar{S}|^2 + |S^s|^2$ and using the values proposed in Hughes et al. [21]. Indeed, the latter gives coefficients for the "large-small" ($2.62C_s$) and "small-small"

$(1.64C_s)$ models, and based on these, the ratio of small scales and large scales can be estimated as $|S^s|/|\bar{S}| \simeq 2.62/1.64 = 1.60$. Then, the ratio of complete and large scales is found with the previous approximation as $|S|/|\bar{S}| \simeq \sqrt{2.62^2 + 1.64^2}/1.64 = 1.88$. Finally, these values lead to $C_R^{(1)} \simeq (2.62/1.88)C_s = 1.39C_s$.

Then, also as done in Cocle, Dufresne, and Winckelmans [9], the order of the filter is taken into account to determine the coefficients $C_R^{(m)} = \alpha^{(m)} C_R^{(1)}$. Thus, coefficient $\alpha^{(m)}$ corresponds to the shift of the "mid-cutoff" wavenumber $k_{mc}^{(m)}h$ with respect to $k_{mc}^{(1)}h = \pi/2$, introduced by iterating the filter several times as observed in Figure 4.2. From a mathematical point of view, the condition reads,

$$\mathcal{G}^{(m)}(\alpha^{(m)}\pi/2) = 1 - \sin^{(2m)}(\alpha^{(m)}\pi/4) = \mathcal{G}^{(1)}(\pi/2) = 1/2, \tag{4.20}$$

and this provides $\alpha^{(2)} = 1.27$ and $\alpha^{(3)} = 1.40$.

4.3.3 SGS models applied on Taylor-Green test case

Hence, both SMAG and RVM models are implemented in Murhpy. In order to investigate the effect of these models, the Taylor-Green vortex test case is once again used as it corresponds to an isotropic turbulent flow. Aubard et al. [1] as well as Drikakis et al. [12] and DeBonis [11] also tested SGS models with this test case. Initial conditions and numerical setup are exactly the same as in the DNS case, see Chapter 3, except that the grids are coarser. Indeed, the effect of these SGS models decreases quadratically with respect to the grid size. The figure 4.4 shows the influence of coarse grids on global kinetic energy diagnostic without any SGS model. As stated by Aubard et al. [1], the case of 64^3 dof is a good agreement to conduct LES comparisons since the latter gives satisfactory results, as both the transition region and the turbulence production peaks are near, but without directly overlapping the DNS reference.

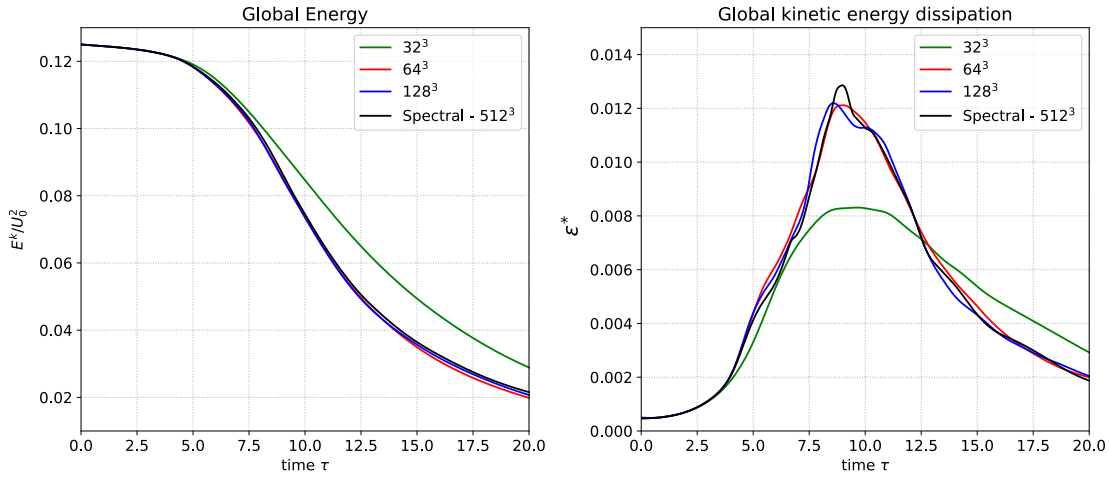

Figure 4.4: Influence of the resolution on global kinetic energy and global kinetic energy dissipation for the Taylor-Green vortex.

Hence, simulations are done for both models and for two grid sizes: 64^3 and 128^3. Table 4.1 tabulates the physical times required for each simulation. It should be noted that the introduction of a SGS model increases the physical computation time for a same number of CPUs. Furthermore, RVM model requires more time than SMAG model since it also has to filter the vorticity field three times at each time step. However, if these SGS models manage to model small scales correctly, the gain realized by reducing the grid size outweighs this loss.

Model	# dof	# Blocks	# CPU	Physical Time [Hour]
NoLES	64^3	8	8	0.23
SMAG	64^3	8	8	0.27
RVM	64^3	8	8	0.4
NoLES	128^3	64	64	0.45
SMAG	128^3	64	64	0.55
RVM	128^3	64	64	0.88

Table 4.1: Comparison of approximated physical times with respect to dof and SGS model.

For the SMAG model, as mentioned before, we set the coefficient $C_s = 0.027$. For the RVM model, the "cross-based" operator filter (equation 4.10) is iterated three times on the vorticity field, thus $\alpha^{(3)} = 1.4$ and $C_R^{(3)} = \alpha^{(3)} 1.39 C_s = 0.052542$.

Note that the enstrophy is no longer relevant when a SGS model is added to the Navier-Stokes equation. Indeed, these models increase dissipation to the simulations, damp large-scale turbulent structures, and strongly decrease enstrophy, as mentioned by DeBonis [11]. Hence, the relationship $\epsilon = 2\nu\mathcal{E}$ is not valid anymore, and the metric of interest here is the global kinetic energy and the kinetic dissipation.

As shown in Figure 4.5, the SMAG model over-dissipates in the transition period. Indeed, the kinetic dissipation rate increases ahead of time and diverges relatively early as compared to the reference for both 64^3 and 128^3 cases. As observed by DeBonis [11], at the beginning of the simulation, the flow consists in large coherent structures and does not exhibit small-scale turbulence. As a result, the sub-grid models, which are unnecessary in this case, generate additional dissipation that contributes to the overall dissipation of the simulation. Following this, the turbulence production peak is shifted earlier, with an underestimation of its maximum for the resolution of 64^3. Beyond this time, the flow is fully turbulent, and the dissipation from the model appropriately dampens the large turbulent structures that are the main dissipation process. The same conclusion is drawn by Aubard et al. [1], "The Smagorinsky model, even in its dynamic form, appears to be too dissipative and describes poorly the laminar turbulent transition region. The dissipation effect is triggered to early resulting in a shift of the peak dissipation toward earlier times"

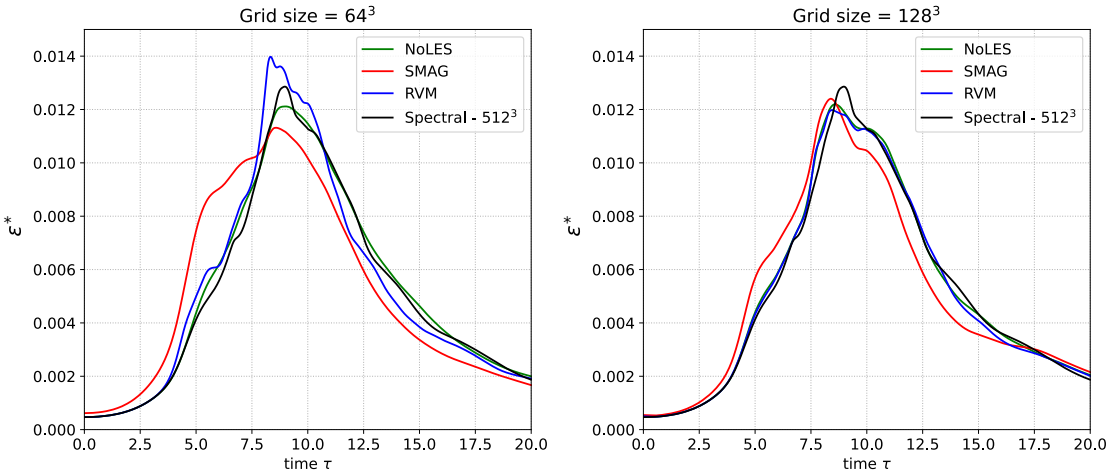

Figure 4.5: Temporal evolution of the global kinetic energy dissipation for Taylor-Green vortex and for resolution of 64^3 (left) and 128^3 (right). Comparison between SMAG and RVM models.

For the case of RVM model, the results for the resolution of 128^3 are very similar to the case without any model, with the exception of a slight underestimation of the peak of dissipation. However, for 64^3, we observe an early dissipation in the turbulence transition, but, unlike the SMAG model, an overestimation of the enstrophy peak appears, and its maximum is slightly ahead of the reference. By filtering the vorticity field, the over-dissipation of the SGS model starts later, as it is necessary to wait for the flow to produce small eddies in order for the model to take effect.

The Figure 4.6 compare the energy spectrum for simulations with and without SGS model. These models used in SMAG and RVM model acts like a low-pass filter. Indeed, as seen in the figure, the energy is lower for small scales right above the cut-off wavenumber k_c with SGS model. For the case of SMAG model, a wide range of scales is affected by the additional dissipation, and the corresponding spectrum faces a reduction of energy since the model acts on the complete field. However, the smallest scales are still the most affected. For the case of RVM model, a smaller range of scales near the cut-off frequency is affected by the additional dissipation, which dissipate higher than the SMAG model, while the large scales are very close to the case without any model. Indeed, the filtering operation used in RVM model allows the model to act only in the small-scale field. Hence, the RVM model is closer to the "ideal" SGS model as illustrated in Figure 4.1.

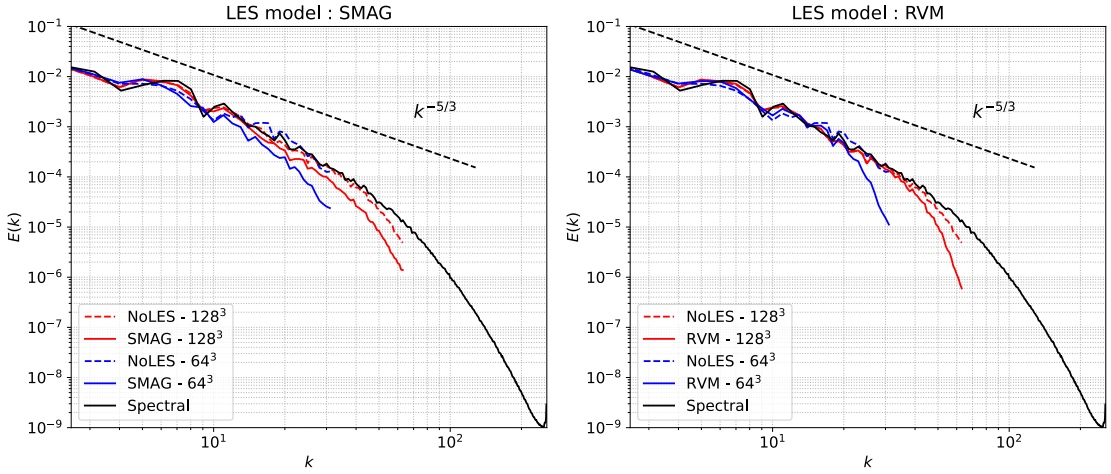

Figure 4.6: Complete energy spectrum of the Taylor–Green vortex and for resolution of 64^3 and 128^3. Comparison between SMAG (left) and RVM (right) model, for $\tau = 9$.

Figure 4.7 illustrates, in the same way as DeBonis [11], the impact of models on the resolved structures. Thus, the overall shape of the field is better maintained and smoothed out - this is especially true for the SMAG model over the RVM model. However, adding a model has the consequence of reducing the maximum value of vorticity norm. DeBonis [11] also observed this behavior with both the SMAG and dynamic SMAG models.

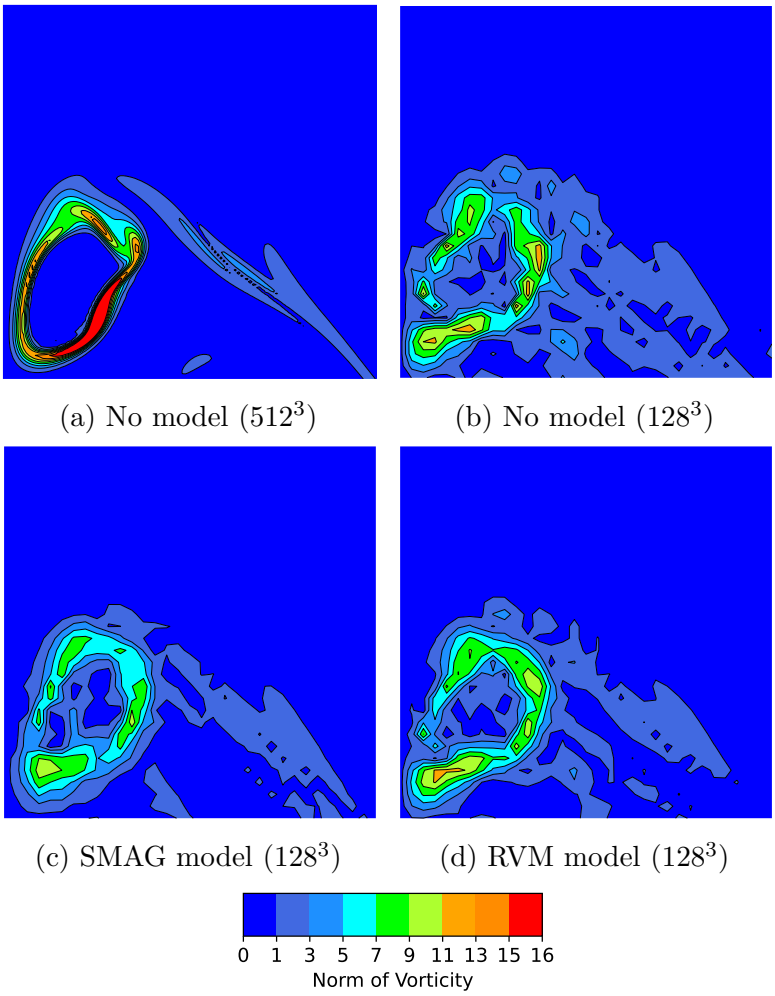

(a) No model (512^3) (b) No model (128^3)

(c) SMAG model (128^3) (d) RVM model (128^3)

Figure 4.7: Dimensionless vorticity norm at $\tau = 8$, iso-contours of $\omega^* = L/U_0|\boldsymbol{\omega}|$, the plane is a slice of the domain at $y/L = 0$, in the region $x = 0$ to $x = L/4$ and $z = 3L/4$ to $z = L$. Comparison of SMAG and RVM models.

4.4 Conclusion

In conclusion, two SGS models are implemented in Murphy. The first one is the "complete-complete" SMAG model, and the second one is the "complete-small" RVM model. Their objective is to model the impact of small and under-resolved scales on large scales to be able to reduce the grid size while maintaining satisfactory results. These SGS models are tested with an under-resolved simulation of the Taylor-Green vortex test case. Thus, no significant improvements are observed in comparison to the DNS for the evolution of kinetic energy dissipation. Indeed, the SMAG model tends to dissipate too early, as observed by Aubard et al. [1]. For the RVM model, the dissipation starts slightly earlier than the reference, and at a lower resolution, it overestimates the dissipation peak. One could study the impact of coefficient C_s to fit the curve better. Observation of the spectrum shows that the models have the expected effect. Indeed, scales before the cut-off wavenumber k_c associated with the mesh are well dissipated by the SGS model. However, the SMAG model also tends to dissipate larger scales, while the RVM model limits itself to a tighter range, preserving the largest scales, as expected.

Chapter 5

No-through flow boundary condition

5.1 Introduction

The implementation of a no-through flow boundary condition is a necessary step in order to implement the no-slip boundary condition. This chapter explains how this first condition is set in the code. Once the condition is correctly added, the latter is validated with the vortex-rings reconnection test case, as done by Lepot [29]. Indeed, this boundary condition behaves like a plane of symmetry, and it is able to reproduce the interaction with a second ring. We also compare the results obtained by Jacquemin [23], which directly simulates two rings.

5.2 Expression of the boundary condition

The no-through flow boundary conditions require the right combination of odd and even extensions of the components of the fields at the wall. Indeed, the Poisson solver considers that there is a perfectly symmetric flow on the other side of the boundary plane. Hence, this plane acts like a symmetric plane, and the flow can interact with its symmetry, although the latter is not in the computational domain.

Hence, the case of walls on both sides is considered, as shown in Figure 5.1.

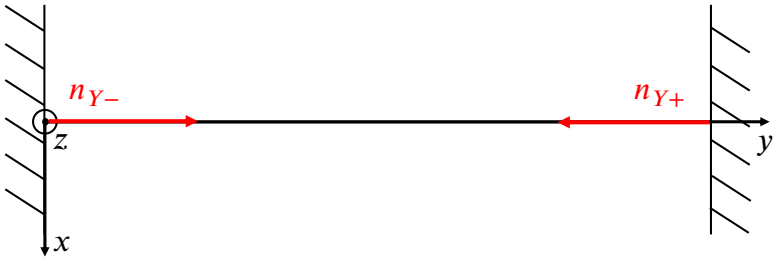

Figure 5.1: No-through flow boundary conditions on opposite walls.

From a code point of view, imposing even and odd conditions corresponds to imposing, respectively, Neumann and Dirichlet conditions. For the velocity, these conditions cancel the normal velocity, but they still allow diffusion through the wall.

$$\begin{aligned} \frac{\partial u_x}{\partial y} &= 0, \\ u_y &= 0, \\ \frac{\partial u_z}{\partial y} &= 0. \end{aligned} \tag{5.1}$$

Then, the vorticity field must have consistent boundary conditions with the velocity. Hence, the vorticity at the wall reads,

$$\begin{aligned} \omega_x &= 0, \\ \frac{\partial \omega_y}{\partial y} &= 0, \\ \omega_z &= 0. \end{aligned} \tag{5.2}$$

5.3 Validation : Vortex-rings reconnection

As a validation of the no-through flow boundary condition, a vortex ring reconnection test case at $Re_\Gamma = 2000$ is proposed as it is done by Lepot [29]. Our results are also compared with the ones from Jacquemin [23]. Note that the latter simulates two distinct rings instead of imposing a symmetry plane, and with a higher Reynolds number of $Re_\Gamma = 5000$. When two vortex tubes have co-planar central lines and interact together, three phenomena can happen depending on the sign and the magnitude of the rings. The case that interests us here is when they have opposed signs with equal magnitude. When these conditions meet, the two tubes reconnect to form one single ring. Thus, from the no-through boundary, we will be able to get this phenomenon since the ring will interact with its symmetry, which guarantees both conditions for reconnection.

5.3.1 Initial condition and numerical setup

A vortex ring is a torus-shaped vortex tube whose vorticity profile is axisymmetric. Thus, only the component ω_θ is non-zero. From the velocity due to the vorticity field, the ring moves in the direction of its normal, i.e., the normal of the plane where the torus lies. Several vorticity profiles exist to generate a vortex ring. We base ourselves on the one used by Lepot [29], so the function employed will be the one of a compact ring, which reads,

$$\frac{\pi \omega_\theta \sigma^2}{\Gamma} = \begin{cases} C(\beta^2) \exp\left(-\frac{\rho^2}{\beta^2(1-\rho^2)}\right) & \text{if } \rho \leq 1 \\ 0 & \text{otherwise} \end{cases} \tag{5.3}$$

To generate a ring from this profile, we define $\rho = s/R_c$ with $s^2 = z^2 + (r - R)^2$, where r corresponds to the distance between the center of the ring and a point in the domain. R is the distance from the center of the torus to the center of the tube, and R_c is the radius of the tube. The parameter β, defined as $\beta = \sigma/R_c$, corresponds to the dimensionless standard deviation of the compact Gaussian profile. Finally, the circulation of the ring is forced to be equal to Γ by choosing the right constant $C(\beta^2)$. Indeed, the circulation is,

$$\Gamma = \int_S \omega_\theta(s) dS = \int_0^{2\pi} \int_0^{R_c} \omega_\theta(s) s ds d\theta, \tag{5.4}$$

and by replacing the vorticity ω_θ by the expression from Equation 5.3, it becomes,

$$\Gamma = 2\pi \int_0^{R_c} C(\beta^2) \frac{\Gamma}{\sigma^2 \pi} \xi(s/R_c) s ds \iff 1 = 2 \int_0^1 C(\beta^2) \frac{1}{\beta^2} \xi(\rho) \rho d\rho, \tag{5.5}$$

where $\xi(\rho) = \exp\left(-\frac{\rho^2}{\beta^2(1-\rho^2)}\right)$.

This allows us to obtain the condition on $C(\beta^2)$ as,

$$C(\beta^2) = \left(2 \int_0^1 \frac{1}{\beta^2} \exp\left(-\frac{\rho^2}{\beta^2(1-\rho^2)} \right) \rho d\rho \right)^{-1}. \tag{5.6}$$

The quantities are set to the same values as those proposed by Lepot [29]. Therefore, $\Gamma = 1$, $R_c/R = 1/2$, $\beta = 1/4$, and by using relation 5.6, we obtain $C(\beta^2) = 1.11866$. The profile of dimensionless vorticity ω_θ is shown in Figure 5.2. For $\rho > 1$, the vorticity equals zero, and the compact Gaussian function connects smoothly to this value at $\rho = 1$.

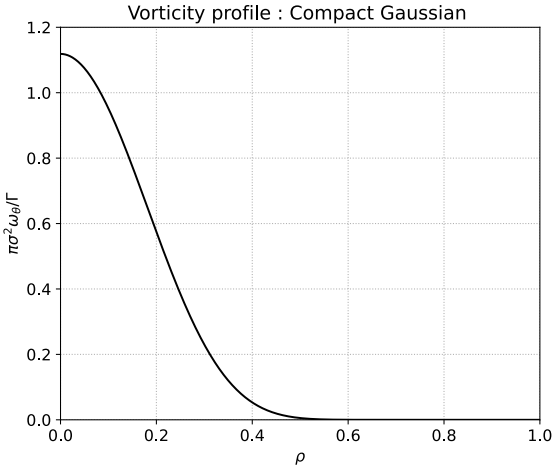

Figure 5.2: Compact ring profile.

The dimensionless time is defined as $\tau = t/t_c$, where the characteristic time is $t_c = R^2/\Gamma$. From preliminary simulations, i.e., with lower grid size (128^3 and 256^3), and an enstrophy analysis based on Figure 5.9, we observe that the reconnection starts at $\tau \simeq 4.5$ and completes at $\tau \simeq 7.5$. Thus, the final time can be set at $\tau = 10$ in order to capture the entire reconnection process. The reference vorticity is defined as $\omega_0 = \max(||\omega||_{t=0}) = 569.72$ and corresponds to the dimensionless factor for vorticity.

The domain is a cube with no-through flow boundary conditions on $\hat{e}_y$ faces, and all other faces are set with unbounded boundary conditions, as represented in Figure 5.3. This domain is split into 16^3 sub-blocks with each 32^3 dof. This simulation runs on 256 processors to achieve $\tau = 10$ after 4.36 hours of physical time.

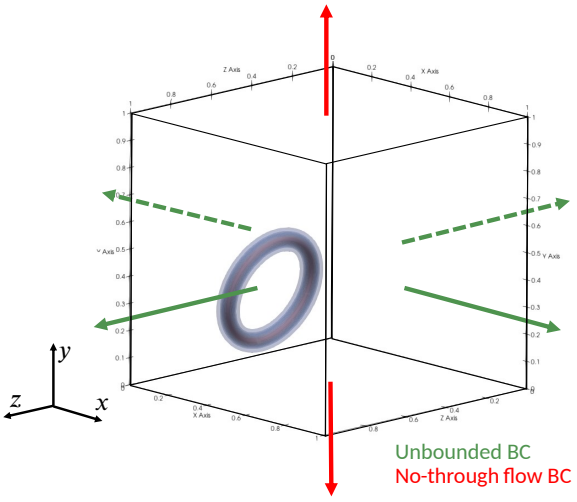

Figure 5.3: Boundary conditions for vortex-rings reconnection.

$Re_\Gamma = \Gamma/\nu$	N_x	N_y	N_z	L_x/R	L_y/R	L_z/R	t_c [s]
2000	512	512	512	5.0	5.0	5.0	25.0

Table 5.1: Numerical parameters for the simulation of the vortex-ring reconnection.

The initial condition for the vorticity is shown in Figure 5.4. The domain for $y < 0$, faded in white, is the symmetry of the flow, and it is not in the computational domain. The compact ring is placed in the $\hat{e}_y$ direction such that it does not touch the wall at $\tau = 0$, but is close enough to interact with it in a short time. Thus, the distance S, between the center of the ring and the center of the symmetric ring is $S/R = 3$. For the longitudinal position $\hat{e}_x$, the center is placed on the left of the domain in order to let the ring flow. Hence, the coordinate of the center of the ring is $(x/R, y/R, z/R) = (1, 1.5, 2.5)$. The angle of incidence is $\theta = 15°$ and defines the direction in which the ring moves.

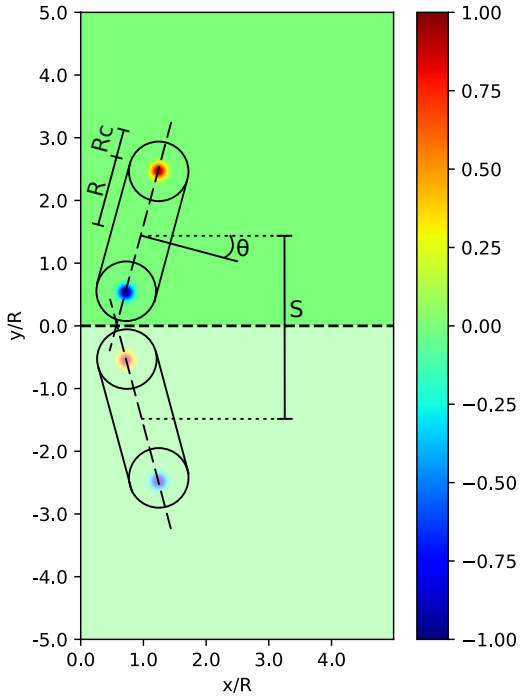

Figure 5.4: Initial condition for vorticity field. Slice of the dimensionless vorticity ω_z/ω_0 at $z = L_z/2$ for $\tau = 0$.

5.3.2 Results and discussion

As done for the DNS simulation of Taylor-Green test case, the mesh Reynolds number based on vorticity is computed and shown in Figure 5.5.

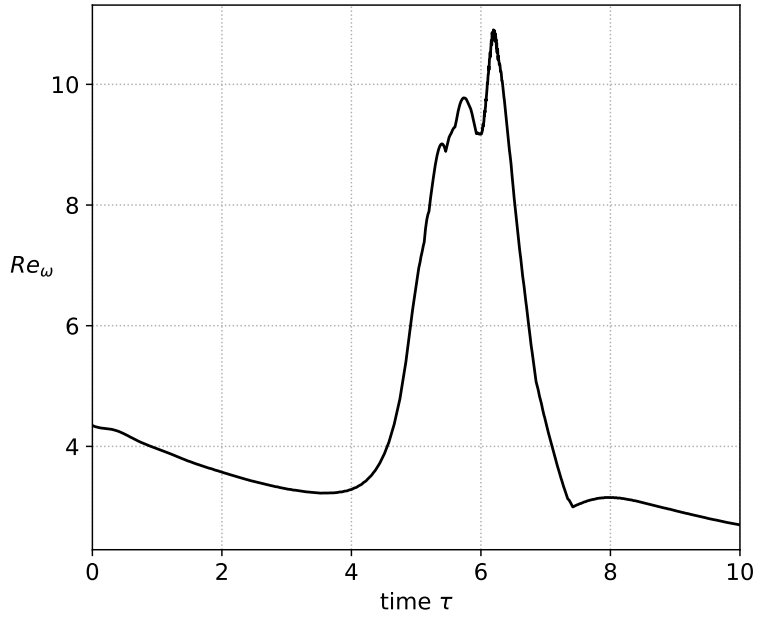

Figure 5.5: Mesh Reynolds number based on vorticity, for the vortex ring reconnection.

Figure 5.6 and Figure 5.7 show vorticity ω_z respectively in the plan XY-plane at $z = L_z/2$ and in the plan XZ-plane at $y = 0$ and for different times. The three dimensions views of isocontours of the vorticity norm are presented in Figure 5.8.

As described by Jacquemin [23], three phases of the reconnection proccess are recognizable. At first, the non-viscous advection for $\tau < 4.9$, the ring gets closer to the symmetry plane, corresponding to a mutual approach of both rings, with negligible viscous dissipation. Then, the rings meet and flatten out on top of each other. From this starts the reconnection phase (bridging) from $\tau > 4.9$ to $\tau < 6.5$. The vorticity diffuses through the wall, and vortex lines connect from direction x toward y. Beyond this moment, for $\tau > 6.5$, comes the threading phase. The residual threads are stretched by the bridges, roll up around them, and thus fade out progressively. Note that the residual vorticity from threads takes a long time to vanish. Finally, both vortex rings are reconnected but through a topology change.

We observe the same results as Lepot [29]. The results from Jacquemin [23] are similar. As a reminder, the latter simulates two distinct rings instead of imposing a symmetry plane, and for a higher Reynolds number $Re_\Gamma = 5000$. Thus, the same results are not expected, but we notice very similar reconnection behavior in both cases.

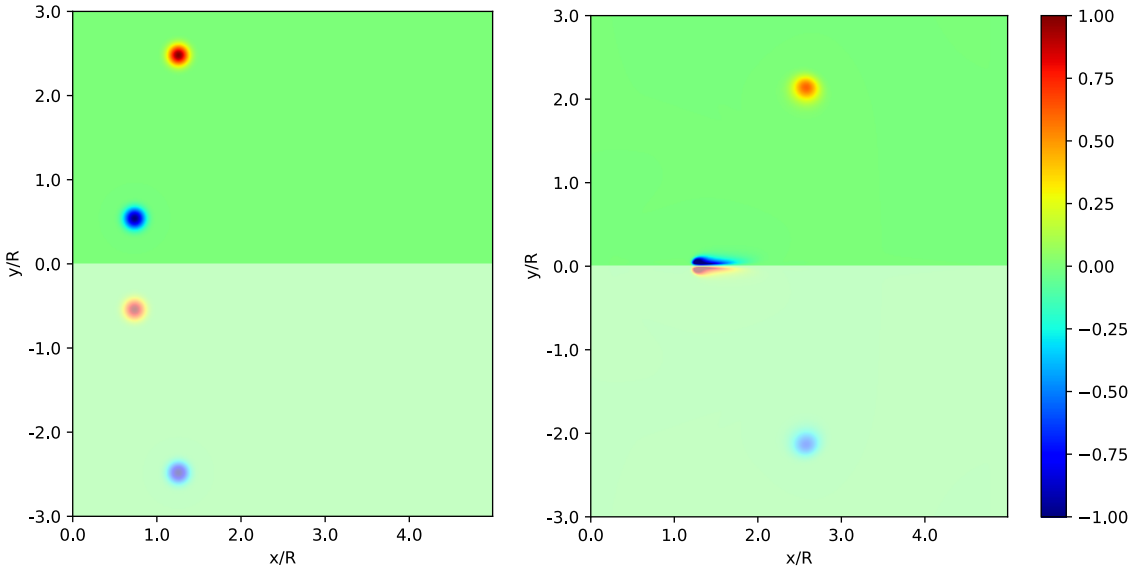

(a) $\tau = 0$ (b) $\tau = 5$

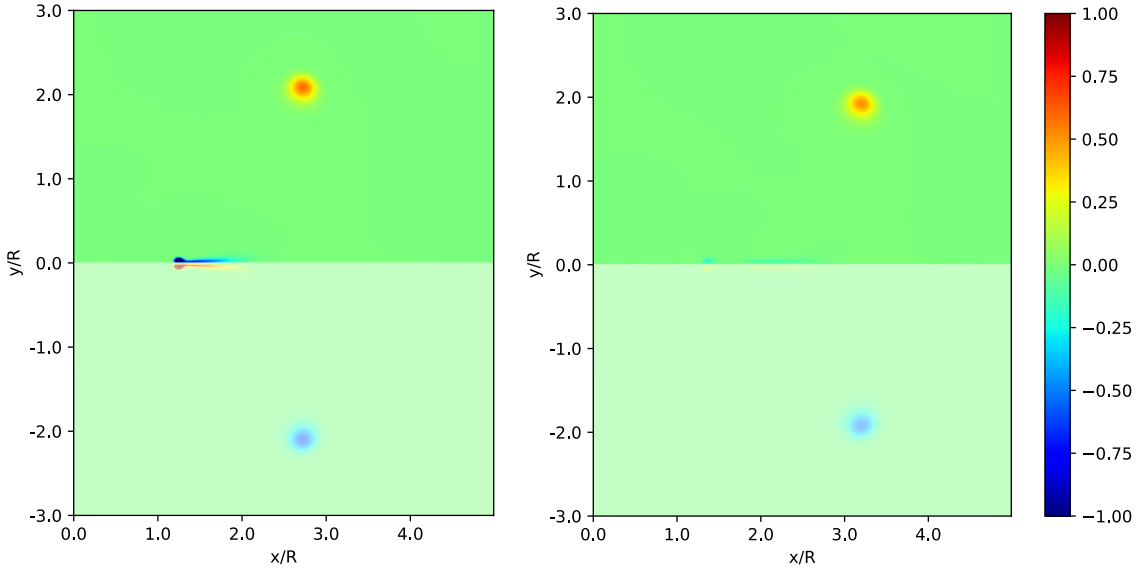

(c) $\tau = 5.5$ (d) $\tau = 7.5$

Figure 5.6: Slice of dimensionless vorticity ω_z/ω_0 in the plane $z = L_z/2$ for different times. Domain faded in white is the symmetrical flow.

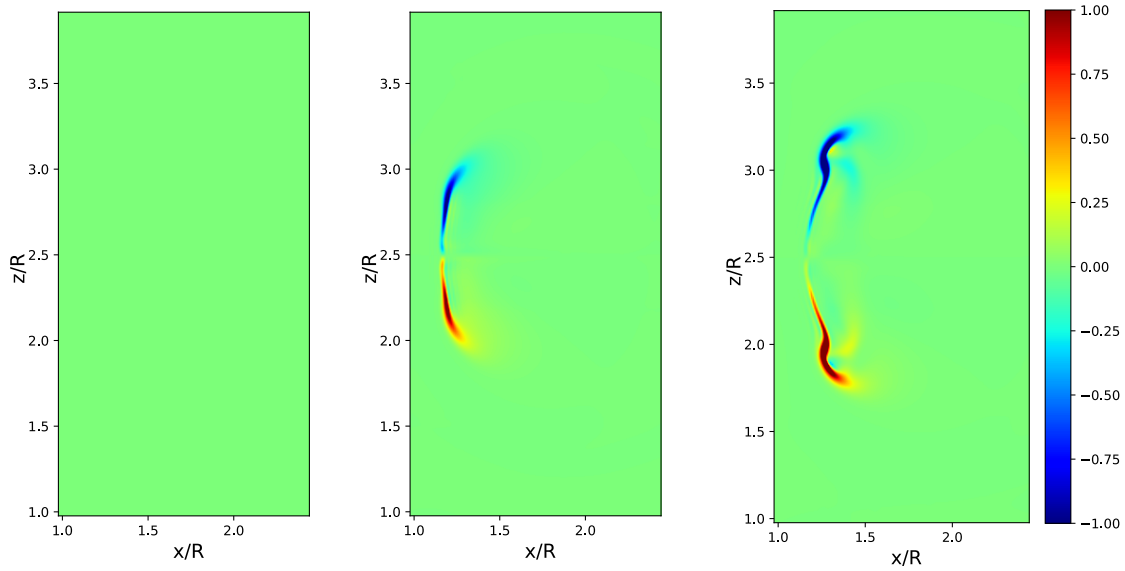

(a) $\tau = 0$ (b) $\tau = 5.5$ (c) $\tau = 6$

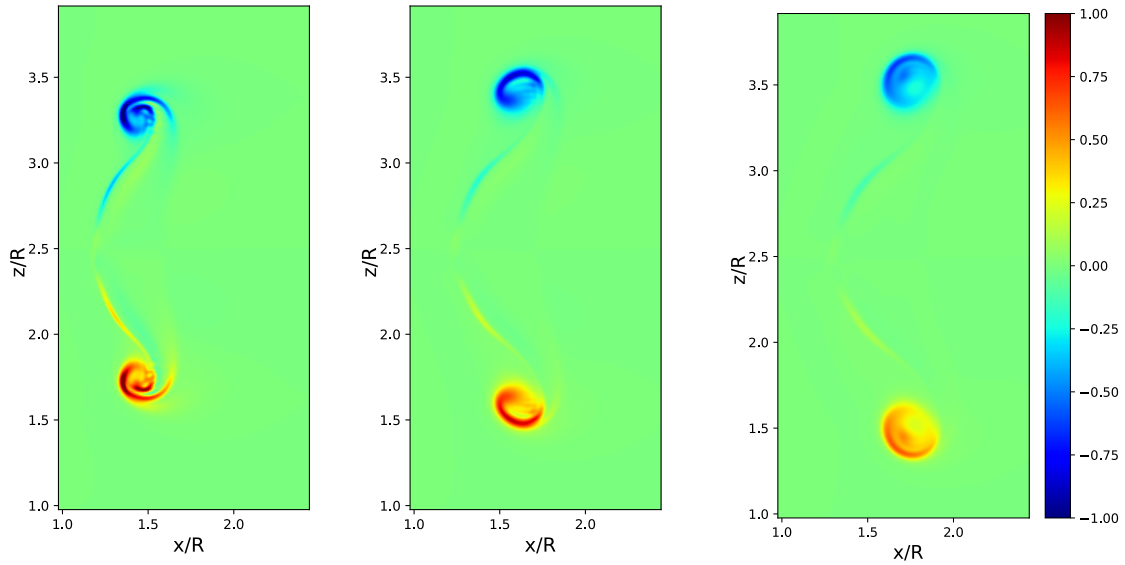

(d) $\tau = 6.5$ (e) $\tau = 7$ (f) $\tau = 7.5$

Figure 5.7: Slice of dimensionless vorticity ω_z/ω_0 in the plane $y = 0$ for different times.

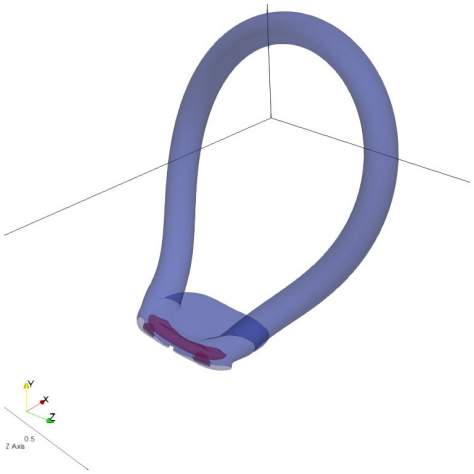

(a) $\tau = 5.5$

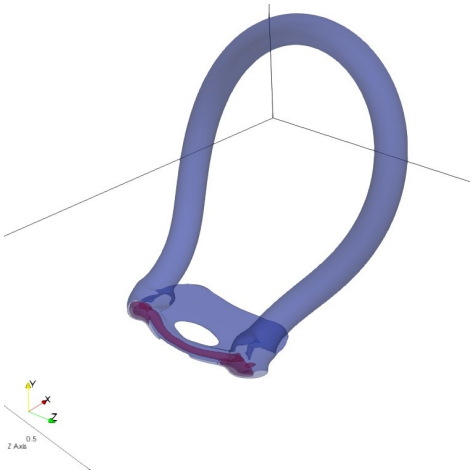

(b) $\tau = 6$

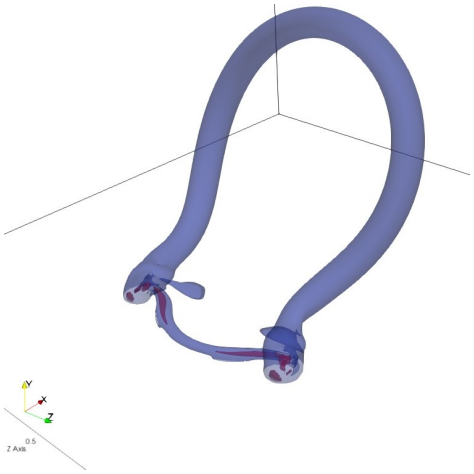

(c) $\tau = 6.5$

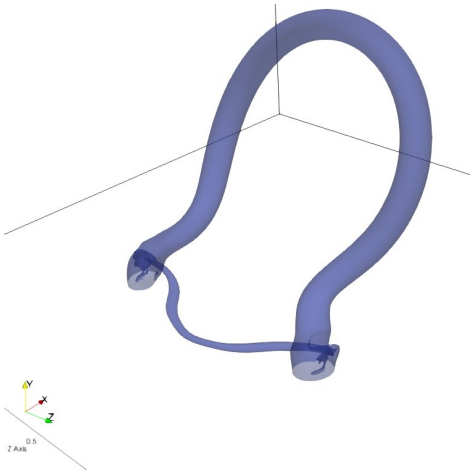

(d) $\tau = 7$

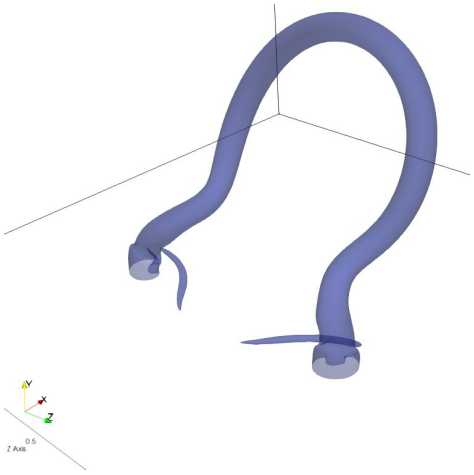

(e) $\tau = 7.5$

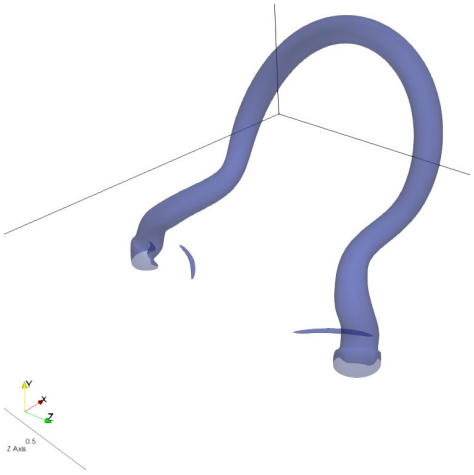

(f) $\tau = 8$

Figure 5.8: Isocontour of the dimensionless vorticity norm, $||\omega||/\omega_0 = 1$ (red) and $||\omega||/\omega_0 = 0,3$ (blue).

The evolution of enstrophy is shown in Figure 5.9. Three distinct phases can be observed from the figure, corresponding to different flow processes, as identified above. At first, the vortex ring diffuses in the domain, and the enstrophy decreases over time. Then, starting from $\tau \simeq 4.25$, the enstrophy starts to increase from the flattening of the ring on the boundary. From this time, the three resolutions start to diverge. Indeed, the reconnection starts, and the vortex structures become more complex. Thus, it requires a finer mesh to capture them adequately. The enstrophy achieves a peak at $\tau = 5.3$, and this local maximum is the expression of the initiation of the bridges and the formation of the threads, as explained by Jacquemin [23]. This phase lasts a relatively short period, and after $\tau \simeq 7.5$, the ring is reconnected and continues to diffuse, leading to a further reduction of enstrophy. Note that even if the enstrophy is very similar between the different grid sizes, only the finest resolution, i.e., 512^3, leads to correctly capturing all scale vortex at the interface.

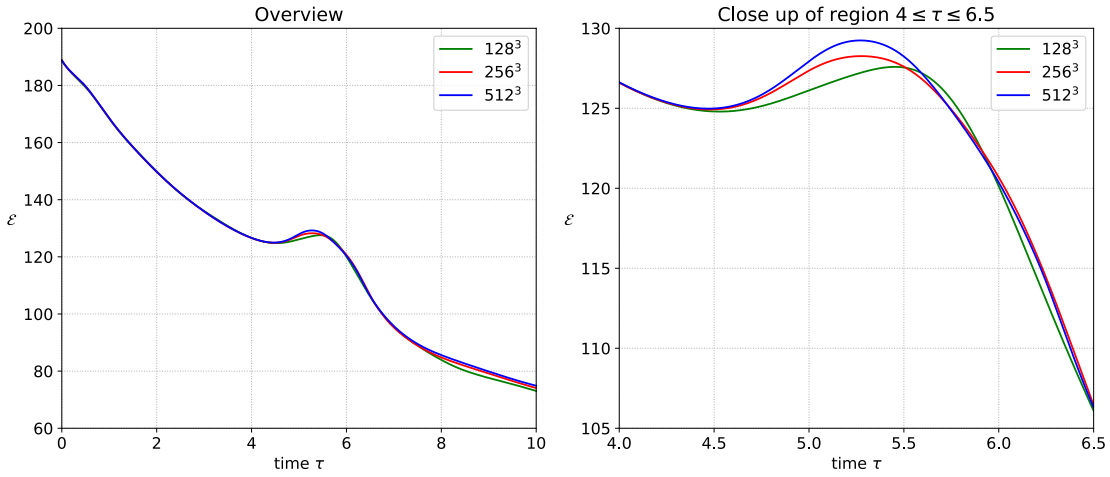

Figure 5.9: Evolution of global enstrophy for vortex ring reconnection and for different resolutions.

5.4 Conclusion

The no-through boundary condition is implemented in Murphy. Based on the results from the vortex-rings reconnection test case, we can state that the boundary condition works appropriately. Indeed, the ring reconnects with its symmetry. Furthermore, these results are very similar to those from Lepot [29], and the behavior of the reconnection is also close to the one described by Jacquemin [23], the differences coming from the different Reynolds number and from the fact that the latter simulates two rings. Thus, the next step is to use this condition to impose the no-slip boundary condition.

Chapter 6

No-slip boundary condition

6.1 Introduction

Now that the no-through-flow condition has been correctly implemented, the no-slip condition is added to the code, following the development of Lepot [29]. The latter uses a vortex particle-mesh code, whereas Murphy is Eulerian. However, the condition imposed on the vorticity is the same as required in our present case. Indeed, both use vorticity-velocity formulation of the Navier-Stokes equation and imposing the velocity $\mathbf{u} = 0$ at the wall is not sufficient, as it could be done in a velocity-pressure code. Hence, a vortex-sheet is computed at the wall by using the velocity right above. At first, the chapter derives the condition on vorticity, and then it explains the numerical implementation in Murphy. Firstly validation of the no-slip condition is made with the study of the convergence of a Poiseuille flow in a channel.

6.2 Expression of the boundary conditions

The boundary conditions of the velocity are the same as for the no-through flow, except that the components u_x and u_z are enforced to be equal to 0 at the wall since no more slip is allowed. Thus, we recall that the no-thought flow conditions on velocity read as,

$$\begin{aligned} \frac{\partial u_x}{\partial y} &= 0, \\ u_y &= 0, \\ \frac{\partial u_z}{\partial y} &= 0. \end{aligned} \tag{6.1}$$

Taking into account the no-slip condition, we impose at the wall,

$$\begin{aligned} u_x &= 0, \\ u_z &= 0. \end{aligned} \tag{6.2}$$

Moreover, imposing a velocity of 0 on the whole boundary leads to nullifying the spatial derivatives of the field in the $\hat{e}_x$ and $\hat{e}_z$ directions,

$$\left.\frac{\partial u_x}{\partial x}\right|_0 = \left.\frac{\partial u_y}{\partial x}\right|_0 = \left.\frac{\partial u_z}{\partial x}\right|_0 = \left.\frac{\partial u_x}{\partial z}\right|_z = \left.\frac{\partial u_y}{\partial z}\right|_0 = \left.\frac{\partial u_z}{\partial z}\right|_0 = 0. \tag{6.3}$$

The vorticity must be computed to be consistent with the no-slip velocity. We recall that the vorticity is defined from the velocity as $\boldsymbol{\omega} = \nabla \times \mathbf{u}$,

$$\begin{aligned} \omega_x &= \frac{\partial u_z}{\partial y} - \frac{\partial u_y}{\partial z}, \\ \omega_y &= \frac{\partial u_x}{\partial z} - \frac{\partial u_z}{\partial x}, \\ \omega_z &= \frac{\partial u_y}{\partial x} - \frac{\partial u_x}{\partial y}. \end{aligned} \tag{6.4}$$

However, the conditions imposed on the velocity field allow to simplify this expression in order to only have two derivatives to evaluate.

$$\begin{aligned} \omega_x &= \frac{\partial u_z}{\partial y}, \\ \omega_y &= 0, \\ \omega_z &= -\frac{\partial u_x}{\partial y}. \end{aligned} \tag{6.5}$$

These spatial derivatives of the velocity are computed by using a decentered finite difference of the fourth order,

$$\left.\frac{du}{dy}\right|_0 = \frac{-25U_0 + 48U_1 + 36U_2 + 16U_3 - 3U_4}{12h} - \frac{h^4}{5}\frac{d^5u}{dy^5}, \tag{6.6}$$

where these points correspond on a grid to,

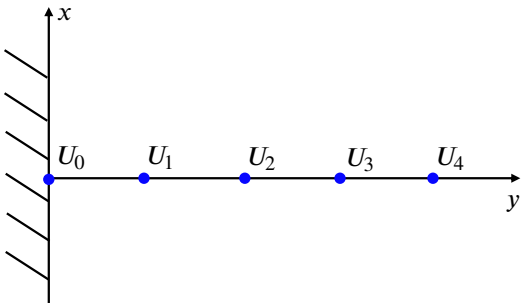

Figure 6.1: Decentered finite difference scheme.

The expression of the vorticity is retrieved by replacing the derivatives in equation 6.5 by their approximation evaluated with the decentered finite difference. Since the no-slip condition imposed that $U_0 = 0$, it is not even necessary to take this point into account in the computation. Thus, the vorticity required at the wall to enforce the no-slip boundary condition reads as,

$$\begin{aligned}
\omega_x(x,0,z) &= \frac{48u_z(x,\Delta y,z) - 36u_z(x,2\Delta y,z) + 16u_z(x,3\Delta y,z) - 3u_z(x,4\Delta y,z)}{12\Delta y},\\
\omega_y(x,0,z) &= 0,\\
\omega_z(x,0,z) &= -\frac{48u_x(x,\Delta y,z) - 36u_x(x,2\Delta y,z) + 16u_x(x,3\Delta y,z) - 3u_x(x,4\Delta y,z)}{12\Delta y}.
\end{aligned} \tag{6.7}$$

6.3 Implementation in Murphy

Firstly, the Poisson equation is solved with a no-through flow boundary condition imposed on both velocity and vorticity fields, as described in the previous chapter. In this case, the normal vorticity ω_y is set to zero since diffusion is not allowed anymore through the wall.

Once resolved, the fields must be adapted to meet the no-slip boundary condition. At first, the velocity field returned from the Poisson solver still has a slip velocity at the wall. Thus, the slip velocity u_x and u_z are overwritten and set to zero to enforce the no-slip condition. Then, the vortex sheet strength is computed by using equation 6.7, and the vorticity at the wall is overwritten by these values. Therefore, both velocity and vorticity fields are consistent with the no-slip and no-through flow conditions.

Once those fields have the right boundary conditions, the right-hand side of the Navier-Stokes equation can be evaluated. We recall that the vorticity-velocity formulation of momentum conservation implemented in Murphy is the following,

$$\frac{\partial \boldsymbol{\omega}}{\partial t} = \nu \nabla^2 \boldsymbol{\omega} + \nabla \times ((\nabla \times \mathbf{u}) \times \mathbf{u}). \tag{6.8}$$

This right-hand side (RHS) of the equation 6.8 is computed as usual, i.e., with a fourth order cross stencil. Indeed, the RHS at the wall is set to zero, but the vorticity at $y = -\Delta y$ is no longer consistent with the newly imposed vorticity at the wall, and this point is required depending on the order of the operators. Hence, a fourth order ghost point is computed to impose this point as follows,

$$\omega(x,-\Delta y,z) = 4\omega(x,0,z) - 6\omega(x,\Delta y,z) + 4\omega(x,2\Delta y,z) - \omega(x,3\Delta y,z). \tag{6.9}$$

Lepot [29] states that similar results can be achieved by using decentered finite differences of second order at the wall.

6.4 Validation : Channel flow

6.4.1 Poiseuille flow

Now that the no-slip boundary condition is implemented in the code, we run a simple test case to validate it. Because we are interested in a channel flow, Poiseuille flow is investigated, and its analytical solution is compared. Indeed, the next chapter will investigate the case of turbulent channel flow, and we must be able to impose a constant flow rate.

Analitical solution

The flow inside a channel is characterized by a constant flow rate, which is defined (per depth unit) as,

$$Q = \int_0^{2\delta} u(y)dy = 2\delta U_\infty. \tag{6.10}$$

We consider that the channel is infinitely long in both streamwise ($\hat{e}_x$) and spanwise directions ($\hat{e}_z$). Thus, the flow is fully developed in these directions, which induces that the velocity is constant in $\hat{e}_x$ and $\hat{e}_z$. Moreover, the height of the channel is thin, which allows us to consider that the component of velocity in $\hat{e}_y$ is zero. The last assumption is that the flow reaches its steady state and does not vary in time. Hence, the velocity field can be described as only one component in the streamwise direction and varying only with respect to y,

$$u = u_x(y)\hat{e}_x. \tag{6.11}$$

For this simplified velocity field, the Navier-Stokes equation of momentum for one-dimensional flow reads as,

$$0 = -\frac{1}{\rho}\frac{dp}{dx} + \nu\frac{\partial^2 u}{\partial y^2}. \tag{6.12}$$

This equation can therefore quickly be analytically solved by imposing the conditions associated with the problem. Indeed, the velocity is zero at the wall from the no-slip boundary condition, and the flow rate is forced to Q. The solution, with dimensionless quantities, reads,

$$u'(y') = -6(y'^2 - y'), \tag{6.13}$$

$$\omega'_z = \frac{du'}{dy'} = 6(2y' - 1), \tag{6.14}$$

where $u' = u/U_\infty$, $y' = y/L_y$ and $\omega' = \omega \cdot L_y/U_\infty$.

6.4.2 Initial condition and numerical setup

At the start of the simulation, a uniform velocity profile is imposed at U_∞, and we expect the flow to converge towards the parabolic profile of the Poiseuille flow while keeping a constant flow rate. The latter is set in the code as follows. Firstly, the Poisson equation is solved from the vorticity field to get the velocity field $\mathbf{u}_{solved}$, then the free stream velocity $\mathbf{u}_\infty$ is added to this field. Hence, the final velocity field is the following,

$$\mathbf{u} = \mathbf{u}_{solved} + \mathbf{u}_\infty, \tag{6.15}$$

where $\mathbf{u}_\infty = (U_\infty, 0, 0)$. Hence, the flow is considered as unidirectional in $\hat{e}_x$, and the flow rate Q is oriented in this direction. The boundary conditions in $\hat{e}_x$ and $\hat{e}_z$ are periodic, while those in $\hat{e}_y$ are the no-slip and no-through flow boundary conditions, as represented in Figure 6.2.

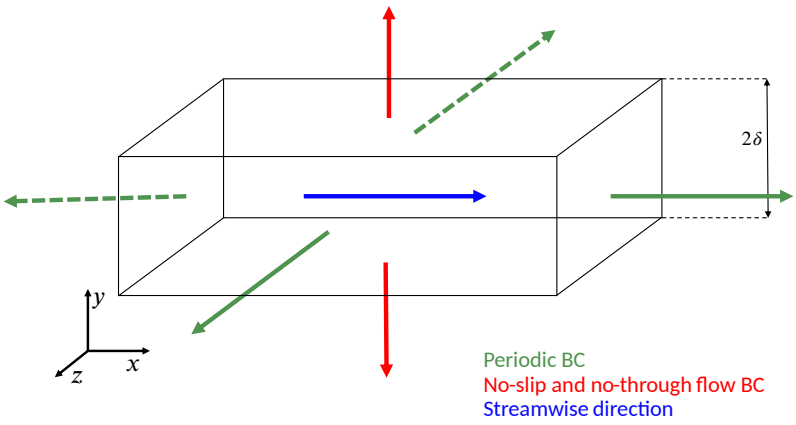

Figure 6.2: Boundary conditions setup for channel flow.

The Reynolds number based on half the height of the channel is $Re_\delta = \delta U_\infty/\nu = 100$, and the characteristic time is defined as $t_c = \delta/U_\infty$. The numerical setup of the simulation is given in Table 6.1.

$Re_\delta = \delta U_\infty/\nu$	N_x	N_y	N_z	L_x/δ	L_y/δ	L_z/δ	t_c [s]
100	48	48	48	1.0	1.0	1.0	0.5

Table 6.1: Numerical parameters for the simulation of the Poiseuille flow.

6.4.3 Results and discussion

Figure 6.3 shows the convergence of the flow into a Poiseuille flow. The flow starts with a constant velocity profile, except at the wall, where it is set to 0. Therefore, the vorticity field is zero except at the wall, with a sharp transition due to the computation of the no-slip boundary condition. The flow converges with respect to time toward the analytical solution while conserving the constant flow rate at Q.

Indeed, the curve for $\tau = 20$ is barely visible since it overlaps with the analytical solution.

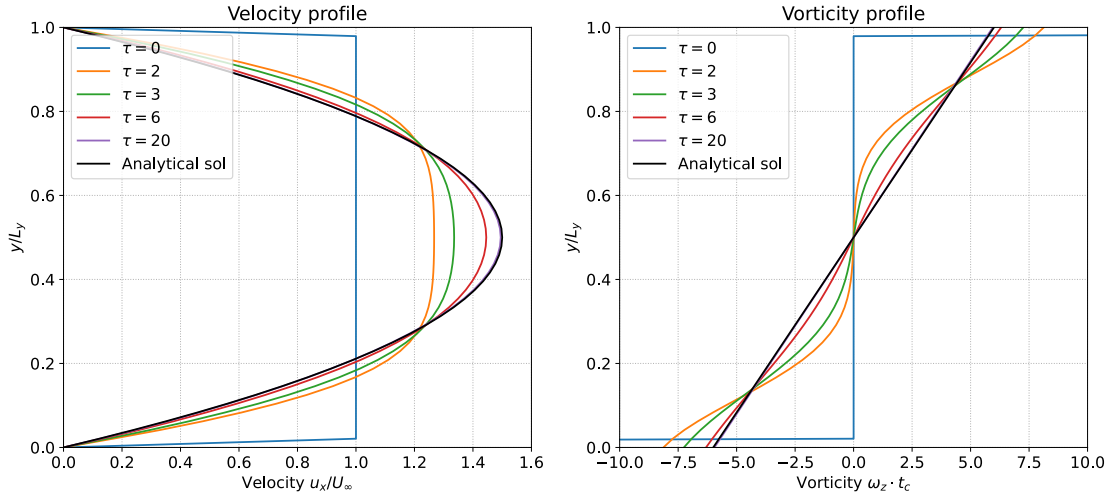

Figure 6.3: Convergence of the velocity and vorticity profile into Poiseuille flow.

After $\tau = 20$, the relative error L^2 is computed between the analytical solution u_e and the numerical solution u_n as,

$$E_{L^2} = \frac{\int_0^{L_y} (u_e - u_n)^2 dy}{\int_0^{L_y} u_e^2 dy} = 9.95 \times 10^{-6}. \tag{6.16}$$

Hence, the relative error is small enough to conclude that the flow converges correctly to the analytical solution.

6.5 Conclusion

Therefore, the no-slip boundary condition is implemented in Murphy by using the no-thought flow boundary condition and imposing the right value of velocity and vorticity at the wall. The boundary condition is validated by simulating the case of a steady-state flow in a channel with a constant flow rate. Indeed, the numerical solution converges into the analytical solution of Poiseuille flow after a long time.

Chapter 7

DNS of Turbulent channel flow at $Re_\tau = 180$

7.1 Introduction

Turbulent channel flow simulations require a very fine grid to be able to capture all scales of turbulence generated by solid boundary, especially at high Reynolds numbers. However, the finer the grid, the more computational resources are required for the simulation. Indeed, this is one of the motivations for using models such as wall-modeled LES. Before considering the latter model, which is presented in the next chapter, we investigate a DNS of channel flow at a low Reynolds number in order to confirm the validation of the no-slip boundary condition. Thus, the Reynolds number based on half of the channel is $Re_\delta = 2800$, and the one from the mean friction velocity is $Re_\tau = 180$. Results are compared with the DNS results of Lee and Moser [28].

7.1.1 Characterization of turbulent channel flows

The test case of turbulent channel flow is similar in principle to the channel flow described above, except that it is now governed by turbulence. Thus, each quantity can be decomposed into an average component, which is independent of time since the flow is statistically stationary, and a fluctuation component as follows,

$$\begin{aligned} u(t) &= \bar{u} + u'(t), \\ v(t) &= \bar{v} + v'(t), \\ w(t) &= \bar{w} + w'(t). \end{aligned} \tag{7.1}$$

The average component is defined as the time average over a period T, greater than the characteristic time corresponding to the slowest turbulent fluctuations. For the case of a turbulent channel flow, the only non-zero average component is $\bar{u}$ and varies with the height. The streamwise and spanwise velocities are only composed of fluctuation terms as their average component is zero,

$$\begin{aligned}\bar{u} &= \frac{1}{T}\int_{t_0}^{t+T} u(t',y)dt',\\ \bar{v} &= \frac{1}{T}\int_{t_0}^{t+T} v(t',y)dt' = 0,\\ \bar{w} &= \frac{1}{T}\int_{t_0}^{t+T} w(t',y)dt' = 0.\end{aligned} \tag{7.2}$$

The shear stress at the wall is defined as,

$$\tau_w = \mu \left.\frac{\partial \bar{u}}{\partial y}\right|_{y=0}. \tag{7.3}$$

From the shear stress at the wall, a velocity scale is defined as the friction velocity u_τ and reads,

$$u_\tau = \sqrt{\frac{\tau_w}{\rho}}. \tag{7.4}$$

Two characteristic Reynolds numbers are defined in the case of a turbulent channel flow, the bulk Reynolds number Re_δ and the friction Reynolds number Re_τ.

$$Re_\delta = \frac{U_\infty \delta}{\nu}, \quad Re_\tau = \frac{u_\tau \delta}{\nu}. \tag{7.5}$$

The flow rate is forced by Re_δ, but the simulation aims to retrieve the corresponding u_τ, and therefore, the associated Re_τ. From the mean friction velocity, the dimensionless variables can be computed as,

$$y^+ = \frac{y u_\tau}{\nu}, \quad \bar{u}^+ = \frac{\bar{u}}{u_\tau}. \tag{7.6}$$

7.2 Initial perturbation of Poiseuille flow and numerical setup

As proposed by Lepot [29], the flow starts with a very perturbed Poiseuille flow in order to initiate turbulence at this low Reynolds number. Thus, the initial vorticity field is the analytical solution from the Poiseuille flow, modulated in the streamwise and wall-normal direction, and the field reads,

$$\begin{aligned}\omega_x &= 0,\\ \omega_y &= 0,\\ \omega_z &= -\frac{3U_\infty}{\delta^2}(\delta - y)\cdot A\left(k_1 \cos\left(k_1 y\right) + k_2 \cos\left(k_2 y\right)\right)\sin(k_3 x),\end{aligned} \tag{7.7}$$

where $A = 1/(0.65\pi)$m and wavenumbers k_1, k_2 and k_3 of perturbation are respectively π/L_y, $24\pi/L_y$ and $8\pi/L_z$. These constants have been chosen in order to have the same conditions as Lepot [29]. Thus, the initial vorticity field is presented in Figure 7.1, and the velocity computed from the perturbed vorticity field is shown in Figure 7.2.

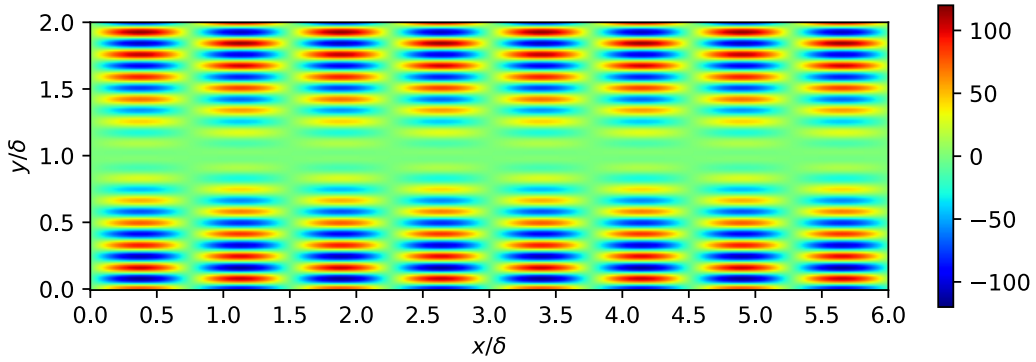

Figure 7.1: Slice of initial condition of vorticity ω_z in the plane $z = L_z/2$.

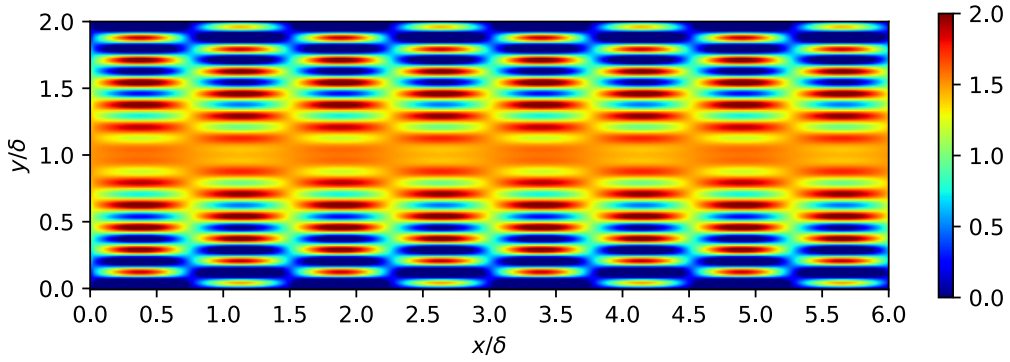

Figure 7.2: Slice of initial velocity u_x in the plane $z = L_z/2$.

The characteristic time is defined as $t_c = \delta/u_\tau$. The simulation parameters are given in Table 7.1 and the boundary conditions are the same as shown in Figure 6.2. Unlike the simulation of Lee and Moser [28], composed of a stretched mesh, Murphy uses a uniform grid which requires more points to correctly capture the flow close to the wall. For this reason, the channel is shorter in the streamwise and spanwise directions than the reference channel.

$Re_\delta = \delta U_\infty/\nu$	$Re_\tau = \delta u_\tau/\nu$	N_x	N_y	N_z	L_x/δ	L_y/δ	L_z/δ	t_c [s]
2800	180	768	256	512	6.0	2.0	4.0	7.78

Table 7.1: Numerical parameters for the simulation of the DNS of turbulent channel flow at $Re_\tau = 180$.

The DNS is made on 320 CPUs and during 6.3 days or 151 hours of physical time to achieve the wanted simulation time of $\tau = 25$.

In fact, as this simulation time is substantial, an under-resolved DNS was firstly performed to get an initial view of the behavior of a turbulent channel flow. Hence, the domain is twice as coarse in the three dimensions, and the results are presented in appendix A. The results of DNS described in Table 7.1 are given below.

The turbulent regime takes some time to settle in the channel flow. Indeed, from Figure 7.3, we observe that from the perturbed initial condition, the flow tends to smooth these perturbations at the beginning, i.e., for $\tau < 5.0$. Nevertheless, some instabilities are still present and moving in the domain. Hence, the flow becomes turbulent after a certain time, here $\tau = 7.5$. In order to be sure that the channel is fully developed at the right Re_τ, it is necessary to wait some more time, which is chosen at $\tau = 12.5$. After this time, the statistics are computed on an additional $\tau = 12.5$ to get the N_t samples. Taking into account that the three-dimensional flow is periodic in two directions, the quantities investigated are also averaged spatially in the streamwise and spanwise directions. Hence, the statistics are performed on $N_x \times N_z \times N_t$ samples.

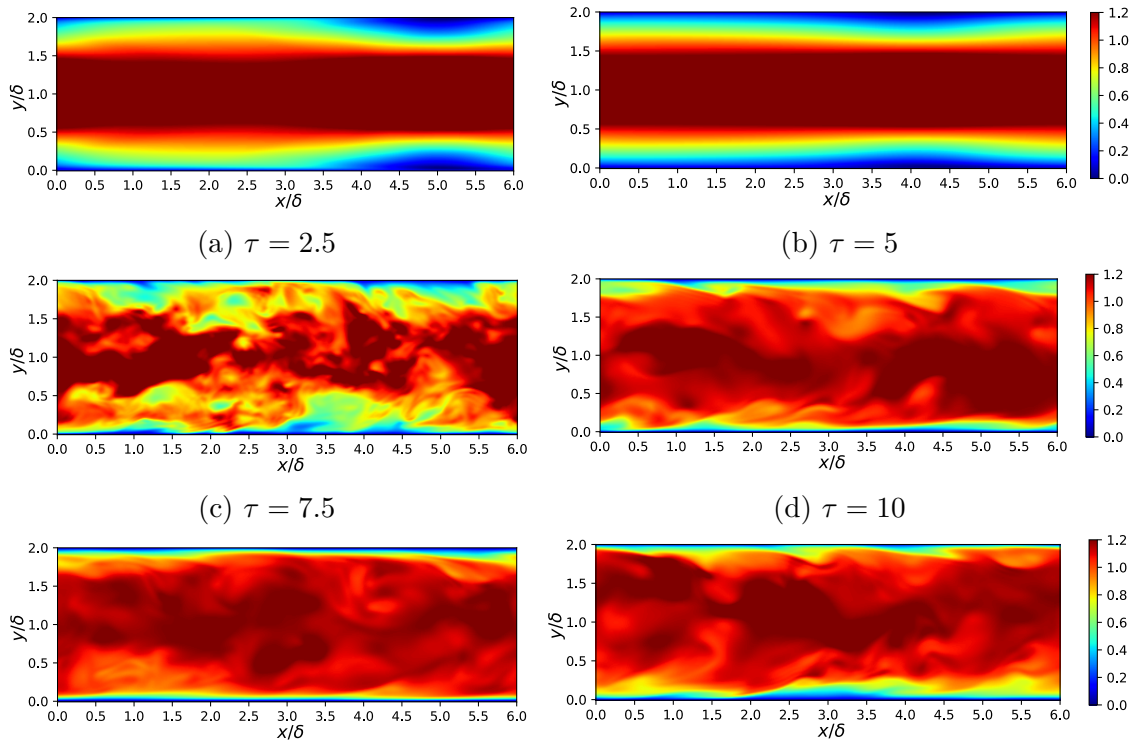

(a) $\tau = 2.5$ (b) $\tau = 5$

(c) $\tau = 7.5$ (d) $\tau = 10$

(e) $\tau = 12.5$ (f) $\tau = 20$

Figure 7.3: Transition of the instantaneous velocity field into fully a turbulent flow. Slices of velocity u_x/U_∞ for different times.

7.3 Results and discussion

Figure 7.4 shows the average velocity profile obtained and the comparison with the DNS of Lee and Moser [28]. Thus, the characteristic shape of the turbulent channel flow is well retrieved, and our simulation overlaps with the reference. There is still a slight underestimation of the velocity in bulk, which can be better observed in Figure 7.5. The latter shows the dimensionless turbulent quantities y^+ and u^+ profile in logarithmic scale. The friction velocity computed from the velocity profile is slightly overestimated, we find $u_\tau = 0.06428$ [m/s] instead of $u_\tau = 0.0637$ [m/s] from Lee and Moser [28]. Hence, the friction Reynolds number can be computed and is $Re_\tau = 179.984$ which is close to the targeted Reynolds number, and where Lee and Moser [28] results give $Re_\tau = 182.088$.

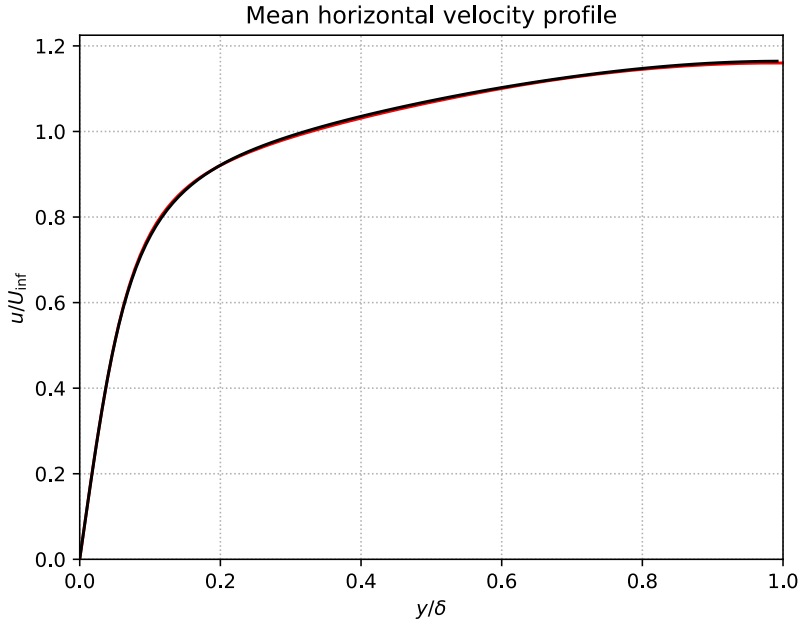

Figure 7.4: Channel flow at $Re_\tau = 180$. Mean velocity profile: DNS of Lee and Moser [28] (—) and DNS from Murphy (—).

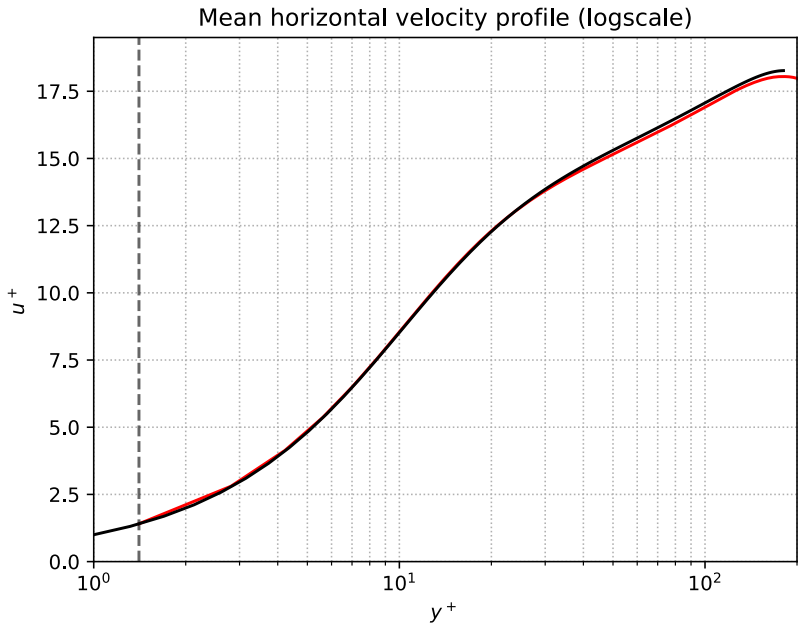

Figure 7.5: Channel flow at $Re_\tau = 180$. Mean velocity profile in logscale: DNS of Lee and Moser [28] (—) and DNS from Murphy (—). The dashed line corresponds to y_1^+ from our mesh.

The variance and covariance are defined as follow,

$$\begin{aligned}
\langle u'u' \rangle &= \frac{1}{T} \int_t^{t+T} (u(t') - \bar{u})^2 dt' \\
&= \frac{1}{T} \int_t^{t+T} (u'(t'))^2 dt', \\
\langle u'v' \rangle &= \frac{1}{T} \int_t^{t+T} (u(t') - \bar{u})(v(t') - \bar{v}) dt' \\
&= \frac{1}{T} \int_t^{t+T} (u'(t'))(v'(t')) dt'.
\end{aligned} \tag{7.8}$$

The average standard deviation, also named RMS, is computed from the square root of these variances, and turbulent kinetic energy can be computed from the variances as,

$$k = \frac{1}{2}(\langle u'u' \rangle + \langle v'v' \rangle + \langle w'w' \rangle). \tag{7.9}$$

The RMS fluctuation profiles are shown in Figure 7.6 and the turbulent kinetic energy profile in Figure 7.7. Hence, the three RMS quantities globally retrieve the same behavior as the reference. However, fluctuations in the streamwise direction have a slightly overestimated peak, with some variation in the bulk. The fluctuations in the spanwise are underestimated, while those for transverse velocity fit well with the reference. The turbulent kinetic energy profile undergoes a higher peak, followed

by a slight underestimation, mainly due to deviation of RMS fluctuations of the spanwise velocity.

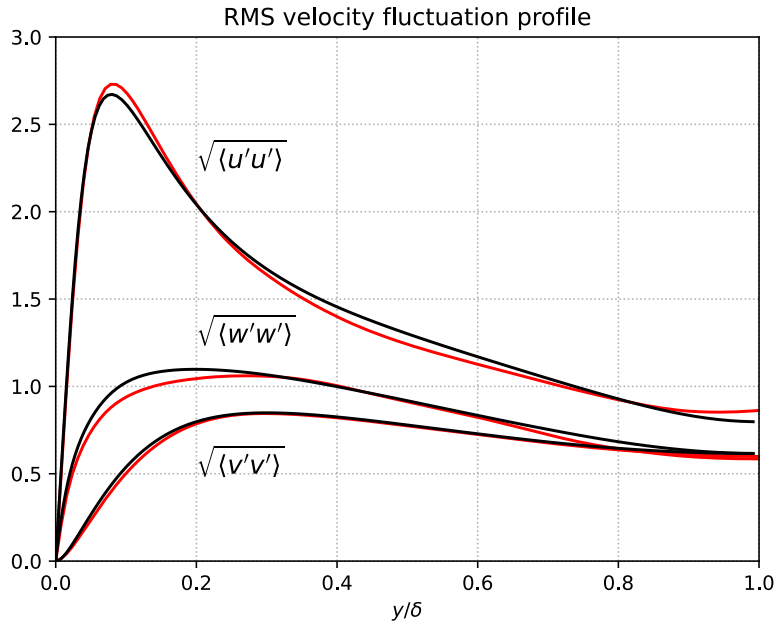

Figure 7.6: Channel flow at $Re_\tau = 180$. RMS velocity fluctuation profiles: DNS of Lee and Moser [28] (—) and DNS from Murphy (—).

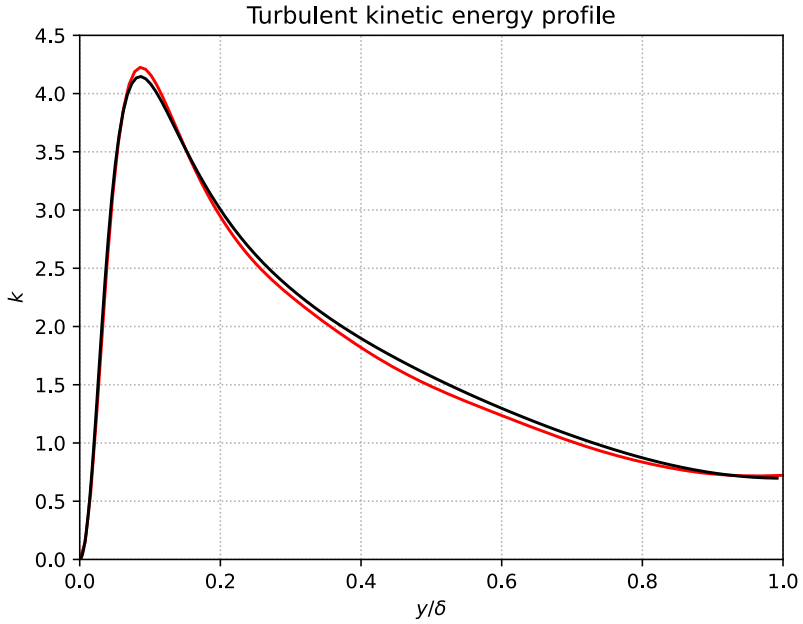

Figure 7.7: Channel flow at $Re_\tau = 180$. Turbulent kinetic energy profile: DNS of Lee and Moser [28] (—) and DNS from Murphy (—).

The last quantity of interest is the shear stress. The latter comprises molecular stress τ_m, dominant near the wall, and turbulent shear stress τ_t. These are defined mathematically as,

$$\tau_m = -\frac{\langle u'v' \rangle}{u_\tau^2}, \qquad \tau_t = \nu \frac{d\bar{u}/dy}{u_\tau^2}. \tag{7.10}$$

These two shear stress compose the total shear stress, and their sum should give a strain line. Figure 7.8 shows that both molecular and turbulent shear stress converge toward the reference but with a very slight underestimation. The linear behavior is globally preserved, with a slightly lower slope than expected due to the deviations described above.

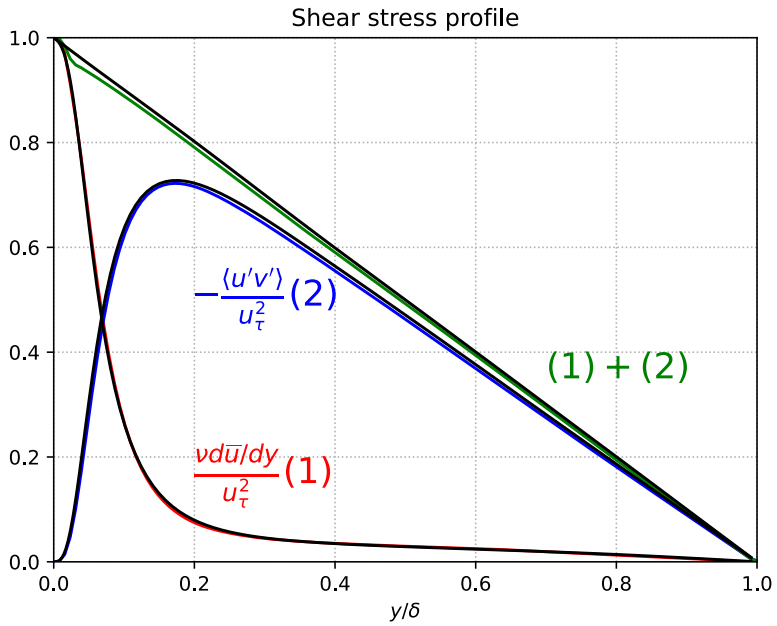

Figure 7.8: Channel flow at $Re_\tau = 180$. Mean shear stress profiles: DNS of Lee and Moser [28] (—) and DNS from Murphy (—), (—), (—).

7.4 Conclusion

The DNS of a turbulent channel flow at a low Reynolds of $Re_\tau = 180$ ($Re_\delta = 2800$) is performed in Murphy, thank to the implementation of the no-slip condition, and the quantities of interest are compared with results from Lee and Moser [28]. Thus, the simulation done with Murphy gives a really good agreement with the reference, indeed, the velocity profiles overlap and the estimated friction velocity is close, $u_\tau = 0.06428$[m/s] instead of $u_\tau = 0.0637$ [m/s]. Other quantities, such as RMS fluctuations or shear stress profiles, may differ slightly but are still close to the reference. However, achieving these results requires high computational resources, even at low Reynolds numbers. Hence, the next chapter investigates wall-modeled LES to relax the DNS mesh size constraint for channel flow.

Chapter 8

Wall shear stress model for wall modeled LES (wmLES)

8.1 Introduction

In Chapter 3, the necessary resources for DNS are budgeted with respect to the Reynolds number. The latter corresponds to the case of a HIT flow, but the complexity increases even more when the flow interacts with a solid boundary. Choi and Moin [7] shows that in a three-dimensional wall-bounded flow, the number of grid points required to be able to capture all the turbulent scales is proportional to $Re^{37/14}$. Taking into account the temporal complexity, the total cost of the simulation scales as,

$$N_x N_y N_z N_t \propto Re^{3.5}, \tag{8.1}$$

which makes turbulent channel flow DNS even costlier. Indeed, our simulation of the turbulent channel flow at a low Reynolds number $Re_\tau = 180$, performed in the previous chapter, required considerable resources, both in CPUs and in physical time and is far from industrial applications. Although the DNS of Lee and Moser [28] for channel flow at $Re_\tau = 5200$ come close to industrial applications, they are too resource-intensive to be applicable. Better improvement could be expected from Wall-resolved LES, but the latter's mesh scales as $Re^{1.9}$ [7], which also requires unaffordable computational resources for high Reynolds number applications. Indeed, the inner part of the boundary layer requires high resolution to resolve structures up to the viscous layer. In order to overcome this issue, wall-modeled LES (wmLES) is proposed, firstly employed by Deardorff [10] and Schumann [45], and yields to a reduction of the mesh requirement to $N \propto Re^{1.0}$ [7].

Thus, wmLES is composed of two models. The first one is a classical LES, which acts on the entire domain while a specific model is used for the inner layer to overcome the issues observed in the case of Wall-resolved LES. Hence, the no-slip boundary condition is relaxed and the wall shear stress is imposed from information taken above the wall. Thiry [48] provides a complete analysis of wall shear stress model, as it is investigated in this present work. Nevertheless, the latter uses a code with

the Navier-Stokes equations expressed in velocity-pressure, which has the advantage of being able to impose friction on the wall directly. In the present case, we cannot directly impose a certain friction on the wall, but we will pass by imposing the vorticity on the boundary.

8.2 Algebraic wall model in Murphy

An algebraic wall shear stress model is investigated here. The objective of the latter is to impose the shear at the wall by taking into account information from an algebraic formulation. Thus, we consider that a given law of the wall (LOTW): $u^+ = f(y^+)$ is valid on average and can be used to retrieve relevant quantities of the flow. There are several algebraic functions to approximate the velocity profile, but we use the standard log law, which reads,

$$\frac{u}{u_\tau} = \frac{1}{\kappa} \log\left(\frac{y u_\tau}{\nu}\right) + C, \tag{8.2}$$

where the constants are $\kappa = 0.41$ and $C = 5$. Figure 8.1 shows the dimensionless velocity profile from the DNS and the chosen LOTW. Indeed, the latter is only valid for the logarithmic region of the profile, which starts at $y^+ \simeq 70 - 90$.

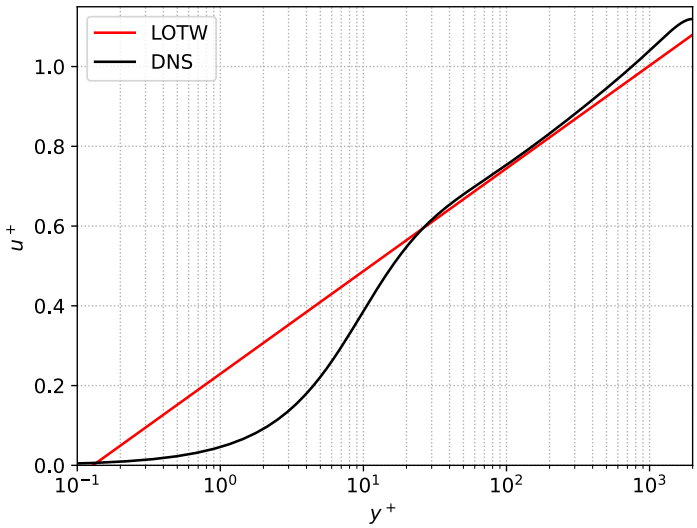

Figure 8.1: Law of the wall for channel flow at $Re_\tau = 2000$, comparison with DNS of Lee and Moser [28].

Conventional codes that use the velocity-pressure formulation of Navier-Stokes benefit from having boundary conditions expressed as fluxes, and the shear stress can directly be imposed on viscous flux, without needing to impose a condition on the velocity. However, in a velocity-vorticity code such as Murphy, since we have no direct access to a conditions on the shear stress, it is required to be clever and to impose a valid vorticity from the known friction and shear stress at the wall. For the

velocity, we want to impose partial-slip conditions since the latter should not be set to zero.

8.2.1 Imposing the vorticity

At the wall, the vorticity can be simplified as $\omega = \partial u/\partial y$. Hence, the key to determining the vorticity is to find a reliable estimation of the spatial derivative of the velocity. However, the grid is too coarse near the wall to be able to estimate the derivative correctly and directly with, for example, a finite difference. The model is therefore based on the theoretical velocity profile in order to obtain additional information on the flow in the log layer.

The first idea was to use the "turbulent friction length", also called "slip length" $l(y)$, where we consider that the velocity in the region close to the wall follows,

$$u(y) = l(y)\frac{\partial u}{\partial y}. \tag{8.3}$$

Based on this relation, the vorticity at the wall can be set as,

$$\omega_{//} = \frac{u(y)}{l(y)}, \tag{8.4}$$

where $\omega_{//}$ are the components of vorticity that are tangent to the wall. The normal component of the vorticity is set at zero. By considering that this equation 8.3 is valid in the log layer, the slip length can be computed by replacing $u(y)$ and its derivative by those of the chosen LOTW, so the slip length reads,

$$l(y) = \kappa y \left(\frac{1}{\kappa}\log\left(\frac{y u_\tau}{\nu}\right) + C\right). \tag{8.5}$$

It can be rewritten using dimensionless quantities, with $l^+(y^+) = u_\tau l(y^+)/\nu$ and reads,

$$l^+(y^+) = y^+\left(\log\left(y^+\right) + \kappa C\right). \tag{8.6}$$

After a few unsuccessful attempts, this model based on slip length is discarded. Indeed, the velocity profile obtained with this method is essentially a constant plateau with a steep drop at the wall. It seems that the momentum transfer between the wall and the bulk does not work properly. In fact, there is no turbulent entrainment, or at least very little, to maintain a velocity deficit near the wall.

Since the previous model shows very poor performance, another model is investigated. This model is based on the shear stress profile, which reads,

$$(\nu + \nu_t)\frac{\partial u}{\partial y} = u_\tau^2\left(1 - \frac{y}{\delta}\right). \tag{8.7}$$

In the inner layer, the ratio y/δ is small over 1, and the expression can be simplified as,

$$(\nu + \nu_t)\frac{\partial u}{\partial y} = u_\tau^2. \tag{8.8}$$

We are interested in finding the value of $\partial u/\partial y$ at the wall to impose the vorticity. The assumption is made that ν_t can be replaced by ν_{sgs}. In this case, the latter is modeled by a basic SMAG model, which is simplified at the wall as $C_s\Delta^2 \left|\partial u/\partial y\right|$ when the basis is aligned with the velocity $\mathbf{u}$. Therefore, the relationship becomes,

$$\left(\nu + C_s h^2 \left|\frac{\partial u}{\partial y}\right|\right)\frac{\partial u}{\partial y} = u_\tau^2. \tag{8.9}$$

Note that there is no given constant value C_s, even the classical value of $C_s = 0.027$ has no more sense since the flow does not fulfill the assumptions allowing to fix it. Moreover, nothing tells us that this constant used for the wall model must be equal to the one used in the SGS model acting in the flow. By default, we will use the same constant C_s for both models.

Therefore, a relation is required to know the mean shear stress velocity u_τ. Through the use of the chosen LOTW, and by measuring the averaged velocity $\langle\mathbf{u}\rangle$ at a certain height y (in the validity region of the law), u_τ can be computed from the equation:

$$|\langle\mathbf{u}\rangle| - u_\tau f\left(\frac{y u_\tau}{\nu}\right) = 0. \tag{8.10}$$

As this equation is non-linear, it is solved with a Newton-Raphson scheme, and the solution converges after a few iterations. The average strategy $\langle\cdot\rangle$ is chosen as an average over a window of 5×5, in the stream and span direction $\hat{e}_x$ and $\hat{e}_z$. Thiry [48] compares different strategies of averaging and concludes that the method has little impact on the result and a 5×5 averaging window is enough to recover the correct profile of the mean velocity as well as the velocity fluctuations, which are slightly impacted with respect to averaging strategies.

Hence, the method is the following and is represented in Figure 8.2. From a certain height above the wall, defined as h_{wm}, the average velocity $|\langle\mathbf{u}(x, h_{wm}, z)\rangle|$ is computed. Then, based on $|\langle\mathbf{u}\rangle|$ and the LOTW (equation 8.2) evaluated at $y = h_{wm}$, the equation 8.10 can be resolved in order to obtain the velocity u_τ.

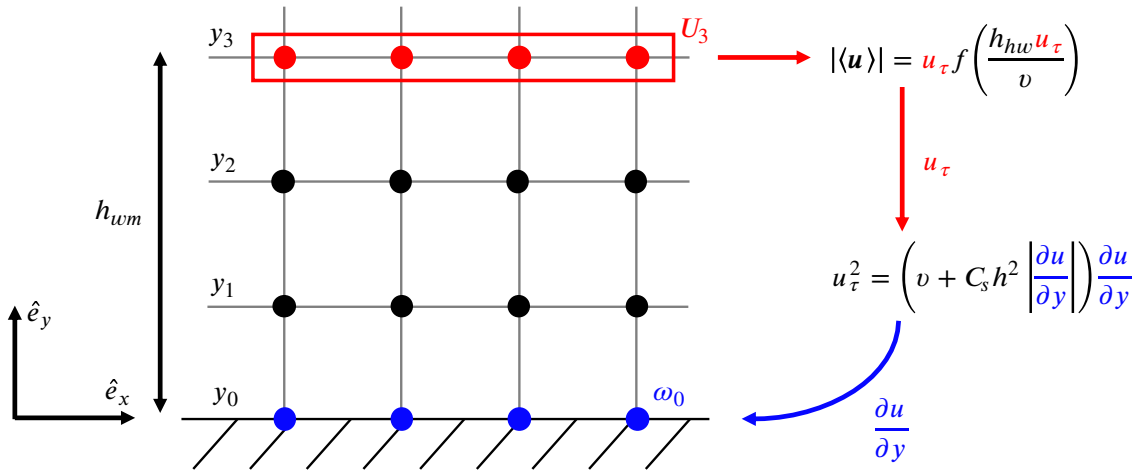

Figure 8.2: Schematic for the wall model, the velocity is taken at $y = h_{wm}$ to impose condition on vorticity at $y = 0$.

Once the mean friction velocity is estimated, the absolute value $|\partial u/\partial y|$ can be obtained by resolving the quadratic polynomial equation 8.9, where the only valid solution is the positive one. Since we compute this value in the basis aligned with the direction of the local velocity, only the magnitude is retrieved, and the associate vorticity must be oriented correctly. The approach used here is close to the one from Schumann [45], as mentioned by Thiry [48], the wall shear stress is imposed in the same direction of the local velocity at the chosen height $\mathbf{u}(x, h_{wm}, z)$, and normalized by the local average velocity computed before. Thus, the vorticity is imposed as,

$$\begin{aligned} \omega_x &= \frac{\partial u}{\partial y}\frac{u_z}{|\langle \mathbf{u} \rangle|}, \\ \omega_y &= 0, \\ \omega_z &= -\frac{\partial u}{\partial y}\frac{u_x}{|\langle \mathbf{u} \rangle|}. \end{aligned} \tag{8.11}$$

The ghost points below the wall are evaluated with the same extrapolation used for the no-slip boundary condition (equation 6.9). No other ghost points should be computed as they are not used. Finally, the RHS is set to zero at the wall.

Note that the choice of h_{wm} is critical, as discussed on UMD [49] website about wmLES. Kawai and Larsson [27], as mentioned in Frère et al. [14], propose that sampling the velocity at the third grid point, rather than the common practice of the first off-wall grid point, could remove errors in the velocity profile and strongly improve their results. Thiry [48] also observed significant improvement in its model

by sampling at the third grid point instead of the first one. Following these arguments, the choice made here is to take information from the points at $h_{wm} = y_3$. Other strategies could include taking information from $h_{wm} = y_3$ and $h_{wm} = y_2$, then taking an average of both estimations of the mean velocity friction.

8.2.2 Imposing the velocity

Since the no-slip boundary condition is relaxed, the velocity u_x and u_z no longer equal zero at the wall. Several techniques are also possible in order to obtain consistent values of slip velocity at the wall. The first idea is to set the velocity by simply computing an extrapolation from the velocity near the wall.

However, we investigate another way. We use the information of $|\partial u/\partial y|$ previously found at the wall . Indeed, based on a decentered finite difference, the velocity at the wall can be found such that its derivative with respect to y is equal to the one found from the LOTW. Hence, this condition reads,

$$\left.\frac{\partial u}{\partial y}\right|_{y=0} = \frac{-25U_0 + 48U_1 - 36U_2 + 16U_3 - 3U_4}{12h} - \frac{h^4}{5}\frac{\partial^5 u}{\partial y^5}. \tag{8.12}$$

The local spatial derivative $\partial u/\partial y|_0$ is known from the wall model, and the local velocity at the wall U_0 can be found as follows,

$$U_0 = \frac{-12\Delta \left.\frac{\partial u}{\partial y}\right|_{y=0} + 48U_1 - 36U_2 + 16U_3 - 3U_4}{25}, \tag{8.13}$$

$$\text{where } \frac{\partial u_x}{\partial y} = \frac{\partial u}{\partial y}\frac{u_x}{|\langle \mathbf{u} \rangle|} \text{ and } \frac{\partial u_z}{\partial y} = \frac{\partial u}{\partial y}\frac{u_z}{|\langle \mathbf{u} \rangle|}.$$

By locally imposing the slip velocity in this way, its spatial derivatives according to $\hat{e}_x$ and $\hat{e}_z$ are not equal to zero anymore. Therefore, the condition imposed on the vorticity ω_y in equation 8.11 is no longer consistent with the wall velocity. In order to guarantee this, the vorticity ω_y at the wall should be overwritten by the one computed according to the new slip velocity and its derivatives as,

$$\omega_y = \frac{\partial u_x}{\partial z} - \frac{\partial u_z}{\partial x}. \tag{8.14}$$

However, due to limitations in the code, this last condition is not implemented.

8.3 Test case : turbulent channel flow at $Re_\tau = 2000$

8.3.1 Initial condition and numerical setup

In the previous case of turbulent channel flow in DNS, the initial condition was set as a perturbed Poiseuille flow which needed to undergo a transitional phase to

reach a fully turbulent flow. Instead of having to wait for the field to settle to a turbulent state and to avoid to retrieve a laminar flow, the vorticity field from the slightly under-resolved DNS (appendix A) for a time $\tau > 12.5$ can be reused as an initial condition. The only difference is that the case of the latter was characterized by a $Re_\tau = 180$ whereas, for the wall model test case with a coarser grid, the flow is set with $Re_\tau = 2000$.

The initial condition used for the channel flow is the vorticity field sub-sampled by a factor of 4 in order to go from a $384 \times 128 \times 256$ to a $96 \times 32 \times 64$ grid. It is important to note that before performing the sub-sampling, the field must first be filtered to respect Shannon's theorem.

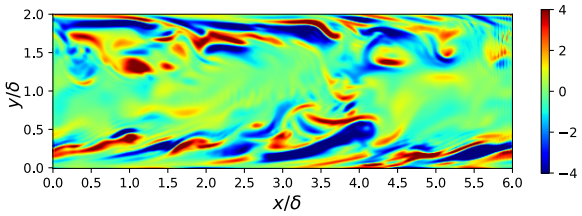

(a) From slightly under-resolved DNS at $\tau = 20.625$.

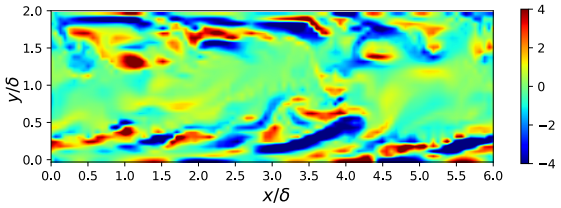

(b) Sub-sampled.

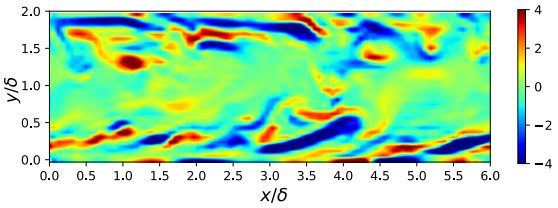

(c) Filtered and sub-sampled.

Figure 8.3: Slice of instantaneous vorticity ω_z used as initial condition for wmLES turbulent channel flow.

Indeed, one may observe in Figure 8.3 some artifacts in the sub-sampled field without an anti-aliasing filter that may corrupt the flow. In practice, once the code runs, the difference between both initial conditions is low since the flow generates turbulence in all cases. For the sake of good practice, we use the one with an anti-aliasing filter. From this initial condition, the code runs during $\tau = 18$ to let the new regime time to settle, and then the statistics are performed on an additional time of $\tau = 36$. Apart from this initial condition, the numerical setup is the same as from channel flow, but with a different Re_δ and grid size, and it is resumed in Table 8.1.

$Re_\delta = \delta U_\infty / \nu$	$Re_\tau = \delta u_\tau / \nu$	N_x	N_y	N_z	L_x/δ	L_y/δ	L_z/δ	t_c [s]
43478.26	2000	96	32	64	6.0	2.0	4.0	10.9

Table 8.1: Numerical parameters for wmLES of turbulent channel flow.

Since the grid size is greatly reduced, the computational resources are also lightened. Indeed, the domain is cut into 48 sub-blocks of 16^3 dof to let the code run on 48 CPUs, during a physical time from 5 to 12 hours, depending on the model.

8.3.2 Results and discussion

Evaluate the mean friction velocity

Since the grid is too coarse to estimate the friction velocity from a derivative of the velocity at the wall, u_τ is retrieved from our model by re-using expression 8.9 and by using the average spatial derivative $\partial u/\partial y$ at the wall, which is directly obtained from the average vorticity at the wall.

However, with this method, we get the friction velocity seen by the model, but it could be different from the one perceived by the flow of the bulk region. Indeed, we know that the shear stress over the channel follows the relationship,

$$\nu \frac{du}{dy} + \langle \tau_{xy}^{sgs} \rangle - \langle u'v' \rangle = u_\tau^2 \left(1 - \frac{y}{\delta}\right). \tag{8.15}$$

From statistic analysis, the contribution of molecular and turbulent shear stress can be retrieved. However, the contribution of the term τ_{sgs} is not measured and is significant for a low value of y/δ. Nevertheless, for y/δ near 1, its contribution is, in this case, negligible. Thus, in this region, we expect that the addition of known terms $\nu du/dy$ and $-\langle u'v' \rangle$ follows a linear relation with respect to y/δ. Actually, this relation should be approximately equal to $u_\tau^2(1 - y/\delta)$, and its value at $y = 0$ should give the expression of u_τ, which is more representative of the frictional velocity experienced by the center flow. It is therefore expected that the estimation of u_τ from the model and that from the statistical study are equal.

Slip velocity : extrapolation

Before considering the model that imposes the slip velocity from the estimated $|\partial u/\partial y|_{y=0}$, equation 8.13, we try the case where the velocity at the wall is computed with a basic extrapolation. The vorticity is set at the wall as explained with equation 8.9.

The SMAG model is used here for the LES in the outer layer, but one could investigate the effect of other SGS models, even if, as shown by Thiry [48], the SMAG model demonstrates good results. As a reminder, the constant C_s is unknown. Indeed, Meyers, Sagaut, and Geurts [37], as cited in John and Roland [26], state that a suitable value of C_s is dependent on the actual type of the mesh, its refinement level, and the underlying discretization. It is hence essential to study the influence of the constant C_s on our specific case. Thus, we keep this degree of freedom in order to adjust our model. In reality, our wmLES model is composed of two constants C_s, one for the SMAG model acting on the outer layer and one for the model at the wall, which makes two degrees of freedom, but we limit ourselves to impose them equally.

Figure 8.4 shows the velocity profile with respect to C_s coefficient. The coefficient directly influences the shape of the velocity profile. An excessive value of the coefficient tends to flatten the top and even generate a deficit. In the other side, a smaller coefficient induces a narrower peak. Moreover, a too small coefficient (< 0.02) makes the simulation explode, which is not illustrated here. Hence, the right coefficient seems to be between 0.03 and 0.04, and the average flow is very sensitive since a slight change induces a significant alteration in the profile.

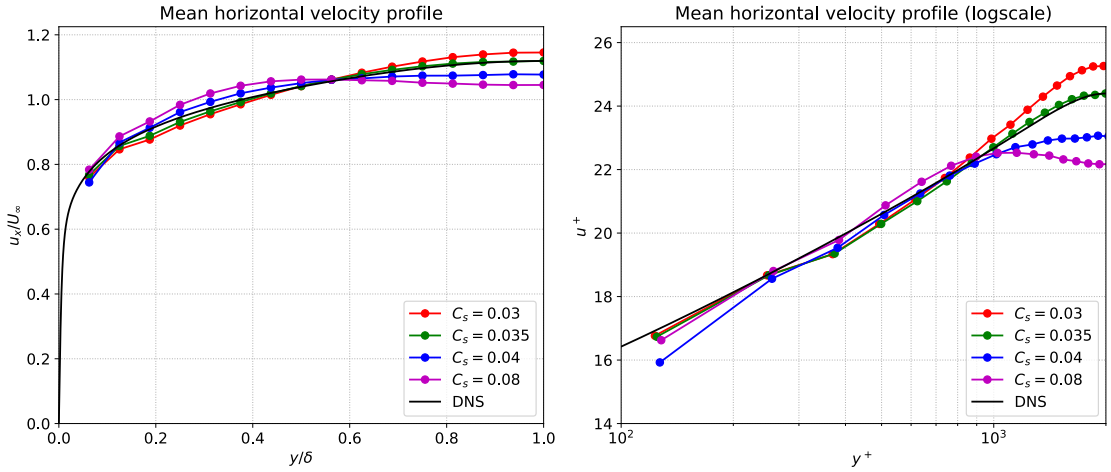

Figure 8.4: Channel flow at $Re_\tau = 2000$. Mean velocity profile (left) and in logscale (right). Comparison for different values of C_s.

As identified in Table 8.2, increasing the coefficient C_s also raises u_τ. Thus, the right value of C_s can be found such that the velocity u_τ from the model approaches the value from the reference, which is about $u_\tau = 0.045879$ m/s. Hence, the case of $C_s = 0.035$ gives the closest value of u_τ, and indeed, the corresponding simulation presents the closest profile to the reference, as shown in Figure 8.4.

C_s	0.03	0.035	0.04	0.08
u_τ [m/s]	0.04534	0.04588	0.04674	0.04714

Table 8.2: Friction velocity with respect to SMAG coefficient C_s.

Although the velocity profile seems promising, the statistics are not perfectly consistent as seen in Figure 8.5. The RMS fluctuations are globally overestimated so as the therefore kinetic energy. Furthermore, they reach a constant plateau when achieving the center of the channel instead of decreasing. Note that the RMS fluctuation profiles of components v and w are overlapping for a same value of C_s, and thus, the latter has essentially an effect on the component u of RMS fluctuation. As stated before, the estimation of velocity u_τ used to get dimensionless quantities comes from the equation used by the model, but it can be estimated from the shear stress equation 8.15. The slope of the term $-\langle u'v' \rangle$ is too high, even if it decreases slightly with C_s. There is, therefore, an inconsistency between the value of u_τ measured by the model and the one perceived by the flow and statistics.

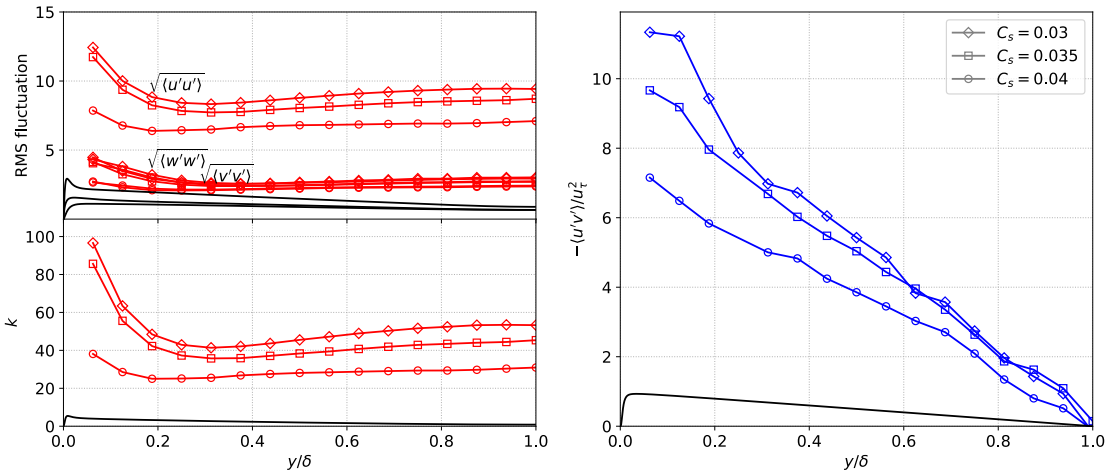

Figure 8.5: Channel flow at $Re_\tau = 2000$. RMS velocity fluctuation profile (left) and mean shear stress profiles (right). Comparison for different values of C_s, with 0.03 (diamonds), 0.035 (squares) and 0.04 (circles).

Slip velocity : decentered finite difference

We are now interested in the case where the slip velocity is imposed at the wall as given in equation 8.13, while keeping the same condition as before for the vorticity at the wall.

As done for the previous case, the parameter C_s is swept in order to observe its influence on the profile. Figure 8.6 shows that, no matter the value of C_s, the velocity u_x/U_∞ is overestimated in bulk, but the shape of the curve is very close to the reference. Moreover, the impact of C_s on the profile shape is much lighter, and the latter controls the overestimation in the bulk region. Indeed, increasing C_s leads to bringing the reference a little closer while straightening the profile near the wall. From the dimensionless profile, an opposite shift in the bulk is made when C_s grows. Indeed, the velocity profile in bulk increases with C_s due to the estimation of u_τ that decreases.

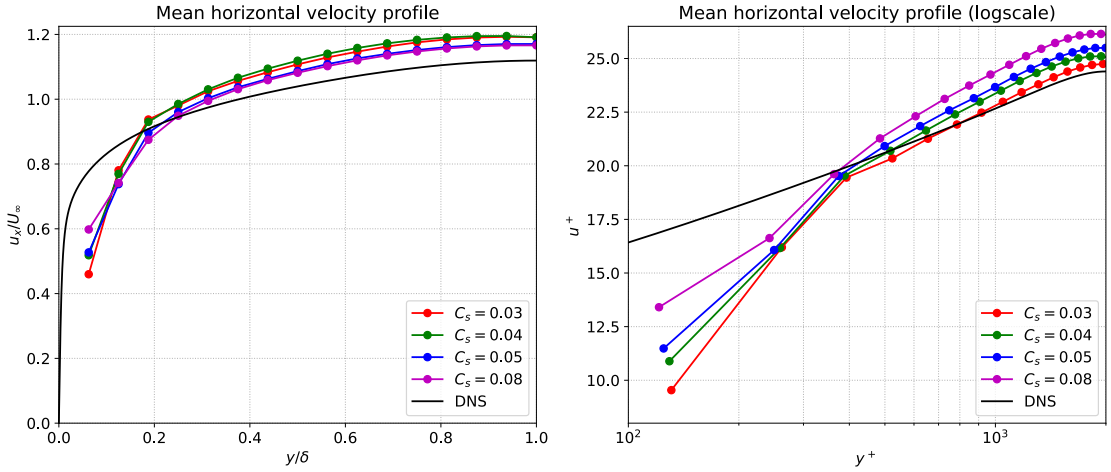

Figure 8.6: Channel flow at $Re_\tau = 2000$. Mean velocity profile (left) and in logscale (right). Comparison for different values of C_s.

Table 8.3 shows the opposite link between u_τ and C_s than the one observed when the slip velocity is extrapolated. Indeed, an increase of the coefficient C_s reduces u_τ. The most suitable value of C_s can also be found, such that it gives the closest u_τ from the reference and, in this case, $C_s = 0.05$. However, as observed in 8.6, the simulation done with $C_s = 0.05$ is not the one that overlaps the most with the reference, but it is slightly shifted.

C_s	0.03	0.04	0.05	0.08
u_τ [m/s]	0.0482	0.04761	0.04591	0.04460

Table 8.3: Friction velocity with respect to SMAG coefficient C_s.

Figure 8.7 shows the statistics for the second case. The RMS fluctuation profiles are much better. Indeed, the behavior is the one expected with a decreasing slope when achieving the bulk region. However, the fluctuation of u is still over-predicted, while those of v and w are under-predicted. Nevertheless, these opposite effects counterbalance a little, and the turbulent kinetic energy overlaps with the reference for $y/\delta > 0.6$, while it is still overestimated near the wall. The choice of C_s has a slight impact on RMS fluctuations, except on the fluctuation of u, and thus, increasing C_s leads to slightly higher values near the wall. For the term $\langle u'v' \rangle$, the linear behavior in the bulk is well retrieved and does not vary a lot depending on the value of C_s. The slopes are still too high but much closer to the one of the reference in comparison to the previous case. Near the wall, the constant C_s has a more significant impact, and increasing the latter leads to increases the value of the closest point to the wall. The observed deficit may be indicative of the effect of ν_{sgs}, since the summation of the three shear stress contributions is supposed to give a straight line from equation 8.15. Hence, imposing a slip-velocity based on the model, and so the theoretical velocity profile, leads to better performance and especially for statistics.

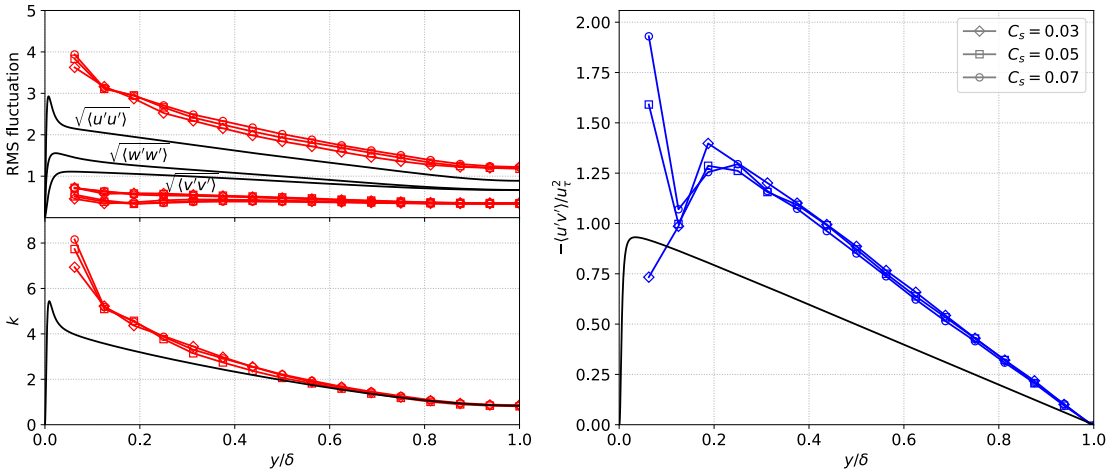

Figure 8.7: Channel flow at $Re_\tau = 2000$. RMS velocity fluctuation profile (left) and Mean shear stress profiles (right). Comparison for different values of C_s, with 0.03 (diamonds), 0.05 (squares) and 0.07 (circles).

8.4 Conclusion and possible ways to improve the model

As experienced, imposing valid conditions at the wall for a wmLES in a velocity-vorticity based code are not trivial. An algebraic model is proposed based on the shear stress equation and a ν_{sgs}. Furthermore, the slip velocity is imposed from the $\partial u/\partial y|_{y=0}$ found and the finite difference expression of the fourth order. Even if the presented model manages to achieve promising performances such as approximating the mean velocity profile of the DNS of Lee and Moser [28] for the simulation of a turbulent channel flow at $Re_\tau = 2000$, the statistics associated with the flow are not close enough to the DNS yet. Indeed, other wmLES strategies, as done by Frère et al. [14] or Thiry [48], but also that of many others before them, have shown better agreement with DNS results. However, the latter do not have the constraint of working with the velocity-vorticity formulation.

Several ways to improve the models could be investigated. Minor changes could be made, such as using a different LOTW. Indeed, as stated by Thiry [48], the Reichardt's LOTW demonstrates better convergence properties. Thiry [48] also studied the impact of correction on ν_{sgs}, which could also be done for this model. The vorticity ω_y is also kept at zero at the wall, but since the slip velocity is locally imposed, this vorticity should locally be non-zero. One could verify its impact by computing it after imposing the slip velocity. Furthermore, the SMAG constant C_s seems to have a non-negligible impact on both profile and statistics. It could be interesting to test different combinations of coefficient C_s between the wall model and the one from the LES on the outer layer. Finally, the choice of strategy to impose the slip velocity seems to have an important impact on the model, especially on statistics. Thus, the method from finite difference exhibits an improvement in results, but one could use other strategies, such as using slip length expression, as done by Bae et al. [2] or Bose and Moin [3], which investigate a slip boundary condition with transpiration through the wall as Robin boundary condition.

Chapter 9

Conclusion

Two main objectives are identified in the present work. The first one is the implementation of a no-slip boundary condition for DNS. The second one is the investigation of a wall-modeled LES in a velocity-vorticity code.

First and foremost, the code's ability in DNS is investigated through the Taylor-Green vortex benchmark at a moderate Reynolds number of $Re = 1600$. Thus, the DNS performed with Murphy yields solid agreement with the reference, which has been done with a pseudo-spectral code. Furthermore, even under-resolved simulation can accurately capture the flow and give satisfactory results. Next, two SGS models are implemented, the classical "complete-complete" Smagorinzky (SMAG) model and the "complete-small" Regularized Variational Multiscale (RVM) model. The Taylor-Green vortex test case is re-used, but this time with SGS models, in order to observe their influence on an under-revolved simulation of isotropic turbulent flow. As a result, no significant improvement in global diagnostics is observed, but the models work as expected from spectra analysis. Indeed, they dissipate the smallest scales, especially with the RVM model. The latter acts on a small-scale filtered field, constraining its range of influence only on the smallest scales.

Then, a no-slip boundary condition is added to the code. The first step is to implement a no-through boundary condition by merely imposing the right odd and even extensions of the velocity and vorticity field components. As a validation, the vortex-rings reconnection at $Re_\Gamma = 2000$ is studied. Indeed, the boundary condition acts like a symmetry plane and is set such as allowing diffusion through the wall. By simulating one ring in the computational domain, the interaction with another ring of opposite circulation and of identical magnitude can be reproduced. These conditions guarantee the reconnection of both rings, and this method has the advantage of requiring twice as less computational resources than if both rings have to be simulated. By visualizing the vorticity field in 3D and 2D, it can be confirmed that the rings have reconnected and the boundary condition has been correctly implemented. Once the no-through flow boundary condition is well implemented, the no-slip can be imposed. The velocity at the wall is set to zero, while a vortex sheet is placed at the wall to impose a consistent condition on the vorticity. This vortex sheet is computed using decentered finite differences of the fourth order from the velocity above the

wall. A first validation is made with the convergence into a Poiseuille laminar flow in a channel by imposing a constant flow rate. Thus, the flow correctly fits the analytical solution while keeping a constant flow rate. Next, the DNS of a turbulent channel flow is performed at a low Reynolds number of $Re_\tau = 180$ and compared to the results of Lee and Moser [28]. The mean velocity profile is well retrieved and matches the reference, as well as the estimated friction velocity. More deviations are observed in the statistics study, such as for RMS fluctuations, but they are still close to the reference results.

The DNS of turbulent channel flow requires important computational resources, even for low Reynolds numbers. Thus, a wall-modeled LES (wmLES) is investigated in order to relax the constraint on grid size. Many have already implemented such models with satisfactory results, in particular in the study of Thiry [48], on which we regularly base ourselves. However, these researchers all use velocity-pressure codes, which have the advantage of having boundary conditions expressed as fluxes, and the viscous flux can straight be defined as the wall shear stress from the wall model. Hence, it is more challenging with codes such as Murphy that required to find consistent conditions on vorticity and velocity. For the outer layer, the code uses the SMAG model to perform LES. For the inner layer, an algebraic wall model is investigated by imposing vorticity at the wall from the expression of shear stress and using the information of the flow in the log layer from a Law Of The Wall (LOTW). A slip velocity is also imposed at the wall. Promising results have been observed for a turbulent channel flow of $Re_\tau = 2000$, but the model still needs to be improved since statistics are overestimated. Several ways are possible, but the most critical one seems to be a parametric study of both C_s coefficients and to correctly impose the slip velocity. One idea might be to use slip length to impose the boundary condition on the velocity.

Appendix A

Slightly under-resolved DNS of Turbulent channel flow at $Re_\tau = 180$

In Chapter 7, the DNS of turbulent channel flow at $Re\tau = 180$ is done in Murphy with a fine grid of $768 \times 256 \times 512$ dof. However, a slightly under-resolved DNS was at first realized in order to study the behavior of this test case for shorter computation times. Hence, initial conditions and numerical setup are exactly as described before, but with a grid twice as coarse, as give in Table A.1.

$Re_\delta = \delta U_\infty / \nu$	$Re_\tau = \delta u_\tau / \nu$	N_x	N_y	N_z	L_x/δ	L_y/δ	L_z/δ	t_c [s]
2800	180	384	128	256	6.0	2.0	4.0	7.78

Table A.1: Numerical parameters for simulation of the turbulent channel flow at $Re_\tau = 180$.

The simulation is made on 256 CPUs and during 96 hours of physical time to achieve the wanted simulation time of $\tau = 25$.

A.1 Results and discussion

Figure A.1 shows the average velocity profile and it is compared with the DNS of Lee and Moser [28]. Thus, the characteristic shape of the turbulent channel flow is well retrieved even though there are very slight variations. Figure A.2 represents this same profile in a logarithmic scale and for the dimensionless variables. Because of the underestimation of the friction velocity of $u_\tau = 0.06162$ instead of $u_\tau = 0.0637$ [28], the profile is shifted upwards. However, the first points fit well with the reference.

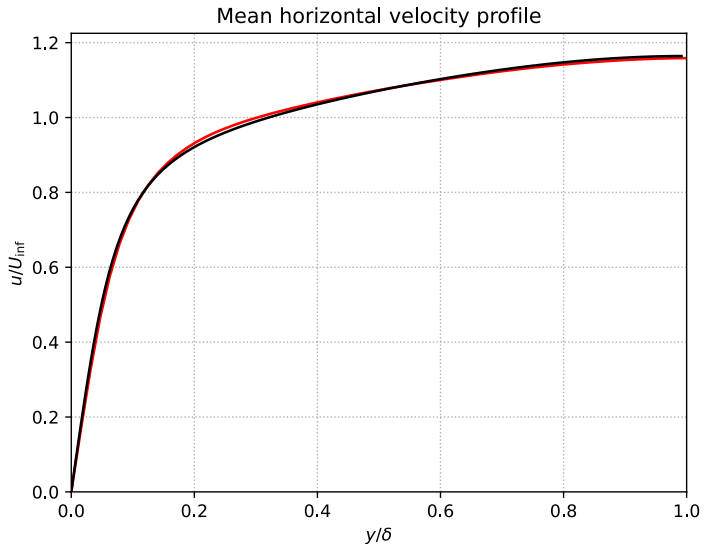

Figure A.1: Channel flow at $Re_\tau = 180$. Mean velocity profile: DNS of Lee and Moser [28] (—) and under-resolved DNS from Murphy (—).

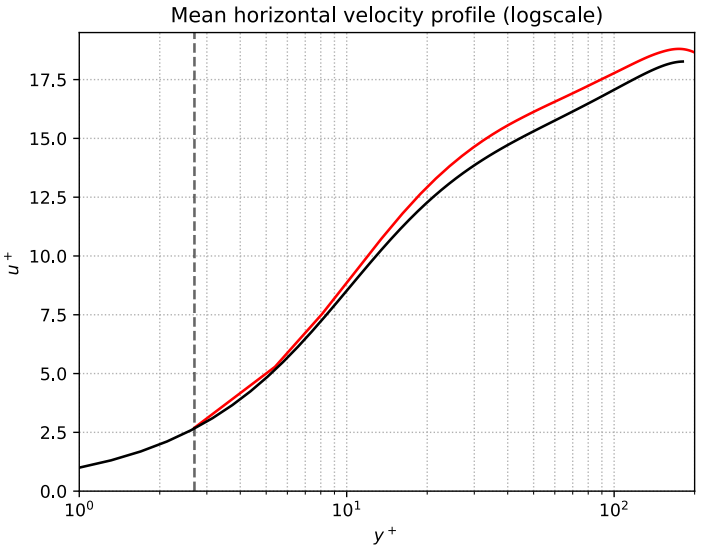

Figure A.2: Channel flow at $Re_\tau = 180$. Mean velocity profile in logscale: DNS of Lee and Moser [28] (—) and under-resolved DNS from Murphy (—). The dashed line corresponds to y_1^+ from our mesh.

The RMS fluctuation are shown in Figure A.3 and the turbulent kinetic energy in Figure A.4. Hence, the three RMS quantities globally retrieve the same behavior as the results of the reference. However, fluctuations in the streamwise direction are slightly overestimated while those in other directions are underestimated. Thus, this difference is compensated and the turbulent kinetic energy is better conserved and fits with the reference, with a slight shift upwards, as seen in A.4.

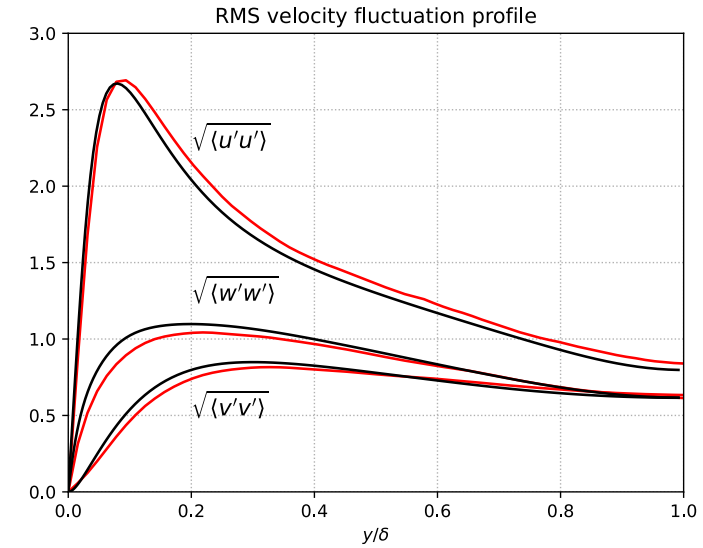

Figure A.3: Channel flow at $Re_\tau = 180$. RMS velocity fluctuation profiles: DNS of Lee and Moser [28] (—) and under-resolved DNS from Murphy (—).

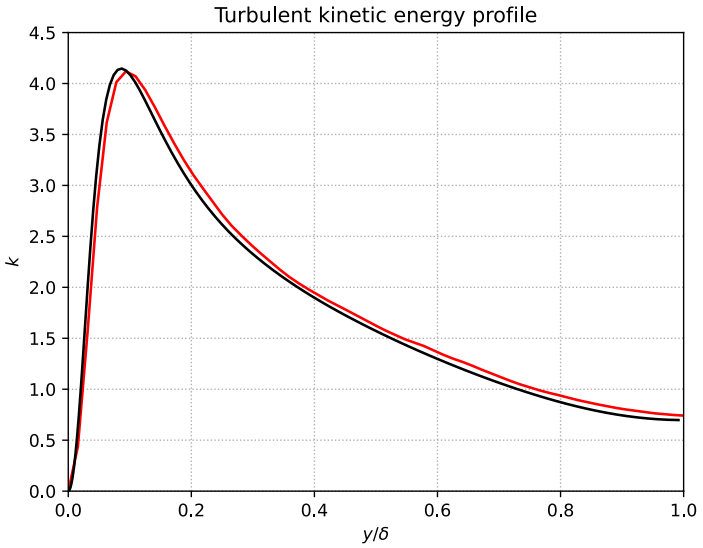

Figure A.4: Channel flow at $Re_\tau = 180$. Turbulent kinetic energy profile: DNS of Lee and Moser [28] (—) and under-resolved DNS from Murphy (—).

Figure A.5 shows that both molecular and turbulent shear stress converge toward the reference but the curves are closer to the reference in the bulk. Indeed, we observe that for $y/\delta < 0.2$, both curves are slightly shifted toward right, which also induce a small deficit in the total shear stress line. However, the linear behavior is globally preserved.

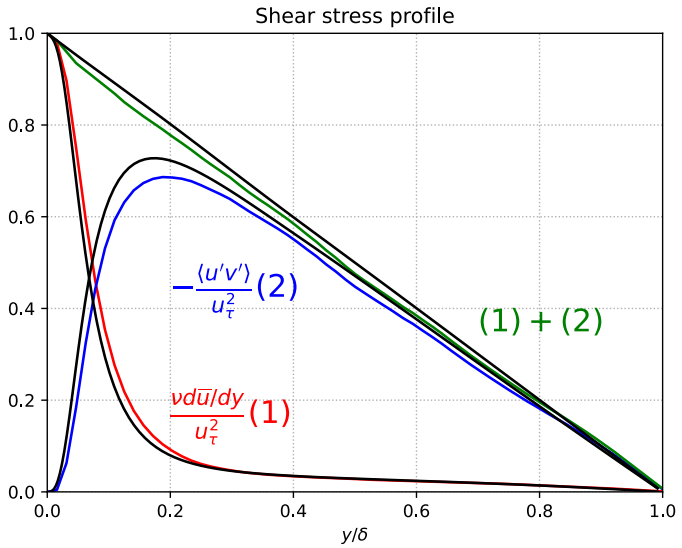

Figure A.5: Channel flow at $Re_\tau = 180$. Mean shear stress profiles: DNS of Lee and Moser [28] (—) and DNS from Murphy (—), (—), (—).

A.2 Conclusion

In conclusion, the slightly under-resolved DNS gives good agreement with the DNS of Lee and Moser [28]. The major difference with the DNS done in Murphy is the computed friction velocity. Indeed, they are respectively $u_\tau = 0.06162$ [m/s] and $u_\tau = 0.06428$ [m/s], in comparison with $u_\tau = 0.0637$[m/s] from Lee and Moser [28]. The DNS presented in chapter 7 still provides a better profiles, such as average velocity, RMS fluctuations and shear stress profiles, but we are still able to achieve close results with a grid twice as coarse.

Bibliography

[1] G. Aubard et al. “Comparison of Subgrid-scale Viscosity Models and Selective Filtering Strategy for Large-eddy Simulations”. In: *Flow, Turbulence and Combustion* 91.3 (July 2013), pp. 497–518. DOI: 10.1007/s10494-013-9485-5.

[2] H. Jane Bae et al. “Dynamic slip wall model for large-eddy simulation”. In: (2018). DOI: 10.48550/ARXIV.1810.04214.

[3] S. T. Bose and P. Moin. “A dynamic slip boundary condition for wall-modeled large-eddy simulation”. In: *Physics of Fluids* 26.1 (Jan. 2014), p. 015104. DOI: 10.1063/1.4849535.

[4] Marc E. Brachet et al. “Small-scale structure of the Taylor–Green vortex”. In: *Journal of Fluid Mechanics* 130.-1 (May 1983), p. 411. DOI: 10.1017/s0022112083001159.

[5] Denis-Gabriel Caprace, Thomas Gillis, and Philippe Chatelain. “FLUPS: A Fourier-Based Library of Unbounded Poisson Solvers”. In: *SIAM Journal on Scientific Computing* 43.1 (Jan. 2021), pp. C31–C60. DOI: 10.1137/19m1303848.

[6] Corentin Carton de Wiart. “Towards a Discontinuous Galerkin solver for scale-resolving simulations of moderate Reynolds number flows, and application to industrial cases”. PhD thesis. 2014.

[7] Haecheon Choi and Parviz Moin. “Grid-point requirements for large eddy simulation: Chapman’s estimates revisited”. In: *Physics of Fluids* 24.1 (Jan. 2012), p. 011702. DOI: 10.1063/1.3676783.

[8] R. Cocle, L. Bricteux, and G. Winckelmans. “Scale dependence and asymptotic very high Reynolds number spectral behavior of multiscale subgrid models”. In: *Physics of Fluids* 21.8 (Aug. 2009), p. 085101. DOI: 10.1063/1.3194302.

[9] R. Cocle, L. Dufresne, and G. Winckelmans. “Investigation of Multiscale Subgrid Models for LES of Instabilities and Turbulence in Wake Vortex Systems”. In: *Ecole polytechnique de Louvain, Université catholique de Louvain*. 2007.

[10] James W. Deardorff. “A numerical study of three-dimensional turbulent channel flow at large Reynolds numbers”. In: *Journal of Fluid Mechanics* 41.2 (Apr. 1970), pp. 453–480. DOI: 10.1017/s0022112070000691.

[11] James DeBonis. "Solutions of the Taylor-Green Vortex Problem Using High-Resolution Explicit Finite Difference Methods". In: *51st AIAA Aerospace Sciences Meeting including the New Horizons Forum and Aerospace Exposition*. American Institute of Aeronautics and Astronautics, Jan. 2013. DOI: 10.2514/6.2013-382.

[12] Dimitris Drikakis et al. "Simulation of transition and turbulence decay in the Taylor–Green vortex". In: *Journal of Turbulence* 8 (Jan. 2007), N20. DOI: 10.1080/14685240701250289.

[13] Daniel Foti and Karthik Duraisamy. "Multi-dimensional finite volume scheme for the vorticity transport equations". In: *Computers &amp Fluids* 167 (May 2018), pp. 17–32. DOI: 10.1016/j.compfluid.2018.02.024.

[14] Ariane Frère et al. "Application of wall-models to discontinuous Galerkin LES". In: *Physics of Fluids* 29.8 (Aug. 2017), p. 085111. DOI: 10.1063/1.4998977.

[15] James Gabbard. *High-order energy- and helicity-preserving finitedifference schemes for 3D vortex dynamics*. MIT Van Rees Lab. 2021.

[16] Laurent GEORGES. "Development and validation of a LESmethodology for complex wall-boundedflows". PhD thesis. Faculté des sciences appliquées Université catholique de Louvain, 2007.

[17] T. Gillis et al. "A 2D immersed interface Vortex Particle-Mesh method". In: *Journal of Computational Physics* 394 (Oct. 2019), pp. 700–718. DOI: 10.1016/j.jcp.2019.05.033.

[18] Thomas Gillis and Wim M. van Rees. *MURPHY – A scalable multiresolution framework for scientific computing on 3D block-structured collocated grids*. 2021. DOI: 10.48550/ARXIV.2112.07537.

[19] Sheldon I. Green, ed. *Fluid mechanics and its applications - Fluid Vortices*. 2nd. Springer-Science+Business Media, B.V., 1995.

[20] Charles Hirsch. *Numerical Computation of Internal and External Flows. Volume1-Fundamentals of Computational Fluid Dynamics*. Ed. by Elsevier. 2nd. Vol. 1. 2nd edn. Butterworth-Heinemann, 2007.

[21] Thomas J. R. Hughes et al. "The multiscale formulation of large eddy simulation: Decay of homogeneous isotropic turbulence". In: *Physics of Fluids* 13.2 (Feb. 2001), pp. 505–512. DOI: 10.1063/1.1332391.

[22] Mohamed Iskandarani. *Syllabus, Numerical Methods and in Fluid and Dynamics*. Rosenstiel School of Marine and Atmospheric Science. 2015.

[23] Gaëtan Jacquemin. "Interaction d'anneaux vortex de circulations différentes". MA thesis. Ecole polytechnique de Louvain, Université catholique de Louvain, 2016-2017.

[24] H. Jeanmart and G. Winckelmans. "Investigation of eddy-viscosity models modified using discrete filters: A simplified "regularized variational multiscale model" and an "enhanced field model"". In: *Physics of Fluids* 19.5 (May 2007), p. 055110. DOI: 10.1063/1.2728935.

[25] Milovan Perić Joel H. Ferziger. *Computational Methods for Fluid Dynamics*. Ed. by Springer. 3rd. 3rd Ed. 2002.

[26] Volker John and Michael Roland. "Simulations of the turbulent channel flow atRe = 180 with projection-based finite element variational multiscale methods". In: *International Journal for Numerical Methods in Fluids* 55.5 (2007), pp. 407–429. DOI: 10.1002/fld.1461.

[27] Soshi Kawai and Johan Larsson. "Wall-modeling in large eddy simulation: Length scales, grid resolution, and accuracy". In: *Physics of Fluids* 24.1 (Jan. 2012), p. 015105. DOI: 10.1063/1.3678331.

[28] Myoungkyu Lee and Robert D. Moser. "Direct numerical simulation of turbulent channel flow up to". In: *Journal of Fluid Mechanics* 774 (June 2015), pp. 395–415. DOI: 10.1017/jfm.2015.268.

[29] Clement Lepot. "Implementation and validation of symmetry and no-slip boundary conditions in a 3-D vortex particle-mesh method". MA thesis. Ecole polytechnique de Louvain, Université catholique de Louvain, 2016-2017.

[30] Marcel Lesieur and Sepand Ossia. "3D isotropic turbulence at very high Reynolds numbers: EDQNM study". In: *Journal of Turbulence* 1 (Jan. 2000), N7. DOI: 10.1088/1468-5248/1/1/007.

[31] M. de la Llave Plata and R.S. Cant. "A wavelet-based multiresolution approach to large-eddy simulation of turbulence". In: *Journal of Computational Physics* 229.20 (Oct. 2010), pp. 7715–7738. DOI: 10.1016/j.jcp.2010.06.027.

[32] Guido Lodato, Patrice Castonguay, and Antony Jameson. "Structural Wall-modeled LES Using a High-order Spectral Difference Scheme for Unstructured Meshes". In: *Flow, Turbulence and Combustion* 92.1-2 (Nov. 2013), pp. 579–606. DOI: 10.1007/s10494-013-9523-3.

[33] John R. Mansfield, Omar M. Knio, and Charles Meneveau. "A Dynamic LES Scheme for the Vorticity Transport Equation: Formulation anda PrioriTests". In: *Journal of Computational Physics* 145.2 (Sept. 1998), pp. 693–730. DOI: 10.1006/jcph.1998.6051.

[34] John R. Mansfield, Omar M. Knio, and Charles Meneveau. "Dynamic LES of Colliding Vortex Rings Using a 3D Vortex Method". In: *Journal of Computational Physics* 152.1 (June 1999), pp. 305–345. DOI: 10.1006/jcph.1999.6258.

[35] Mogens V. Melander and Fazle Hussain. "Cut-and-connect of two antiparallel vortex tubes". In: (1988).

[36] O. Métais. "Large-Eddy Simulations of Turbulence". In: *Les Houches - Ecole d'Ete de Physique Theorique*. Springer Berlin Heidelberg, pp. 113–186. DOI: 10.1007/3-540-45674-0_3.

[37] Johan Meyers, Pierre Sagaut, and Bernard J. Geurts. "Optimal model parameters for multi-objective large-eddy simulations". In: *Physics of Fluids* 18.9 (Sept. 2006), p. 095103. DOI: 10.1063/1.2353402.

[38] Kolmogorov A. N. "Equations of turbulent motion of an incompressible fluid". In: *Izvestia Academy of Sciences* (1942).

[39] George Ilhwan Park and Parviz Moin. "Space-time characteristics of wall-pressure and wall shear-stress fluctuations in wall-modeled large eddy simulation". In: *Physical Review Fluids* 1.2 (June 2016), p. 024404. DOI: 10.1103/physrevfluids.1.024404.

[40] Wim M. van Rees et al. "A comparison of vortex and pseudo-spectral methods for the simulation of periodic vortical flows at high Reynolds numbers". In: *Journal of Computational Physics* 230.8 (Apr. 2011), pp. 2794–2805. DOI: 10.1016/j.jcp.2010.11.031.

[41] Austin Richards, Tony Saad, and James C. Sutherland. "A Fast Turbulence Generator using Graphics Processing Units". In: *2018 Fluid Dynamics Conference*. American Institute of Aeronautics and Astronautics, June 2018. DOI: 10.2514/6.2018-3559.

[42] Tony Saad and James C. Sutherland. "Diffusion by a random velocity field". In: *Physics of Fluids* 28.11 (Nov. 2016), p. 119101. DOI: 10.1063/1.4968528.

[43] Tony Saad and James C. Sutherland. *University of Utah's synthetic turbulence generator and tools*. University of Utah Turbulence Generator and Tools. URL: https://turbulence.utah.edu/.

[44] Tony Saad et al. "Scalable Tools for Generating Synthetic Isotropic Turbulence with Arbitrary Spectra". In: *AIAA Journal* 55.1 (Jan. 2017), pp. 327–331. DOI: 10.2514/1.j055230.

[45] U. Schumann. "Subgrid scale model for finite difference simulations of turbulent flows in plane channels and annuli". In: *Journal of Computational Physics* 18.4 (Aug. 1975), pp. 376–404. DOI: 10.1016/0021-9991(75)90093-5.

[46] S. Stolz, P. Schlatter, and L. Kleiser. "High-pass filtered eddy-viscosity models for large-eddy simulations of transitional and turbulent flow". In: *Physics of Fluids* 17.6 (June 2005), p. 065103. DOI: 10.1063/1.1923048.

[47] Wim Sweldens. "The Lifting Scheme: A Construction of Second Generation Wavelets". In: *SIAM Journal on Mathematical Analysis* 29.2 (Mar. 1998), pp. 511–546. DOI: 10.1137/s0036141095289051.

[48] Olivier Thiry. "Investigation of wall shear stress models for large eddy simulation". PhD thesis. Ecole polytechnique de Louvain, Université catholique de Louvain, 2018.

[49] UMD. *Website of UMD on WMLES and Wall-stress models*. en-US. URL: https://wmles.umd.edu/wall-stress-models/ (visited on 05/26/2023).

[50] G. Winckelmans. *Lecture notes in LMECA2660 Numerical methods in fluid mechanics*. Universtié Catholique de Louvain. 2018.

[51] G. Winckelmans. *Lecture notes in LMECA2853 Turbulence*. Universtié Catholique de Louvain. 2011.

[52] Jie-Zhi Wu, Hui-Yang Ma, and Ming-De Zhou. *Vorticity and Vortex Dynamics*. Springer Berlin Heidelberg, 2006. DOI: 10.1007/978-3-540-29028-5.

UNIVERSITÉ CATHOLIQUE DE LOUVAIN
École polytechnique de Louvain
Rue Archimède, 1 bte L6.11.01, 1348 Louvain-la-Neuve, Belgique | **www.uclouvain.be/epl**